THEORETICAL SCHEMES FOR NEGATIVE REFRACTION AND ENHANCED REFRACTIVE INDEX IN ATOMIC SYSTEMS

by

Daniel E. Sikes

A dissertation submitted in partial fulfillment of
the requirements for the degree of

Doctor of Philosophy

(Physics)

at the

UNIVERSITY OF WISCONSIN–MADISON

2012

Date of final oral examination: October 1, 2012

The dissertation is approved by the following members of the Final Oral Committee:

Deniz D. Yavuz, Associate Professor, Physics
James E. Lawler, Professor, Physics
Mark Saffman, Professor, Physics
Thad G. Walker, Professor, Physics
John C. Wright, Professor, Chemistry

ACKNOWLEDGMENTS

I would like to thank my advisor Deniz Yavuz for his help over the years and always having the time to answer my questions. I would also like to thank my undergraduate professors Steve Reynolds, Charlie Johnson, Sandy Paur, and Laura Clarke for inspiring me to challenge myself. I also would like to acknowledge my fellow grad students Nick Proite, Tyler Green, Josh Weber, Zach Simmons, and Jared Miles for their help and suggestions over the years. Additionally the support and encouragement of my parents has been very important to me to throughout my graduate studies. Finally I wish to acknowledge the support of my wonderful girl friend Stacy.

DISCARD THIS PAGE

TABLE OF CONTENTS

Page

DISCARD THIS PAGE

LIST OF FIGURES

Appendix
Figure Page

DISCARD THIS PAGE

NOMENCLATURE

$\mathcal{E}_i$	Electric field Fourier amplitude at frequency ω_i
$\mathcal{B}_i$	Magnetic field Fourier amplitude at frequency ω_i
P_i	Polarization Fourier amplitude at frequency ω_i
M_i	Magnetization Fourier amplitude at frequency ω_i
δ	One-photon detuning
ϵ_0	Permittivity of free-space
μ_0	Permeability of free-space
ϵ	Relative permittivity
μ	Relative permeability
$\hat{d}$	Electric dipole transition operator
$\hat{\mu}$	Magnetic dipole transition operator
c_i	Probability amplitude of quantum state $\|i\rangle$
$\rho_{ij} \equiv c_i c_j^*$	Coherence of quantum states $\|i\rangle$ and $\|j\rangle$
Γ_i	Decay rate of excited electronic state $\|i\rangle$
γ_j	Decay rate of excited Raman or magnetic state $\|j\rangle$

ABSTRACT

In this thesis we present a scheme that achieves negative refraction with low absorption in far-off resonant atomic systems. Negative refraction was predicted over 4 decades ago and recently experimentally demonstrated. Over the last decade there has been much active research in negative refractive index in the field of metamaterials. We seek a new approach for negative refraction using laser driven transition resonances in atomic systems. By utilizing atomic system resonances we hope to achieve negative refraction in short wavelength regimes inaccessible to metamaterials, such as visible and ultra-violet, and eliminate absorption by quantum interference techniques.

This scheme is based on the recently predicted and experimentally demonstrated "refractive index enhancement with vanishing absorption" technique, in which closely spaced absorptive and amplifying transitions are interfered. Our scheme utilizes Raman transitions and is able to strongly drive an atomic electric resonance while far-detuned from an electric dipole transition. This far-off resonance feature allows our scheme to be adaptable to various atomic energy level structures, in that it does not require the simultaneous presence of an electric dipole transition and a magnetic dipole transition near the same wavelength. To our knowledge, this constraint for simultaneous transitions is featured in all previous suggestions for negative refraction and the lack of a suitable existing level structure prevents experimental implementation. We show that two interfering Raman transitions coupled to a magnetic dipole transition can achieve a negative index of refraction with low absorption through magnetoelectric cross coupling. Analytical predictions have been made for a model atomic system and the validity of the analytical results have been confirmed with exact numerical simulations of the density matrix. We also discuss possible experimental implementations of the scheme in rare-earth metal atomic systems, such as ultracold vapors and doped crystals.

In this thesis we also discuss how negative and enhanced refractive index can be utilized in imaging systems and other applications. A fundamental challenge of modern imaging systems is the diffraction limit. The diffraction limit causes spatial features of an object that are smaller than the light wavelength to be lost in the image. Achieving negative refraction with vanishing absorption is potentially important for near-perfect imaging systems based on Pendry's suggestion for a negative index material perfect lens. This perfect lens idea is able to focus the light related to small spatial features through the unique ability of negative index materials to "amplify" evanescent waves. Alternatively, techniques for enhanced refractive index improve imaging resolution by effectively decreasing the light wavelength by a factor inversely proportional the refractive index. Additionally we consider in this thesis proposals for all-optical devices based on refractive index enhancement such as a low-photon conditional phase shifter and a distributed Bragg reflector.

Chapter 1

An overview of light matter interactions

1.1 Introduction and background

The index of refraction, n, of a material is a parameter that well describes the unique interaction between the material and an electromagnetic wave. It is in general, a complex quantity that describes how a light wave propagating through matter differs from that of a vacuum. The simplest interpretation is that the real part describes the slowing of light in more "optically dense" matter and the imaginary part relates to absorption of the wave's energy by the material system.

Knowledge of the interaction of light with matter allows us to predict the propagation of light and engineer material systems to harness the properties of light for applications such as imaging, information processing, and photonics. More so, knowledge of the refractive indices of two different materials provides a way of predicting the scattering of light at the interface of the materials. Since in general, the materials will have different optical densities, light has a different speed in each material and Fermat's principle of least time implies that there will be a refraction of the light. Refraction is the perceived bending of light, where the transmitted light ray's trajectory changes to a different angle with respect to the normal of the material interface than the incident ray's angle. This is quantitatively described by Snell's Law in the familiar formula $n_1 \sin\theta_1 = n_2 \sin\theta_2$. The refractive index is also a key parameter in Fresnel's equations which quantitatively describe the splitting of incident light on the interface into reflected and transmitted parts.

The ability of refraction to manipulate the propagation direction of light rays by placing transparent materials in the light's path gives rise to the field of traditional optics and imaging. Lenses are a special class of such materials, which are optical devices that are typically used to focus light.

The shape of a lens, its refractive index, and the refractive index of the medium surrounding the lens determines how well the lens focuses scattered light from an object into a resolved image. One of the most important problems of modern imaging systems is how to effectively image features that are smaller than the wavelength of the light being focused. It is well known in modern optical imaging systems that the spatial resolution is limited by the wavelength of the light scattered from the object. The smallest spatial features that can be resolved have dimensions on the order of λ [53]. This obstacle is the diffraction limit and overcoming this barrier to sub-wavelength imaging has been the subject of much theoretical and experimental research [54, 64, 10, 55, 12, 25, 59, 7].

Inside a refractive medium the effective wavelength is $\lambda = \lambda_0/n$, where λ_0 is the free-space wavelength. Therefore the diffraction limit may be expressed as λ_0/n, where n is the refractive index of the medium. Thus one possible approach to the imaging problem would be to prepare a medium with an increased refractive index. For example, this is why oil immersion microscopes have superior resolution because $n_{oil} > n_{air}$. In part of this thesis we will consider an approach for possibly greatly increasing the refractive index of an atomic vapor while maintaining vanishing absorption. Alternatively, it has recently been suggested that a new imaging approach using negative refractive index materials may be used to beat the diffraction limit [104]. Negative refraction of light has recently been demonstrated in the emerging field of metamaterials [131], but absorptive losses limit their potential uses for imaging. In part of this thesis we will suggest a new approach for using laser driven atomic systems to achieve negative refraction with vanishing absorption that may be suitable for negative index lenses. We will also explore some applications of this enhanced refractive index beyond improvement to imaging resolution such as optical switching.

1.2 Origin of refractive index

The refractive index as discussed so far is a macroscopic property of a material that describes its interaction with light. However, the origin of the refractive index comes from taking into account the cumulative interaction of the light's electric and magnetic fields with the material's microscopic building blocks (e.g. atoms, molecules, or as we will discuss later, meta-atoms). When a light wave propagates through a material system, as opposed to free-space, there is an interaction that occurs

at the atomic or molecular level which uniquely modifies the wave propagation. The electric and magnetic fields of the light cause a deformation of the microscopic electric charge distribution of the system's atoms or molecules. This deformation of the charge distribution causes the constituent particles of the system to behave as microscopic dipoles, which tend to align themselves with the propagating electric and magnetic fields. These dipoles are driven to oscillate at the frequency of the incident light, which then radiate their own light wavefronts at this frequency. Thus the resulting macroscopic light wave observed in the material is a linear superposition of the primary incident light and the secondary dipole radiated light, that oscillates at the incident frequency.

Quantitatively, the interaction of the light's electromagnetic fields with the material that induces and aligns dipoles is described by the polarizing effect in the medium. The dipole moments of the materials constituent particles are given by

$$\begin{aligned} p &= \alpha_{\mathcal{E}}\mathcal{E} \quad , \\ m &= \alpha_{\mathcal{B}}\mathcal{B} \quad , \end{aligned} \tag{1.1}$$

where $\alpha_{\mathcal{E}}$ and $\alpha_{\mathcal{B}}$ are the electric and magnetic polarizability coefficients, respectively, and the $\mathcal{E}$ and $\mathcal{B}$ are the electric and magnetic fields of the incident light. The collective behavior of the particles is macroscopically described by the (electric) polarization, P, and magnetization, M, which are the electric and magnetic dipole moments per unit volume of the bulk material. If we consider a uniform number density of particles N, then the total polarization and magnetization are given by

$$\begin{aligned} P &= Np = N\alpha_{\mathcal{E}}\mathcal{E} \quad , \\ M &= Nm = N\alpha_{\mathcal{B}}\mathcal{B} \quad . \end{aligned} \tag{1.2}$$

More commonly, the polarization and magnetization are expressed in terms of the electric and magnetic susceptibilities, $\chi_{\mathcal{E}}$ and $\chi_{\mathcal{B}}$, respectively, as

$$\begin{aligned} P &= \epsilon_0\chi_{\mathcal{E}}\mathcal{E} \quad , \\ M &= \frac{1}{\mu_0}\chi_{\mathcal{B}}\mathcal{B} \quad . \end{aligned} \tag{1.3}$$

The susceptibilities are dimensionless proportionality factors that relate the induced polarizations in the medium to the applied field strengths. In terms of the polarizabilities, the susceptibilities are given by

$$\chi_{\mathcal{E}} = \frac{N}{\epsilon_0}\alpha_{\mathcal{E}} \quad ,$$
$$\chi_{\mathcal{B}} = N\mu_0\alpha_{\mathcal{B}} \quad . \qquad [1.4]$$

We now consider the time dependent nature of the polarizing effect occurring in the system. The polarized dipole moments vary in time since the electromagnetic fields that induce the polarization are not static but oscillate at the frequency of the incident light wave. The behavior of the dipoles may be viewed as damped harmonic oscillators that are driven by the sinusoidal electromagnetic fields of the light. From a linear treatment of the driven harmonic motion, the dipole moments will oscillate at the driving frequency, however the amplitude of the oscillation will depend on the structure of the particles. The particles' structure determines the natural resonant frequencies and damping coefficients of the dipoles' harmonic motion. Therefore the magnitude of the oscillating polarization in the material will be frequency dependent as determined by the detuning of the incident light's frequency from the particles' resonance frequencies.

The macroscopic polarization and magnetization responses in a material are characterized by the constitutive parameters of the relative electric permittivity, ϵ, and relative magnetic permeability, μ, respectively (Note: be aware of confusion distinguishing the relative and absolute parameters, because many other notation styles feature a subscript 'r' for these dimensionless relative coefficients). These parameters are in general complex, frequency dependent quantities that describe the dispersion and absorption of light propagating through matter. The relative permittivity and permeability are conveniently expressed in terms of the electric and magnetic susceptibilities as

$$\epsilon = 1 + \chi_{\mathcal{E}} \quad ,$$
$$\mu = 1 + \chi_{\mathcal{B}} \quad . \qquad [1.5]$$

The susceptibilities are dimensionless numbers that describe relative change of the permittivity and permeability from their free-space values, ϵ_0 and μ_0. In a sense the susceptibility is a parameter

that relates to the tendency of the system's matter to become polarized in response to applied electromagnetic fields.

The physical significance of the permittivity and permeability is most readily seen in the observed slowing of light when propagating through matter. One of the features derived from the inclusion of ϵ and μ in Maxwell's wave equations is that the square of the wave phase velocity is given by $v^2 = \frac{c^2}{\epsilon\mu}$. This product of the permittivity and permeability, appearing in many electromagnetic expressions, is a consequence of the coupling of the electric and magnetic fields in Maxwell's equations. Thus the refractive index is traditionally defined as the parameter n, which quantifies the reduced speed of light in matter and is given by

$$n^2 = \epsilon\mu \quad . \tag{1.6}$$

This observed change of speed results from phase differences between the primary incident light and secondary dipole radiated light by the material's polarized particles. These phase differences cause the superposition of light observed in the material to have a different wavelength than the incident light, although it oscillates at the incident light frequency. This change of the wavelength in matter can by derived from the wave phase velocity relations. The speed of light in a free-space is $c = f\lambda_0$ and in matter it is $v = \frac{c}{n} = f\frac{\lambda_0}{n}$. This reduction of $\lambda \rightarrow \lambda_0/n$ in a refractive medium (with $n > 1$) may be used to reduce diffractive effects, which cause a break down for rectilinear propagation of the light when the spatial dimensions concerned are on the order of the wavelength.

The ability to find or create materials with large values for ϵ and μ is of much interest because a larger refractive index improves resolution in imaging applications. This is very fundamental in the integrated circuit industry, where the resolution of lithographic techniques creates a limitation on how small and dense computer processing elements can be designed. A greatly enhanced refractive index would also be of interest in biological imaging applications, where nondestructive optical microscopy could potentially be used to image live samples at high resolution.

1.3 Origin of diffraction limit

We now consider a brief derivation of the diffraction limit. We will denote the free space wave vector as $k_0^2 = k_\perp^2 + k_z^2 = \left(\frac{2\pi}{\lambda_0}\right)^2$, where k_z is the component in the propagation direction and $k_\perp$ is the component in the transverse x-y plane. The field emanating from an object in the transverse plane can be expressed as a superposition of plane wave modes as

$$\mathcal{E}(\rho, z) = \sum_{k_\perp} A(k_\perp) \exp i(k_\perp \rho + k_z z) \quad , \tag{1.7}$$

where $A(k_\perp)$ is the amplitude of the transverse mode, $\rho = \sqrt{x^2 + y^2}$ is the transverse spatial coordinate and we have omitted the time dependent terms. Using the definition of the wave vector, we can substitute $k_z = +\sqrt{k_0^2 - k_\perp^2}$. Here we can see that for modes that satisfy $k_0^2 > k_\perp^2$, the component k_z will be real valued and the wave mode will propagate in the z direction as

$$A(k_\perp) \exp i(k_\perp \rho + \sqrt{k_0^2 - k_\perp^2} z) \quad , \tag{1.8}$$

and can be focused by a conventional lens. On the other hand for modes that have $k_0^2 < k_\perp^2$, the component k_z will be imaginary and the wave mode will be evanescent with exponentially decaying amplitude as the wave front advances in the z direction as

$$\exp -(\sqrt{k_0^2 - k_\perp^2} z) A(k_\perp) \exp i(k_\perp \rho) \quad . \tag{1.9}$$

These decaying amplitudes will be negligibly small at the image plane and thus these large $k_\perp$ Fourier components can not be focused by a conventional lens.

The inability of a lens to focus these evanescent components where $k_\perp > k_0$ is the reason that image resolution is limited. Similar to the Fourier relationship of time and frequency, the Fourier transform that relates space and reciprocal k-space results in an inverse relationship between the resolution of the wave vector components and the spatial dimensions. Small transverse spatial details of an object are associated with a spread of wave modes possessing large $k_\perp$ values that exceed k_0 and can not be properly focused. The Fourier uncertainty principle $k_\perp^{max} \Delta\rho \sim 2\pi$, relates the maximum transverse wave number to the smallest transverse spatial detail $\Delta\rho$. In the

limiting case for the mode to be propagating, $+k_z \rightarrow 0$, we have $k_{\perp}^{max} = k_0 = \frac{2\pi}{\lambda_0}$. Thus we can derive the diffraction limit,

$$\Delta\rho \sim \lambda_0 \quad , \tag{1.10}$$

on the spatial resolution allowed for a given wavelength. This implies that light corresponding to subwavelength features will have attenuated propagation and will be eliminated from the final image. A corollary of this is that the tightest focus that can be achieved for a laser beam is a spot size with a diameter on the order of the laser's wavelength [133]. Hence the diffraction limit presents an obstacle to the limit of how much data can be recorded on optical media, how small computer processors can be designed with lithography, or how to address individual trapped atoms in quantum computing applications.

1.4 Outline of thesis chapters

Chapter 2 introduces the idea of refractive index enhancement with vanishing absorption in an atomic vapor. We describe how the refractive index experienced by an incident laser beam is related to the role of the light in quantum transitions of an atomic system. These quantum transitions result in a modified refractive index for the laser light, but are also accompanied by absorption or amplification of the light. Based on ideas proposed by Scully [124], we consider a system with closely spaced absorption and amplification Raman transitions, that are interfered to produce an enhanced refractive index with canceled absorption of the light. This suggested interference technique is the basis for all of the proposed applications of enhanced refractive index considered in this thesis. We also review the details of recent experimental demonstrations of this technique.

Chapter 3 introduces the concept of negative refractive index that was proposed by Veselago and has recently been experimentally demonstrated. Traditionally negative refractive occurs when both the permittivity and permeability are simultaneously negative valued. Materials that possess this property are not known to exist in nature, however the emerging field of metamaterials have

artificially constructed media that do exhibit negative refractive index. We briefly review the history and operating principles of metamaterials. We also discuss how negative index materials may also provide an alternative approach to the problem of the diffraction limit by considering Pendry's proposed perfect lens. Pendry's lens suggests that a lens made from a negative index material can successfully focus evanescent wave components that are traditionally cut-off by the diffraction limit, by reversing the decay of evanescent modes.

Chapter 4 suggests a new approach to achieve negative refractive index in atomic vapors by interfering Raman transitions and using magnetoelectric cross coupling. We suggest using laser driven atomic systems in hopes to achieve negative refractive index at smaller wavelength regimes than metamaterials and eliminate absorption by quantum interference. In principle negative refraction can be achieved by driving electric and magnetic transition resonances sufficiently strongly and simultaneously at the same light frequency, however this can not be implemented practically. Our suggestion includes a magnetoelectric cross coupling of the resonances, which revises the conditions for negative refraction and reduces the required atomic densities by two orders of magnitude. The key advantage of our approach is that it does not require the simultaneous presence of an electric dipole and a magnetic dipole transition at the same frequency. This gives considerable flexibility in the energy level structure and allows our technique to be implemented with a number of different atomic species. In this chapter we present analytical results for negative refraction in an atomic medium and verify their validity with exact numerical simulations of density-matrix of the system.

Chapter 5 considers possible experimental systems to implement the negative refractive index scheme discussed in Chap. 4. We consider both schemes that use rare-earth atom vapors and rare-earth doped crystals. Ideally we wish to find a system with an existing level structure that has strong electric and magnetic transitions with a small difference in their resonant wavelengths, because the required laser intensities greatly increase as the wavelength difference increases. We consider the rich level structure of the rare-earth atoms to find a suitable level structure by using the ab initio atomic structure code by Cowan [22] to estimate the transition wavelengths and strengths.

We have identified promising experimental systems in ultracold neutral atom vapors of Erbium and Dysprosium and cryogenically cooled crystals doped with ions of Terbium and Praseodymium.

Chapter 6 presents a suggestion for a low photon conditional phase shifter as an application of refractive index enhancement discussed in Chap.2. In this scheme a weak “switching” beam is introduced to the system to modify the nature of the refractive index enhancement. The condition of whether the switching beam is turned on or off results in a shift of the phase accumulated by a probe beam propagating through the medium, while maintaining vanishing absorption. We include a fidelity analysis of the feasibility of using a phase shifted probe beam pulse for optical information applications. This analysis considers the number of spontaneously generated “noise photons” in the mode of the probe beam, which possess random phase and lower the fidelity.

Chapter 7 presents a suggestion to achieve giant Kerr nonlinearities between two weak laser beams by utilizing refractive index enhancement with vanishing absorption. These Kerr nonlinearities differ from other approaches for significant nonlinear interactions at the single photon level in that a strong driving laser is not required by the scheme. We also propose an application for our scheme in which an atomic vapor can function as a distributed Bragg reflector that works at very low light levels.

Chapter 2

An overview of refractive index enhancement

2.1 Introduction

It is well known that according to the linear response of an atom to an electromagnetic field, the refractive index is greatly enhanced near resonance but it is also accompanied by strong absorption. This presents a conflict to the advantages of imaging with enhanced refractive index since the light will be absorbed by the medium within a distance of a fraction of the wavelength. Far from resonance the medium becomes transparent but the refractive index is almost the same as in a vacuum. It was first suggested by Scully [124] that by establishing quantum coherence in a three-level atom, interference effects can be exploited to obtain a large index of refraction with vanishing absorption simultaneously. Scully's suggestion is essentially that when an excited state is coupled with two lower lying states that are prepared in a coherent superposition, the competing excitation paths may be configured such that there is complete destructive interference of the imaginary (absorptive) part and constructive interference of the real part of the susceptibility. This scheme results in a particular frequency band where the real part of the susceptibility is greatly enhanced and the absorption is negligible. This idea was further investigated theoretically [125, 38, 115, 95] and has been demonstrated experimentally [171, 113].

In the simplest sense Scully's suggestion may be understood by considering an ensemble of multiple two-level atoms with slightly different transition frequencies as shown in Fig. 2.1. In this system the two atoms are configured for gain and absorption transitions for a weak probe and have resonance frequencies ω_1 and ω_2, respectively. The first atom is prepared with a population inversion by an external pumping mechanism, such that stimulated emission by a resonant probe

beam results in gain for the probe field. The second atom is initially populated in the ground state and will absorb light from a resonant probe beam. These closely spaced gain and absorption resonances result in interfering interactions for a propagating probe beam and modify its effective susceptibility in the system. The interference from the superposition of these resonances can be exploited such that for some frequency ν , $\omega_1 < \nu < \omega_2$, a probe field can experience zero absorption and enhanced refractive index. However this scheme is problematic to implement experimentally because there is not a practical method to pump one of the atomic species to a population inversion while not pumping the other species that is to remain populated in the ground state.

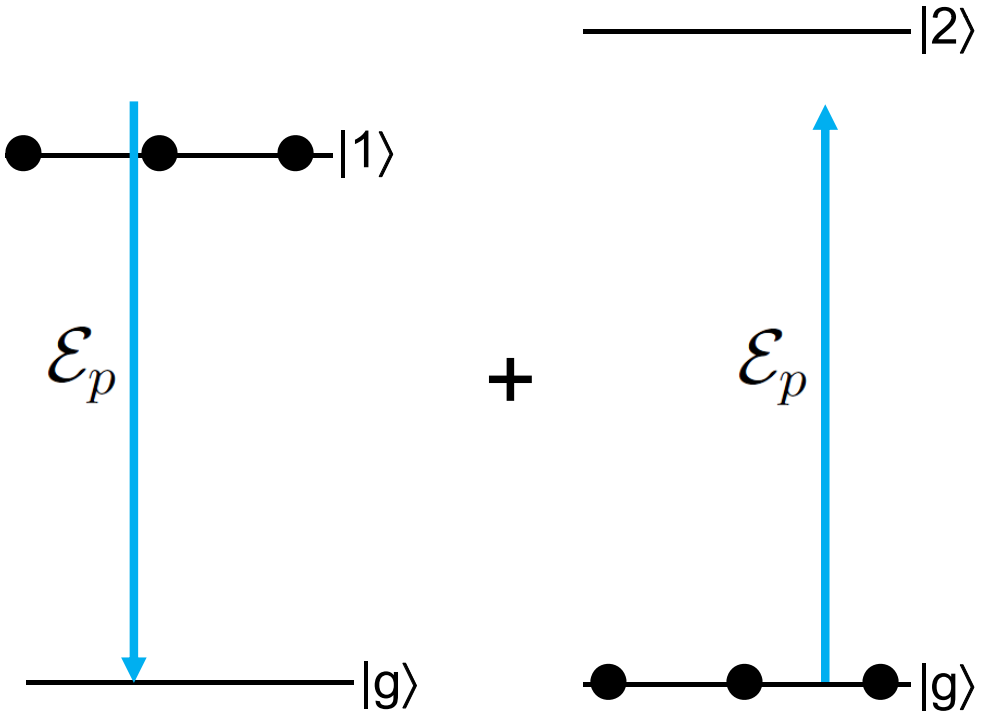

Figure 2.1 A system of 2, two-level atoms with closely spaced transition frequencies. The first pair of levels is prepared with population in the excited state $|1\rangle$ and the probe beam $\mathcal{E}_p$ experiences gain from the transition $|1\rangle \rightarrow |g\rangle$. The second pair of levels is populated in the ground state $|g\rangle$ and the probe beam experiences absorption from the transition $|g\rangle \rightarrow |2\rangle$. The competing transition processes cause interference effects that significantly alter the electric susceptibility of the probe beam.

The refractive index enhancement schemes considered in this thesis are based on a newly suggested approach in which the coherence of two lower states is prepared by a far-off resonant Raman transition [165]. Earlier relevant work has studied and demonstrated other novel effects of coherently driven atomic system such as coherent population trapping (CPT), lasing without inversion (LWI) [126, 68], and electromagnetically induced transparency (EIT) [49, 37]. EIT is a popular coherence effect that also results in a medium that has negligible absorption, though it is primarily concerned with achieving a steep dispersion (slope) of the refractive index rather than enhancing the value of the index itself.

The method that we will focus on is essentially the idea of interfering two closely spaced gain and absorption resonances that are derived from laser driven Raman transitions in an atomic vapor. By utilizing additional laser fields we are able create far-off resonant Raman resonances for a weak probe beam, which may be either absorptive or amplifying. Thus we are able to create the desired effect of Scully's interfering two-level systems without the unwanted complications of selective pumping. Additionally the ability to control the frequency separation of the Raman resonances offers an advantage over a scheme that has a fixed separation. The refractive index enhancement resulting from interference has a strong dependence on the separation of the resonances and this separation can be optimally selected in a Raman system. This scheme also offers a technical advantage in that the we have a larger bandwidth of potential probe frequencies since the probe beam does not have to be near resonance with an excited state.

2.2 Refractive index in two-level system

We now consider a more quantitative treatment of the refractive index of a weak probe beam propagating through a dilute atom vapor. Recalling results from the last chapter, we have the refractive index given by

$$n = \sqrt{\epsilon\mu} = \sqrt{(1+\chi_{\mathcal{E}})(1+\chi_{\mathcal{B}})}. \qquad [2.1]$$

In the majority of atomic interactions the magnetic susceptibility $\chi_{\mathcal{B}}$ is negligible and we can well characterize the refractive index by the electric susceptibility $\chi_{\mathcal{E}}$ alone. n and $\chi_{\mathcal{E}}$ are both complex

frequency dependent quantities. We denote $n = n' + in''$ where n' is the refractive index of the medium and n'' is the absorption coefficient and $\chi_\mathcal{E} = \chi'_\mathcal{E} + i\chi''_\mathcal{E}$ where $\chi'_\mathcal{E}$ and $\chi''_\mathcal{E}$ represent the dispersion and loss, respectively. For a weak probe beam in a two-level system the electric susceptibility is

$$\chi'_\mathcal{E} = \frac{N|d|^2}{\epsilon_0 \hbar} \frac{\delta}{\delta^2 + \Gamma^2} \quad ,$$
$$\chi''_\mathcal{E} = \frac{N|d|^2}{\epsilon_0 \hbar} \frac{\Gamma}{\delta^2 + \Gamma^2} \quad , \qquad [2.2]$$

where we have assumed all atoms are populated in the ground state. N is the number density of atoms or molecules, d is the electric dipole matrix element, δ is the detuning from resonance, and Γ is the decay rate of the excited state. In Fig. 2.2 we see that both the susceptibility and refractive index in frequency space have a dispersion curve centered at the resonant frequency. Here we note that the refractive index curve qualitatively correlates with the resonant behavior of the susceptibility and there is a correspondence of the curves extrema with the detuning from the resonant frequency plotted along the horizontal axis. This means we can well predict the resonance structure of the index of refraction and the absorption of the probe beam from the real and imaginary parts of the electric susceptibility, respectively. For the two level system the largest changes in the index of refraction occur at $\delta = \pm\Gamma$ and we have

$$|\chi'_\mathcal{E}|^{max} = \frac{N|d|^2}{\epsilon_0 \hbar} \frac{1}{2\Gamma}. \qquad [2.3]$$

However, at these detunings we also have undesirable condition that $\chi''_\mathcal{E} = \chi'_\mathcal{E}$, meaning there will be significant absorption when the index of refraction most strongly differs from unity. This concurrent absorption with the resonant enhancement of the index of refraction is true of all systems where the polarization is linear with respect to the probe beam electric field. Thus quantum coherence and interference techniques are required to achieve enhanced refractive index while maintaining low absorption.

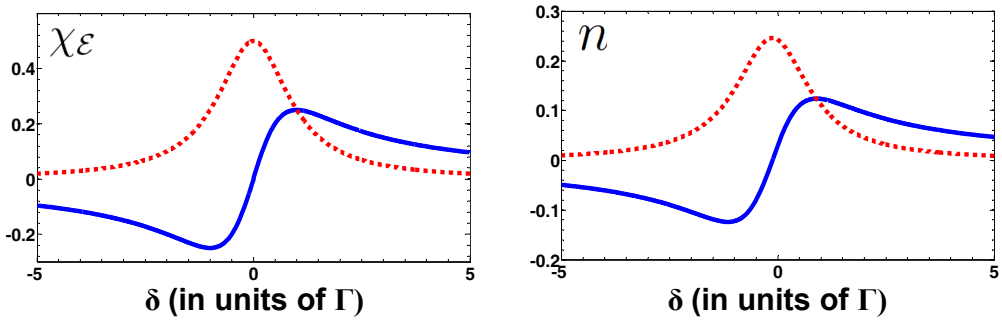

Figure 2.2 A comparison of the line shapes of the electric susceptibility, $\chi_{\mathcal{E}}$, and the relative refractive index, $n-1$, for a simple two-level absorption transition. Both the real (solid blue lines) and imaginary (red dotted lines) components of the two quantities exhibit dispersion curves with nearly the same width and corresponding locations of maxima and minima. Therefore the resonance behavior of the refractive index is well described by the susceptibility resonance.

2.3 Refractive index enhancement by interference

Now we will illustrate how Scully's suggestion achieves simultaneous enhanced refractive index without absorption by the interference of multiple two-level systems. We consider a medium that is a uniform mixture of the two atomic species that exhibit the two level transitions shown in Fig. 2.1. For simplicity we assume that the gain transition and absorption transitions have matching parameter values such that they will be of equal strength, however they will have distinct resonance frequencies, ω_1 and ω_2, respectively. Both resonances can be related to the same functional form of the two-level electric susceptibility given in Eq. (2.2), however both the real and imaginary parts for the gain resonance will have the sign flipped because of the complete population inversion of its levels. Quantitatively, interference arises in the electric susceptibility for the probe frequency, ω_p, from the superposition of the individual resonances, given by

$$\chi_{\mathcal{E}} = \frac{N\left|d\right|^2}{\epsilon_0 \hbar}\left[\frac{-1}{\delta_1 - i\Gamma} + \frac{1}{\delta_2 - i\Gamma}\right] \quad , \qquad [2.4]$$

where the detunings from the resonances are $\delta_1 = \omega_1 - \omega_g - \omega_p$ and $\delta_2 = \omega_2 - \omega_g - \omega_p$.

Ideally we wish these two resonances to be closely spaced, so that in the frequency band between the resonances there will be significant interference of their resonant features. In Fig. 2.3 we show the effect of interfering the gain and absorption resonances for different values of the

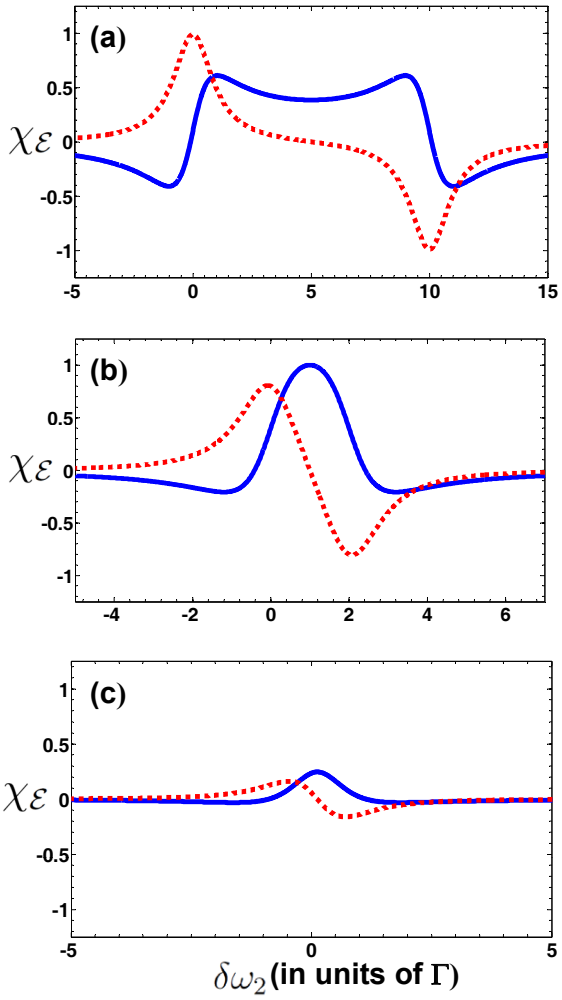

Figure 2.3 The real part $\chi'_{\mathcal{E}}$ (blue solid line) and the imaginary part $\chi''_{\mathcal{E}}$ of the susceptibility of the probe beam for closely spaced gain and absorption transitions separated by $\Delta = 10\Gamma$ in (a), $\Delta = 2\Gamma$ in (b), and $\Delta = 0.25\Gamma$ in (c). At the midpoint between the resonances , there is destructive interference in the imaginary part of the susceptibility resulting in vanishing absorption. At the same point the real part of the susceptibility is significantly increased due to constructive interference, which simultaneously yields an enhanced refractive index.

frequency spacing of the resonances,

$$\Delta = \omega_2 - \omega_1 \quad , \qquad [2.5]$$

in terms of the resonance line width, Γ. The plotted curves are the real and imaginary parts of the probe beam electric susceptibility which results from superimposing the resonances. The gain and

absorption resonant frequencies coincide with the negative and positive peaks of the imaginary part of the susceptibility, respectively. As is seen in the region between the resonances there is constructive interference of $\chi'_{\mathcal{E}}$ and destructive interference of $\chi''_{\mathcal{E}}$. For the case of equal strength resonances, there will be zero absorption for a probe beam when tuned midway between the resonances at $\omega_p = \frac{\omega_2+\omega_1}{2}$.

The effect of the interference depends strongly on the spacing of the resonances, Δ. When $\Delta \gg \Gamma$ there is little interference and the system behaves as two isolated resonances, as seen in Fig. 2.3(a). When $\Delta \ll \Gamma$ the resonances overlap and there is almost complete cancellation of any resulting resonant structure. The maximized constructive interference for $\chi'_{\mathcal{E}}$ that coincidences with $\chi''_{\mathcal{E}} = 0$, occurs for the optimal condition that the separation of the resonances is $\Delta = 2\Gamma$, as seen in Fig. 2.3(b). Thus we can achieve an enhanced index of the refraction for the probe beam while maintaining perfect destructive interference of its absorption coefficient.

2.4 Refractive index in far-detuned Raman system

A more practical method to experimentally implement this desired interference of resonances is to recreate the behavior of the ideal multiple two-level system by using Raman transitions. New probe beam resonances may be engineered using nonlinear approaches in a three-level system by coupling the probe beam with additional laser fields in two photon Raman transitions. By appropriately tuning the parameters of the additional lasers, the resonant frequency of the probe beam may be chosen and the nature of the resonance can be chosen to be either absorptive or amplifying for the probe field. Raman transitions are advantageous to implementing this interference scheme because we are able to select the probe resonance frequencies for the two transitions we wish to interfere. This way we are able to control the important dependence on the frequency separation of the resonances and we can optimally configure the interference conditions for enhanced refractive index with vanishing absorption.

In this scheme a weak probe beam, which has a large one photon detuning from an excited electronic state, and a strong control beam interact in a Raman transition between two low lying levels as seen in Fig. 2.4. In general a Raman transition is a two photon process, where the atoms

of a populated state absorb a photon of frequency ω_α and is, in a sense, "excited" to a virtual level, and then emits a photon of frequency ω_β, effectively transitioning the atom to the other low lying level. A two-photon resonance occurs when the energy spacing of the two lower levels matches the difference of the laser frequencies, which is given by

$$\delta E = \hbar(\omega_\alpha - \omega_\beta) \quad . \tag{2.6}$$

The lower levels are dipole forbidden from a direct one photon transition between the two, but they each have a dipole allowed transition with a higher energy excited electronic level. The role of the beams in the Raman transition can be configured for gain of the probe beam by selecting the probe and control beam frequencies ω_p and $\omega_\mathcal{C}$, respectively, such that $\hbar(\omega_\mathcal{C} - \omega_p) = \delta E$. Similarly there will be absorption of the probe beam for frequency selection satisfying $\hbar(\omega_p - \omega_\mathcal{C}) = \delta E$.

However it should be noted that it is tempting to conceptualize the Raman transition as a single atom absorbing and emitting photons, such that it is transferred between the two states, this is an inaccurate interpretation. Since quantum mechanics is statistical in nature and describes an ensemble of many atoms, the Raman transition should be viewed as establishing a quantum superposition of the atom being in either state rather than individual atoms transferring between states. With the ensemble of atoms in a coherent superposition, the dynamics of the collective atoms are well described by the coherence. The coherence is a quantum mechanical wave function of the time varying mixture of the quantum states of the system averaged over the ensemble and eliminates the need for individual atom statistics in modeling system dynamics.

In the scheme of interest, we consider a four level atomic or molecular system seen in Fig. 2.4. A weak probe beam, $\mathcal{E}_p$, is paired with two strong control beams, $\mathcal{E}_{\mathcal{C}1}$ and $\mathcal{E}_{\mathcal{C}2}$, to form two Raman transitions. The frequencies of the control beams will be chosen so that the Raman transitions will differ in which one will be amplifying and the other absorptive with respect to the probe beam. $\mathcal{E}_{\mathcal{C}1}$ will two-photon couple the ground state $|g\rangle$ to the excited Raman state $|1\rangle$ via a stimulated emission of $\mathcal{E}_p$ and similarly $\mathcal{E}_{\mathcal{C}2}$ will couple the excited state $|2\rangle$ via a stimulated absorption of $\mathcal{E}_p$. In the absence of the control beams the probe beams experience the usual largely detuned linear susceptibility of the one photon transition from the ground state to the excited electronic state $|e\rangle$. The presence of the control beams strongly modifies the susceptibility of the probe beam due to

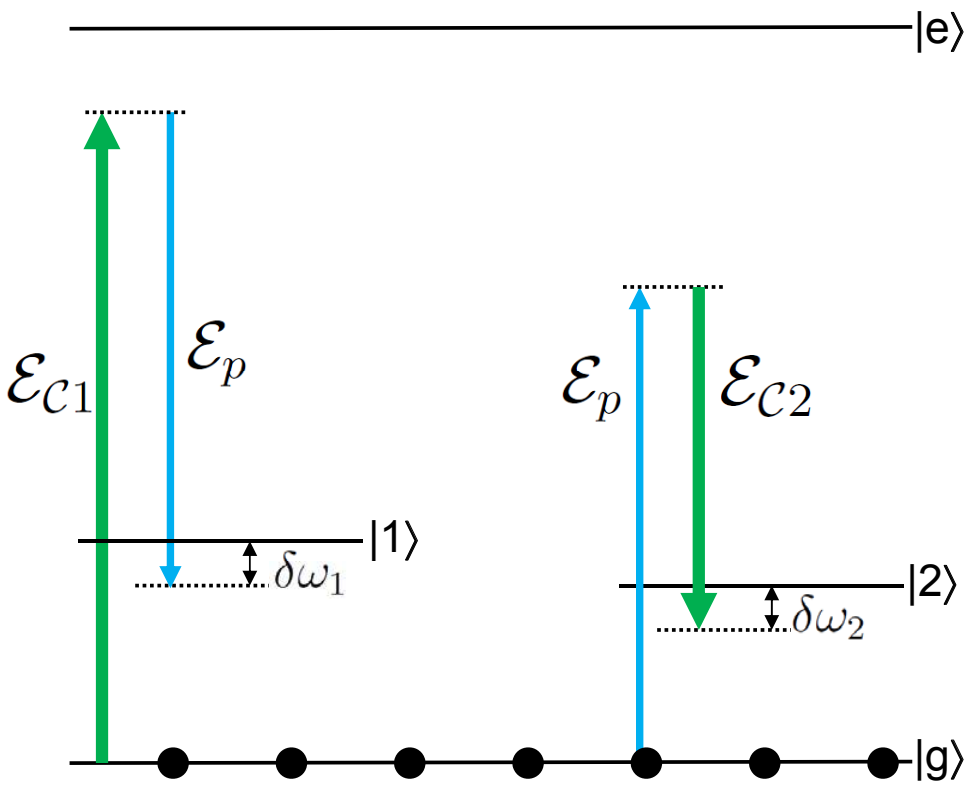

Figure 2.4 A scheme equivalent to Scully's suggested interfering system of two-level gain and absorption resonances. This more practical scheme uses Raman transitions of a far-off resonant probe beam induced by two control lasers, $\mathcal{E}_{\mathcal{C}1}$ and $\mathcal{E}_{\mathcal{C}2}$. By changing the excitation path from the ground level, a Raman resonance can effectively be a gain or absorption transition for the probe beam, $\mathcal{E}_p$

nonlinear interactions that correspond to new Raman resonances at frequencies determined by the control beam frequencies and the level separation of the ground state from the excited Raman states.

We proceed with an analysis of the scheme in Fig. 2.4. We follow the formalism of Harris et al. [48, 51, 167] and the full details are given in Appendix A. The two-photon detunings of the Raman resonances are defined as

$$\delta\omega_1 = (\omega_1 - \omega_g) - (\omega_{\mathcal{C}1} - \omega_p) \quad ,$$
$$\delta\omega_2 = (\omega_2 - \omega_g) - (\omega_p - \omega_{\mathcal{C}2}) \quad , \qquad [2.7]$$

where $\delta\omega_1$ and $\delta\omega_2$ correspond to the gain and absorption resonances, respectively. All of the lasers are far-detuned from the excited electronic state such that we may approximate that the population remains in the state $|g\rangle$ and we can adiabatically eliminate the dynamics of the excited state $|e\rangle$. From a semiclassical treatment of the quantum dynamics of the system, we evaluate a generated dipole moment at the probe frequency given by

$$P_p = 2\hbar N\Bigg(a_p \;+\; \frac{|b_1|^2\,|\mathcal{E}_{\mathcal{C}1}|^2}{2\left[\delta\omega_1 - \frac{Re(F_1-A)}{2} + i\left(\gamma_1 + \frac{Im(F_1)}{2}\right)\right]} + \frac{|b_2|^2\,|\mathcal{E}_{\mathcal{C}2}|^2}{2\left[\delta\omega_2 - \frac{Re(F_2-A)}{2} - i\left(\gamma_2 + \frac{Im(F_2)}{2}\right)\right]}\Bigg)\mathcal{E}_p \quad , \qquad [2.8]$$

where γ_1 and γ_2 are the Raman decay rates; $\mathcal{E}_p$, $\mathcal{E}_{\mathcal{C}1}$, $\mathcal{E}_{\mathcal{C}2}$ are the electric field amplitudes of the lasers; A, F_1, and F_2 are higher order intensity dependent shifts; a_p, b_1, and b_2 are Raman coupling coefficients that contain electric dipole matrix elements and one photon detunings. Using the relation $P_p = \epsilon_0\chi_{\mathcal{E}}\mathcal{E}_p$ with Eq. (2.8), we can find the susceptibility of the medium for the probe wave

$$\chi_{\mathcal{E}} = \frac{2\hbar N}{\epsilon_0}\left(a_p + \frac{|b_1|^2}{2\left[\delta\tilde{\omega}_1 + i\tilde{\gamma_1}\right]}\,|\mathcal{E}_{\mathcal{C}1}|^2 + \frac{|b_2|^2}{2\left[\delta\tilde{\omega}_2 - i\tilde{\gamma_2}\right]}\,|\mathcal{E}_{\mathcal{C}2}|^2\right) \quad . \qquad [2.9]$$

In the above expression we have used the notation $\delta\tilde{\omega}_1$, $\delta\tilde{\omega}_2$, $\tilde{\gamma_1}$, and $\tilde{\gamma_2}$ as defined in Appendix A to suppress the stark shifts and power broadenings of the detunings and decay rates, respectively, for convenience. The first term in the susceptibility represents the background susceptibility of the far-detuned one photon transition of the probe beam with the excited electronic state and is typically negligible compared to the second and third terms which represent the Raman gain and absorption resonances, respectively.

These two Raman transitions allow us to create the interference described in Scully's suggestion by the ability to move the resonant frequency positions by appropriately choosing the control laser frequencies, $\omega_{\mathcal{C}1}$ and $\omega_{\mathcal{C}2}$. Ignoring the effect of stark shifts for now, the two resonances occur when the probe laser wavelength is chosen such that $\omega_p = \omega_g + \omega_{\mathcal{C}1} - \omega_1$ $(\delta\omega_1 = 0)$ or $\omega_p = \omega_2 + \omega_{\mathcal{C}2} - \omega_g$ $(\delta\omega_2 = 0)$. The separation of the resonances in frequency space is given by

$$\Delta = \delta\tilde{\omega}_1 + \delta\tilde{\omega}_2 \quad . \qquad [2.10]$$

For the case of equal transition matrix elements and laser parameters such that the resonances are of equal strength, there is perfect destructive interference of the imaginary part of the susceptibility when the probe frequency is tuned midway between the resonances, equally detuned from each one. This point of vanishing absorption is satisfied by the condition that $\delta\tilde{\omega}_1 = \delta\tilde{\omega}_2 = \Delta/2$. With this condition for vanishing absorption we may express the real part of the susceptibility (neglecting the background contribution) as

$$\chi'_{\mathcal{E}} = \frac{2\hbar N}{\epsilon_0}\left(\frac{|b_1|^2\,(\Delta/2)}{\left[(\Delta/2)^2 + \tilde{\gamma_1}^2\right]}\,|\mathcal{E}_{\mathcal{C}1}|^2\right) \quad . \tag{2.11}$$

Recalling from the last section that the individual resonances have extrema for their real part when detuning matches the linewidth, it can be shown that the constructive interference in $\chi'_{\mathcal{E}}$ is optimized for equal strength resonances, when the spacing between the resonances is $\Delta = 2\tilde{\gamma_1}$. With this condition the optimized susceptibility is given by

$$\chi'_{\mathcal{E}} = \frac{2\hbar N}{\epsilon_0}\left(\frac{|b_1|^2}{[2\tilde{\gamma_1}]}\,|\mathcal{E}_{\mathcal{C}1}|^2\right) \quad . \tag{2.12}$$

In the limit of very large intensity values of the control beam, the power broadened linewidths of the resonances $\tilde{\gamma_1}$ will saturate the susceptibility and the maximum susceptibility that can be attained by increasing the control intensity is

$$\chi'_{\mathcal{E}} = \frac{N}{\hbar\epsilon_0}\frac{|d_{ge}|^2}{2\Gamma_e} \quad . \tag{2.13}$$

Thus for sufficiently intense control beams, this far-off resonant Raman scheme can attain a $\chi'_{\mathcal{E}}$ that matches that for a near-resonant one-photon excited state transition given in Eq. (2.3), however, while maintaining vanishing absorption. It should be noted that the susceptibility can not be made arbitrarily large by sufficiently increasing the particle density, N, because at high densities the susceptibility will saturate because of increased pressure broadening and other higher order effects.

This implementation of refractive index enhancement by interfering Raman transitions suggested by Yavuz [165] has been initially demonstrated in a proof of principle experiment [113] and is the topic of continuing experimental research [135]. These experiments are performed in a magnetically shielded, temperature controlled vapor cell containing a natural isotopic abundance

of rubidium atoms with diatomic nitrogen as a buffer gas, as shown in the schematic of Fig. 2.5. A weak probe beam with two strong control beams are far detuned from the excited $5P_{3/2}$ (D_2 line) near a wavelength of $\lambda = 780.2$nm. The Raman coupling of the hyperfine levels of the $5S_{1/2}$ ground state by the lasers induces the interfering amplifying and absorptive resonances. Optical pumping lasers are included to selectively populate the ground state hyperfine levels for the appropriate excitation configurations.

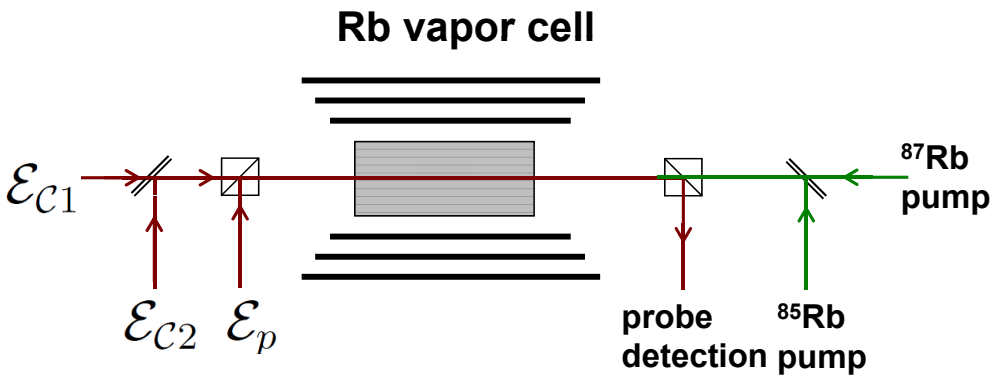

Figure 2.5 Simplified experimental schematic. The experiment is performed in a magnetically shielded, natural abundance rubidium vapor cell with a length of $L = 1$mm. The three experimental beams, $\mathcal{E}_p$, $\mathcal{E}_{C1}$, and $\mathcal{E}_{C2}$, are obtained by appropriate frequency shifting and amplifying the output of a single master external cavity diode laser. After the cell, the probe laser beam is separated with a high extinction polarizer and measurements are performed. Some experiments utilize optical pumping lasers, which propagate in the direction opposite the experimental laser beams

In the configuration of the most recent experiment, shown in Fig. 2.6, atoms are optically pumped to the $F = 3$ level of the ^{85}Rb and Raman transitions couple this state to the $F = 2$ level. For a 1 mm long Rb cell with a density of $N = 1.8 \times 10^{14}$ cm^{-3}, Raman linewidth $\gamma \sim 1$MHz and a one-photon resonance detuning $\delta \approx 7$GHz, the experimentally observed interference of the resonances is plotted in Fig. 2.7 as the probe frequency is scanned. The imaginary part of the refractive index is calculated by measuring the probe intensity at the end of the cell, the relative change of the intensity, (I_{out}/I_{in}), and the cell length, L. The data for n'' is then fit to a model that assumes each resonance has a Lorentzian line shape and n' is inferred from the

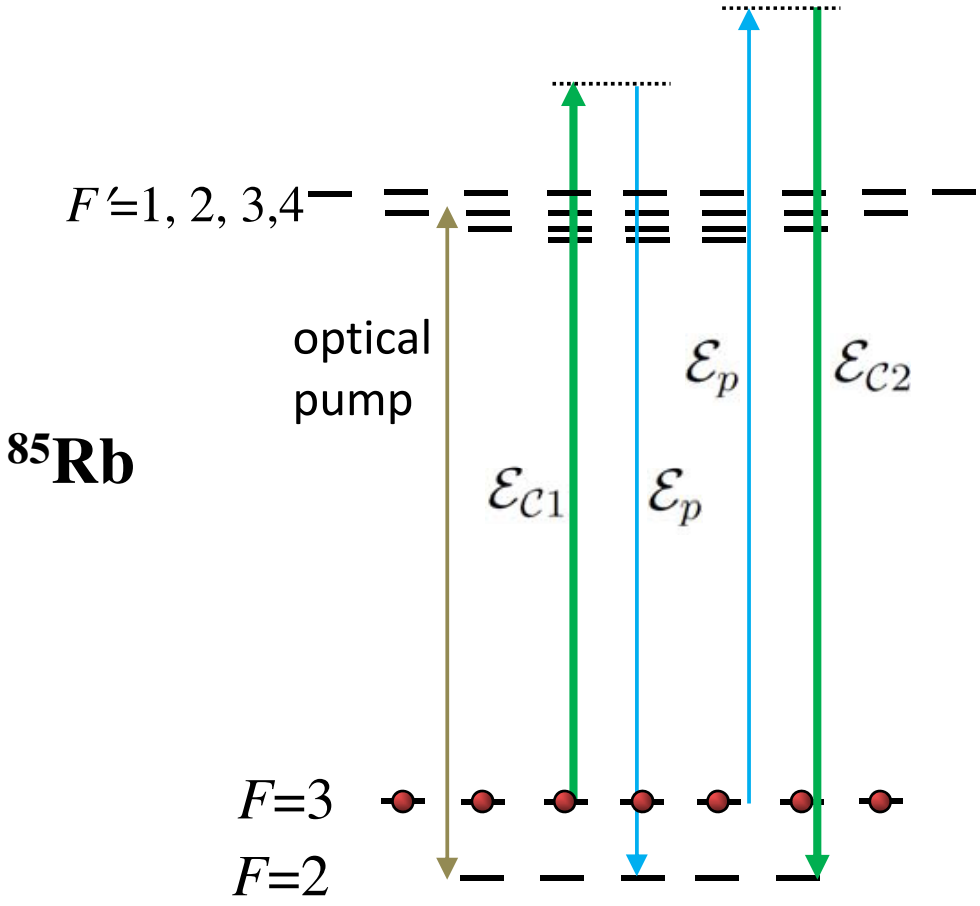

Figure 2.6 Refractive index enhancement in ^{85}Rb level structure. The system is optically pumped to the $F = 3$ level and two Raman transitions are induced. The spacing between the $F = 2$ and $F = 3$ levels is 3.035 GHz.

real part of the Lorentzian curves. A relative change in the refractive index of $\Delta n = 0.4 \times 10^{-4}$ with low absorption was observed in the data shown in Fig. 2.7. Future efforts are working toward improving the change in the refractive index by resolving unexplained power broadening and preparing ultracold ^{87}Rb atoms in a magneto-optical trap and dipole trap.

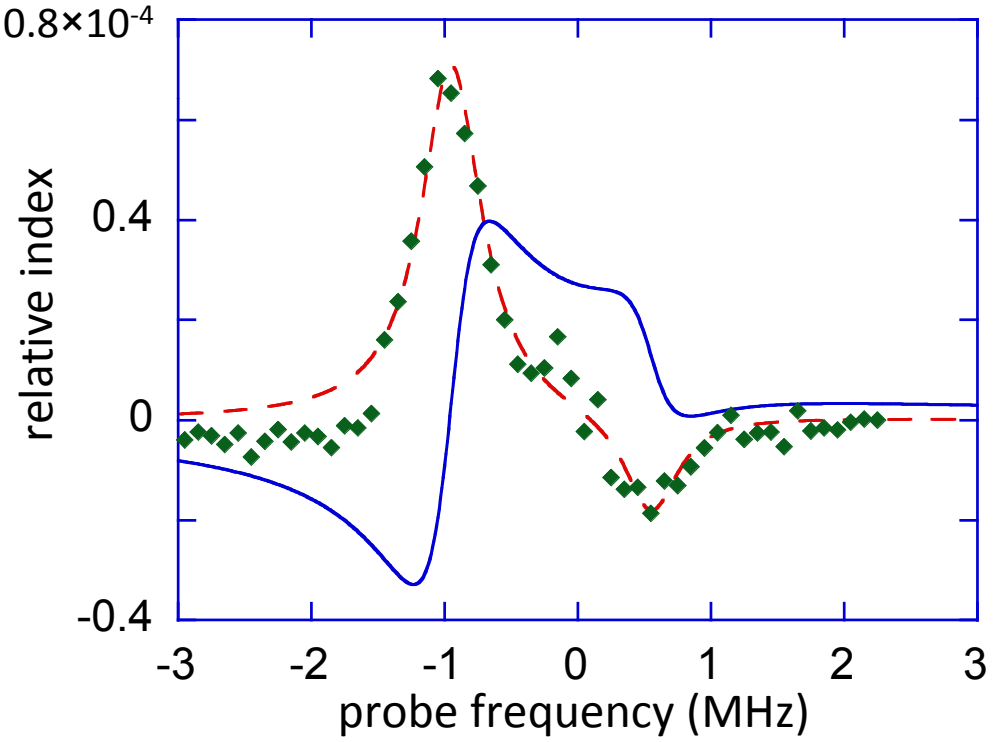

Figure 2.7 The real (solid blue lines) and imaginary (data points and dashed red line) parts of the refractive index when the two Raman resonances are combined. The dashed lines are fits to the data that assumes each Raman resonance to have a Lorentzian line shape. The solid lines are the calculated real part of the refractive index based on these fits. A change in the refractive index of $\Delta n \approx 0.4 \times 10^{-4}$ with low absorption is observed.

2.5 Summary

This novel nonlinear optic technique provides an effective way to modify the susceptibility and hence the refractive index of a weak probe beam and greatly reduce absorption. This scheme offers straightforward ways to manipulate the susceptibility by tuning laser frequencies and varying the control beam intensities. The far-detuned characteristic of the scheme presents an advantage over other schemes in that it can be applied to a potential range of probe beam frequencies since the probe frequency is not required to be near resonance with the level structure that is available. The configurable nature of the Raman resonances also allows us to create a system of closely spaced gain and absorption transitions without requiring selective pumping complications. This scheme

also provides a practical alternative from EIT based techniques to eliminate resonant absorption. Its ability to modify the refractive index may potentially be useful in schemes to achieve negative refraction in non-metamaterial systems.

Chapter 3

An overview of negative refractive index

3.1 Veselago's thought experiment

The concept of negative refractive index is a topic that has generated much interest over the last decade. The idea was published over four decades ago by Veselago, where in a thought experiment he considered a physical system that corresponds to taking the negative branch cut of the square root of the expression, $n^2 = \epsilon\mu$, that results from Maxwell's equations. It was found that in order for a system to have $n < 0$, it required the condition that simultaneously the system must have $\epsilon < 0$ and $\mu < 0$. When these conditions are met and used as parameters in Maxwell's equations, there result some novel changes from traditional behavior of electromagnetic radiation. Among these changes is a "left-handed" triad of the vectors $\vec{E}$, $\vec{B}$, and $\vec{k}$, inverted Snell's law, reversed Doppler effect, and reversed Cherenkov effect [152]. The left-handed triad represents a system where the wave vector $\vec{k}$ is antiparallel to the Poynting vector, $\vec{S} = \frac{1}{\mu_0}\vec{E} \times \vec{B}$, which implies the propagation directions of the phase velocity and group velocity are oppositely oriented. This backward wave motion has been colloquially compared to the popularized dance called "Moon Walking" because of the paradoxical backward motion that accompanies forward stepping. These unusual properties and the requirement for negative permittivity and permeability have manifested in the many names that have been used for negative index materials (NIM) such as left-handed, backward wave, and double negative materials. Currently there is much intense research effort in developing NIMs [137, 39, 131, 56, 101, 23, 24, 168, 36, 128, 17, 160, 170, 28, 29, 118, 75] and developing applications for the unique electromagnetic properties of such materials [139, 91, 36, 90, 57], in particular, a NIM lens with perfect resolution [104].

The refractive index is related to the product of ϵ and μ and since the product of two negatives is positive valued, it is unclear why n should be negative when this is the case. To examine the logic behind the appropriate choice of branch cuts in the refractive index for the cases $n = \pm\sqrt{(+\epsilon)(+\mu)} \Rightarrow +\sqrt{\epsilon\mu}$ and $n = \pm\sqrt{(-\epsilon)(-\mu)} \Rightarrow -\sqrt{\epsilon\mu}$, we consider the role of ϵ and μ in Maxwell's equations. From the constitutive relations and equations

$$\vec{D} = \epsilon\epsilon_0\vec{E} \quad , \quad \vec{B} = \mu\mu_0\vec{H} \quad , \tag{3.1}$$

$$\nabla \times \vec{E} = -\frac{\partial \vec{B}}{\partial t} \quad , \quad \nabla \times \vec{H} = \frac{\partial \vec{D}}{\partial t} \quad , \tag{3.2}$$

if we consider a monochromatic plane wave that propagates in space-time as $e^{i(\vec{k}\cdot\vec{r}-\omega t)}$, we can derive the expressions

$$\vec{k} \times \vec{E} = \omega\mu\mu_0\vec{H} \quad , \quad \vec{k} \times \vec{H} = -\omega\epsilon\epsilon_0\vec{E} \quad , \tag{3.3}$$

that show how the orientation of the vectors $\vec{E}$, $\vec{B}$, and $\vec{k}$ depend on the signs of ϵ and μ. For $\epsilon > 0$ and $\mu > 0$ there is a right-handed triad $\vec{E} \times \vec{B} = \vec{k}$ and for $\epsilon < 0$ and $\mu < 0$ the triad is left-handed $\vec{E} \times \vec{B} = -\vec{k}$. This sign dependent orientation relationship can also be inferred by considering the boundary conditions of a light ray being refracted while traveling through two media with opposite signed ϵ and μ values as seen in Fig. 3.1. The medium on the incident side has $\epsilon_1 = 1$ and $\mu_1 = 1$ and the transmitted side has $\epsilon_2 = -1$ and $\mu_2 = -1$. The continuity of the transverse and normal field components required by the interface boundary conditions

$$E_{t1} = E_{t2} \quad , \quad H_{t1} = H_{t2} \quad , \tag{3.4}$$

$$\epsilon_1 E_{n1} = \epsilon_2 E_{n2} \quad , \quad \mu_1 H_{n1} = \mu_2 H_{n2} \quad , \tag{3.5}$$

results in a sign flip of the normal component of the field vectors in the negative medium. This sign flip of vector components combined with the fact that the energy flux moves in the direction of the Poynting vector, determined by $\vec{E} \times \vec{B}$, results in the ray being refracted at a negative angle with respect to the interface normal. Thus $\epsilon < 0$ and $\mu < 0$ lead to a geometry with negative refraction and the appropriate branch cut is $n = -\sqrt{\epsilon\mu}$, which is consistent with Snell's law.

Since Veselago's initial contemplation of the implications of negative refractive index, the idea remained an academic curiosity due to the fact that there are no known systems in nature that

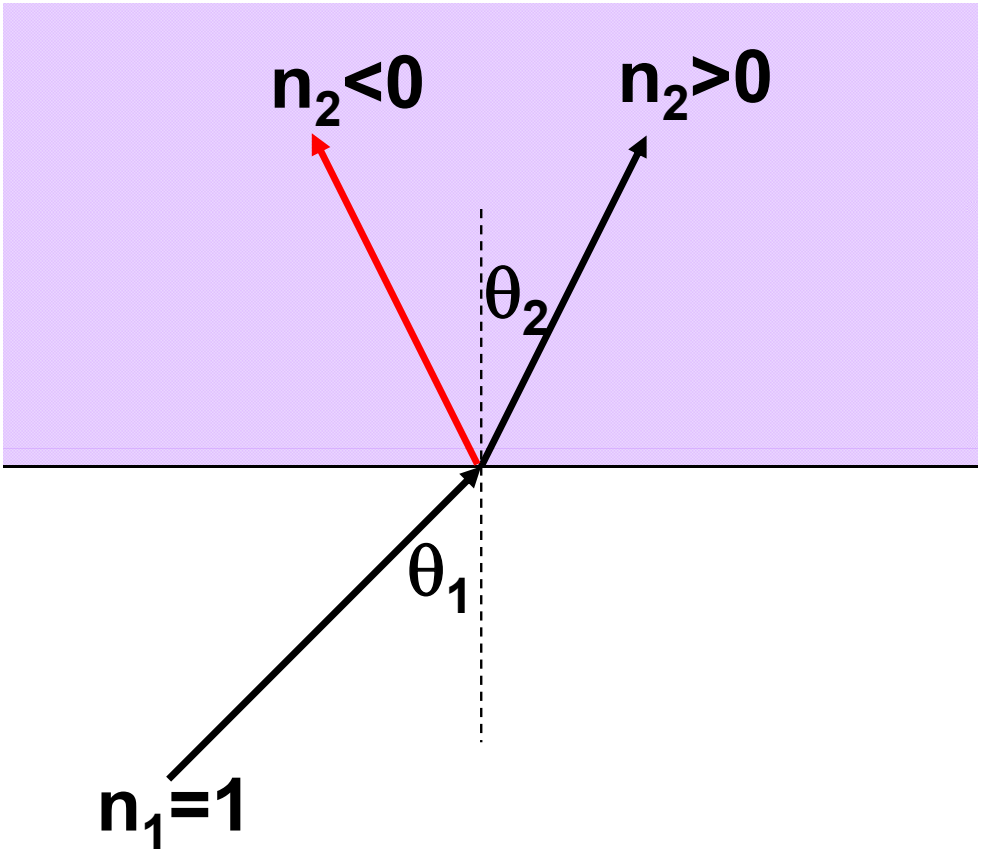

Figure 3.1 The simplest interpretation of a material possessing a negative refractive index is the demonstration of refraction of an incident beam with a negative angle for the transmitted beam, as determined by utilizing Snell's law with $n < 0$. Materials possessing negative refractive index were considered by Veselago in 1968 and negative refraction was experimentally demonstrated in 2001 using metamaterials.

simultaneously have $\epsilon < 0$ and $\mu < 0$. It is well known that in both nature and the laboratory there exist plasmas of electric charges that exhibit negative permittivity for certain ranges of frequencies. In a cold plasma of electrons with no magnetic field, the permittivity is given by

$$\epsilon(\omega) = 1 - \frac{\omega_{ep}^2}{\omega^2} \quad , \qquad [3.6]$$

where $\omega_{ep}^2 = \frac{Ne^2}{m_e \epsilon_0}$ is the square of the electron plasma frequency, with number density, N, electron charge, e, and electron mass, m_e [44]. Clearly, the permittivity will be negative for frequencies

below the plasma frequency and the refractive index will be imaginary. Veselago proposed a hypothetical material that consisted of a plasma of magnetic “charges” with an effective magnetic plasma frequency that could analogously provide a route to negative permeability. However, since magnetic monopole “charges” are not known to exist, the challenge of realizing a negative refractive index persisted for many years. In the late 1990’s John Pendry discovered a new approach to achieving negative permeability in the developing field of metamaterials.

3.2 Metamaterials

Metamaterials, named after the Greek word “meta” meaning “beyond”, are artificial materials that have properties that result from macroscopic structures, termed “meta-atoms”, that interact with propagating electromagnetic fields in analogy to the atoms or molecules of natural materials as described in Chap. 1. The meta-atoms are conducting structures with practical dimensions that are designed for particular resonant frequencies. These resonant structures behave like electric or magnetic dipoles and may become polarized through their interaction with light and establish a net dipole moment in the material. A metamaterial is a structure with an ordered lattice of meta-atoms such that the lattice spacing is much smaller than the wavelength of the propagating light. This subwavelength periodicity allows the material to be considered by an effective medium model and a homogeneous permittivity and permeability well describe its macroscopic electromagnetic properties. The resulting homogeneous interaction with light distinguishes metamaterials from other periodic structured materials, such as photonic crystals, where the periodicity is on the order of the wavelength and diffractive effects cause inhomogeneous polarization.

The advantage offered by metamaterials is the ability to directly engineer the electromagnetic properties of the material for qualities that are superior or not found in nature. In order to manipulate the electromagnetic interactions of a system it requires access to the resonant scatterer (i.e. the atom or molecule) and the ability to modify its resonant behavior. One approach to this was considered in the last chapter, where nonlinear optics techniques were used to manipulate the quantum interactions of the atom that determine the permittivity. Metamaterials use an alternative approach to the problem in which the light scattering meta-atoms are custom fabricated for the

desired resonant behaviors. The meta-atom structures are fabricated macroscopically with conducting elements arranged in various geometries that resemble antenna configurations (such as straight wires and loops). The materials and geometries are designed to have resonant frequencies that can differ greatly from the natural resonances of bulk samples of the constituent materials. Ideally these resonant frequencies correspond to a wavelength that is much larger than the physical dimensions of the meta-atom itself. In this long wavelength regime, the metamaterial exhibits an artificial homogeneous polarizability that is derived from the structured dipole characteristics of the meta-atoms rather than the constituent atoms or molecules. When the resonant wavelength approaches the unit cell dimensions of the lattice there is a break down of the collective polarization due to Bragg effects occurring similar to x-ray diffraction in solids. This presents a difficulty for metamaterials to operate at higher frequencies because of the reduced practicality in fabricating smaller resonant structures.

The forerunner of metamaterials was in the creation of artificial dielectrics by Kock in 1948, who by analogy with the oscillating molecular dipoles of dielectric materials in response to light, reasoned that the dipoles that result from the flow of electrons in metal under an alternating electric field could change the phase velocity of an incident radio wave. He used the effective medium model to design a radio wave lens from a three dimensional array of metallic elements with subwavelength spacing [69]. Later in 1962, Rotman constructed an artificial dielectric material from an array of conducting metal rods with a dielectric response similar to that of electric plasmas, with a characteristic plasma frequency, to simulate the electrodynamics of plasmas [119]. This rodded structure was modified by Pendry et. al. in the mid 1990s by using thin metal wires as array elements and experimentally verified that the permittivity was negative at frequencies below the plasma frequency [106]. Expanding upon this idea in 1999, Pendry was also able to create a metamaterial with a diamagnetic response from nonmagnetic materials by using meta-atom structures called split ring resonators [109]. The diamagnetic properties of this array of split ring resonators possessed an effective magnetic plasma frequency and successfully simulated an artificial magnetic plasma, which could achieve the previously unattainable negative permeability. Soon after this in 2000, Smith and Schultz et. al, in collaboration with Pendry, developed a composite metamaterial

of straight wires and split ring resonators that possessed both negative permittivity and permeability in the same microwave frequency band at 10.5 GHz [138] and were able to experimentally verify Veselago's prediction of negative refraction [131, 137].

Since this demonstration of negative refraction, the field of metamaterials has grown rapidly, investigating new physics owing to the ability to synthesize resonance characteristics not found in natural materials. The first metamaterials were designed in the RF and microwave regime and there is much active research in developing for the optical regime. Metamaterials have been considered for new nonlinear optical components, where the meta-atom lattices are designed to mimic the characteristics of photonic crystals. One particularly interesting topic emerging from metamaterials is that of transform optics [155, 107, 74, 123] and its potential for electromagnetic cloaking [122, 73, 148].

3.3 Pendry's lens

The concept of negative refractive index and its experimental demonstration were important new advances in science that opened up new areas of electromagnetic theory, but the rapid interest in this subject over the last decade is attributed to Pendry's proposed perfect lens as a practical application of this new physics. This perfect lens made from a negative index material would not only improve the resolution beyond the diffraction limit, but would, in principle, allow infinite resolution and perfect imaging. Perfect imaging means that every single detail of the object is reproduced in the image, including both propagating and evanescent wave components.

In Veselago's original paper he explored one of the unique variations from traditional electromagnetic theory when he postulated a flat lens created from a NIM with $n = -1$. Veselago noted that the geometry associated with the negative angle of refraction from Snell's law would allow light from a point source to be focused by a planar lens as seen in Fig. 3.2. In a geometrical optics treatment, rays from a point object are negatively refracted at the lens, brought to a focus inside the (sufficiently thick) lens, and then negatively refracted outside the lens into a focused point image. Initially this flat planar lens was of interest because the lens did not possess an optical axis and was free from spherical aberrations that affect non-paraxial rays in a conventional lens.

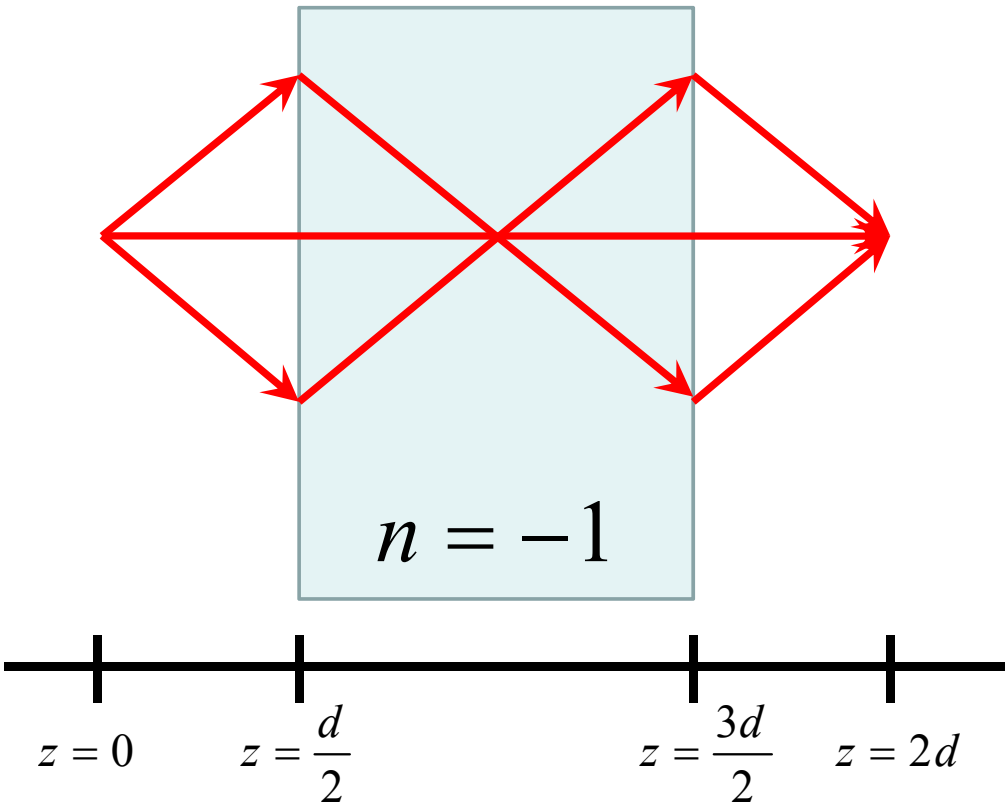

Figure 3.2 A flat slab lens made of a negative index material. For a planar lens with thickness d and $n = -1$, the object should be a distance $d/2$ in front of the lens and image will be formed a distance $d/2$ behind the lens. The negative refractive index bends light to a negative angle such that light initially diverging from a point source is focused to a point inside the lens, then diverges and is focused to a point again upon refraction when exiting the lens.

In Pendry's formative 2000 paper [104], he performed a Fourier optic analysis of a planar NIM lens beyond the geometric optics consideration by Veselago. Pendry considered a similar setup of a planar lens of material possessing $\epsilon' = \mu' = -1$ and $\epsilon'' = \mu'' = 0$ with thickness d placed a distance $d/2$ from a point source object. The wavefront is traveling in the $+z$ direction and the lens in the transverse plane. For this setup the dispersion relation,

$$k_0^2 = k_\perp^2 + k_z^2 = n^2 \left(\frac{\omega}{c}\right)^2 \quad , \qquad [3.7]$$

is the same both inside and outside the lens since $n^2_{freespace} = n^2_{lens} = 1$. For the case of propagating wave components, where $k_0^2 > k_\perp^2$, we have the components

$$k_{z,freespace} = +\sqrt{k_0^2 - k_\perp^2} \quad , \tag{3.8}$$

$$k_{z,lens} = -\sqrt{k_0^2 - k_\perp^2} \quad , \tag{3.9}$$

where the choice of sign for the square-root is determined by the $+z$ directed transport of energy and the relationship of the wave vector with the Poynting vector. In free space the wave vector and Poynting vector are parallel and we have the expected result that the wave accumulates phase as it propagates in the $+z$ direction. However, inside the NIM lens, the wave vector is anti-parallel and there is an unusual phase reversal of the wave as it travels through the lens. For wave components that are propagating, the negative phase reversal enables the medium to focus light by canceling the phase acquired by the light as it travels through free space. In the geometry shown in Fig. 3.2, the phase accumulation follows as

$$\phi\left(z = 2d\right) = \phi\left(z = 0\right) + \sqrt{k_0^2 - k_\perp^2}\frac{d}{2} - \sqrt{k_0^2 - k_\perp^2}d + \sqrt{k_0^2 - k_\perp^2}\frac{d}{2} = \phi\left(z = 0\right) \quad . \tag{3.10}$$

In imaging with a conventional lens the task is to correct the phase of propagating wave components emitted from an object but there is no way to prevent the decay in amplitude of the evanescent components. However, in a NIM lens the evanescent waves experience an "amplifying" enhancement of the amplitudes that distinguish negative index imaging systems from conventional positive index lenses. For the case of evanescent wave components, where $k_0^2 < k_\perp^2$, we have the z components

$$k_{z,freespace} = k_{z,lens} = +i\sqrt{k_\perp^2 - k_0^2} \quad , \tag{3.11}$$

where in both cases the value is positive and imaginary. The transmission coefficients solved from a wave scattering analysis of the system [104, 140] shows that

$$T_{freespace} = \exp\left(ik_{z,freespace}z\right) \quad , \tag{3.12}$$

$$T_{lens} = \exp\left(-ik_{z,lens}z\right) \quad , \tag{3.13}$$

and then plugging in the values of the wave vector components we have

$$T_{freespace} = \exp\left(-\sqrt{k_\perp^2 - k_0^2}z\right) \quad , \tag{3.14}$$

$$T_{lens} = \exp\left(+\sqrt{k_\perp^2 - k_0^2}z\right) \quad . \tag{3.15}$$

These transmission coefficients correspond to the expected exponential decay of Fourier amplitude for waves progressing in free space but there is a unique exponential growth of the amplitude in the negative index material. For perfect imaging with a negative index lens the amplitude growth inside the NIM should cancel out the decay in free space, thus the amplitude values resolved at the image perfectly match the initial values emitted from the object. Looking at the geometry shown in Fig. 3.3, the total Fourier transfer function for evanescent components of the system follows as

$$\begin{aligned} A\left(z=2d\right) &= A\left(z=0\right)\exp\left(-\sqrt{k_\perp^2 - k_0^2}\frac{d}{2}\right)\exp\left(+\sqrt{k_\perp^2 - k_0^2}d\right) \quad \exp\left(-\sqrt{k_\perp^2 - k_0^2}\frac{d}{2}\right) \\ &= A\left(z=0\right) \end{aligned} \tag{3.16}$$

which reproduces the original value.

The apparent "amplification" of the evanescent Fourier component amplitudes does not violate conservation of energy because evanescent waves do not transport energy in a lossless material. The physical mechanism for this amplification is related to excitations of surface waves by the incident light at the rear boundary of the NIM. These excitations are similar to surface plasmons that occur at dielectric interfaces of metals such as gold and silver, where incident light induces collective surface charge or current oscillations that propagate along the interface [108, 140]. These surface wave excitations at the NIM interface result for evanescent wave components that experience a sign change in the permittivity (permeability) when a TM (TE) wave crosses over the boundary. The fact that surface plasmons only require a single parameter to be negative (ϵ or μ) and not both, has inspired near-perfect lens designed from thin films of gold and silver [104, 36], which naturally have negative permittivity at optical frequencies. Studies of these thin metal layer lens have shown experimental verification of evanescent amplification [77]. These kinds of surface wave excitations are the topic of much active research in the field of plasmonics which is closely

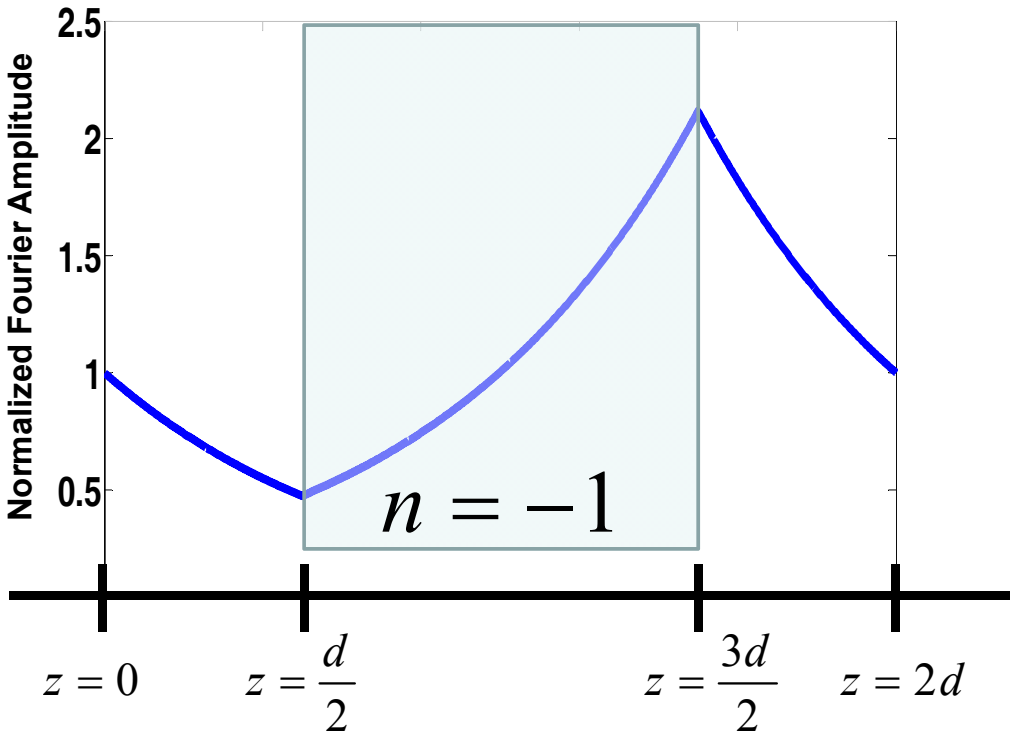

Figure 3.3 The amplitude decay and amplification for nonpropagating wave components passing through a negative index material. Evanescent wave fronts, with $k_0^2 < k_\perp^2$, experience exponential decay in positive index materials and are unable to be focused by traditional lenses. A planar lens constructed of negative index material, with a thickness that matches the optical path length in the positive index material, experiences an exponential growth that counteracts the loss and is able to restore the evanescent amplitude to its original value.

related to the developing field of metamaterials. It is important to note that metal lenses with exclusively negative ϵ or μ would only be able to focus evanescent Fourier components, whereas a NIM with both ϵ and μ negative would focus both propagating and evanescent waves.

The ability of the lens to counter both the phase accumulation and amplitude decay of propagating and evanescent waves, respectively, allows all spatial features of the object to be resolved in the image. This design is termed a perfect lens because there is no wavelength dependent obstacle to perfect imaging of the object beyond practical limitations of apertures, perfection of the lens surface, and homogeneity of the lens material. However, these practical limitations are not trivial.

The physical possibility of a perfect lens using negative refractive index still remains as a widely considered question. One of the idealized necessary conditions for a perfect lens is that it has no losses, where ϵ'' and μ'' are both zero. As a consequence of this there would be an unbounded growth of the evanescent amplitudes for a sufficiently thick negative index lens, which is physically unreasonable. The presence of losses in the material would also imply frequency dispersion by Kramers-Kronig relations and other effects that would complicate imaging, such as plasmon resonance frequency cut-offs. In a sense, the concept of a negative index perfect lenses is similar to other conceptual idealizations of physical systems, such as a Carnot engine. A Carnot engine is a hypothetical construct of a perfectly reversible mechanical thermodynamic system that operates at the maximum theoretical limit of efficiency and requires an ideal condition that there is zero change in the entropy of the system. It may be that it is indeed impossible to truly create a perfect lens, but like the Carnot engine, research efforts concerning perfect lenses provide important insights that can be applied to advances in practical near-perfect imaging [139, 91, 36, 90, 57].

Chapter 4

Raman approach for negative refractive index in atomic systems

4.1 Introduction and background

Since the publication of Pendry's suggestion for a perfect lens using negative refractive index materials and the experimental verification of negative refraction there has been continually growing interest in the topic over the last decade. In particular there have been a large number of novel theoretical developments and experimental advances demonstrated in negative refraction using metamaterials [137, 39, 131, 56, 101, 23, 24, 168, 36, 128, 17, 160, 170, 28, 29, 118, 75]. As we mentioned in the last chapter metamaterials are artificially constructed with periodic metal-dielectric structures with appropriate electric and magnetic resonances to engineer the polarization and magnetization responses beyond those of the constituent materials. These structures typically have a characteristic periodicity scale smaller than the wavelength, so that according to effective medium theory, a nearly uniform electromagnetic response is obtained. Initial experiments have demonstrated negative refraction in the microwave region of the spectrum using metamaterials constructed from metal wires and split-ring resonators [131, 56, 101, 23, 24]. The requirement that the resonant structure unit cell dimensions remain much smaller than the wavelength presents a practical challenge to designing metamaterials that can achieve negative refraction in the optical region of the spectrum. Recently, utilizing advances in nanolithography techniques, several groups have reported a negative index of refraction at optical frequencies in metal-dielectric nanostructures and photonic crystals [168, 36, 128, 17, 160, 170, 28, 29, 118, 75]. A key difficulty of these experiments that is particularly pronounced in the optical domain is the large absorption that accompanies negative refraction. For all experiments that have been performed in the optical region

of the spectrum, the imaginary part of the refractive index is almost as large as the real part. This is a key limitation for many potential applications since light is largely absorbed within a few wavelengths of propagation inside the material.

In this chapter, we focus on atomic systems that are driven with lasers in their internal states so that negative refraction for a weak probe wave is achieved. The key advantages of using driven atomic systems as opposed to metamaterials are: (i) using interference principles, one can obtain a negative index of refraction with negligible absorption, (ii) atomic systems are uniquely suited for achieving negative refraction at shorter and shorter wavelengths, particularly in the visible and ultraviolet regions of the spectrum, (iii) since negative refraction is achieved through manipulation of internal states, the properties of the material can be dynamically modified, (iv) unlike metamaterials, which have anisotropic negative refraction due to orientation of the resonator structures, negative refraction by an atomic vapor is naturally isotropic.

Despite these advantages, achieving negative refraction in atomic systems is a very challenging problem that has not yet been experimentally demonstrated due to several difficulties. According to Veselago, achieving negative refraction for light of a particular frequency requires that both ϵ and μ have negative values at that frequency. Revisiting the resonant interaction of light with atoms discussed in Chap. 2, we consider an idealized atomic system to achieve negative refraction in Fig. 4.1. In this atom a probe beam interacts with a three-level system where there is a ground state, $|g\rangle$, and two excited states, $|e\rangle$ and $|m\rangle$. There exists an electric dipole matrix element d_{ge} corresponding to a resonant electric dipole transition between states $|g\rangle$ and $|e\rangle$ by the electric field of the probe beam and similarly a magnetic dipole matrix element μ_{gm} for the transition between states $|g\rangle$ and $|m\rangle$ for the magnetic field of the probe. In this system the states $|e\rangle$ and $|m\rangle$ are degenerate such that the same probe beam may be concurrently resonant with both states and the electric and magnetic transitions overlap at the same resonant frequency. Thus for a probe beam tuned near this resonance frequency, the electric and magnetic fields of the probe beam simultaneously interact with the atom to significantly alter the values of the permittivity and permeability. The degeneracy of the levels is ideal because in order to satisfy Veselago's condition for negative refraction, there must be an overlap of the frequency bands where ϵ and μ are both negative. All

recent proposals include this constraint that requires a strong electric dipole and a strong magnetic dipole transition at almost exactly the same wavelength, which is difficult to satisfy in real atomic systems.

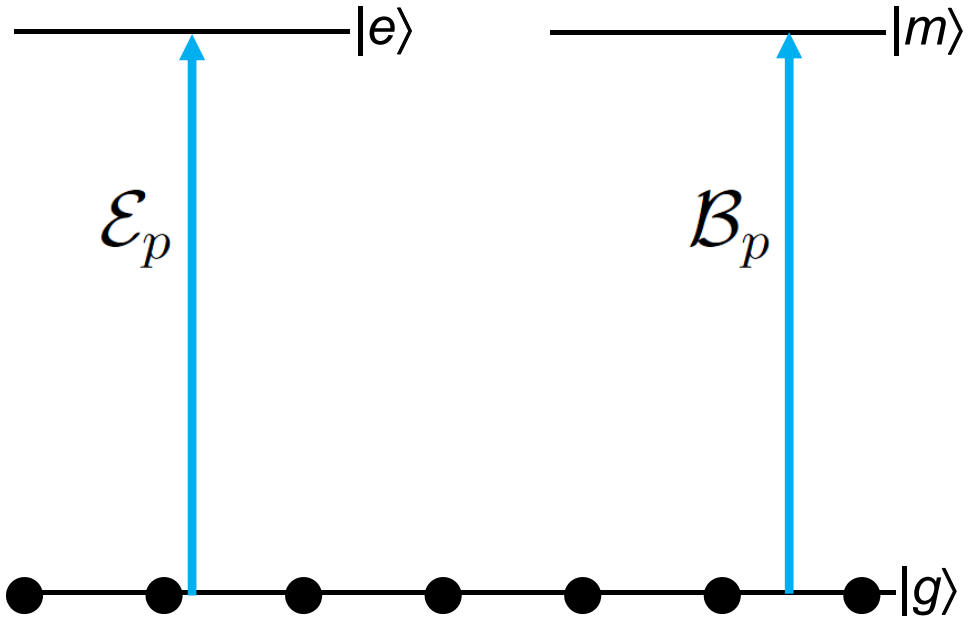

Figure 4.1 An idealized scheme to achieve negative refractive index in an atomic system. In this three level system there are strong electric dipole and magnetic dipole transitions at exactly the same wavelength, between the ground state $|g\rangle$ and the excited states $|e\rangle$ and $|m\rangle$, respectively. The light of a probe beam simultaneously interacts with the system in the electric and magnetic resonances, via the fields $\mathcal{E}_P$ and $\mathcal{B}_P$. Thus for sufficiently strong interactions, both ϵ and μ of the system will be negative at the probe frequency, resulting in negative refractive index.

Another challenging difficulty is the magnetic interaction in the atom is much weaker than the electric interaction. Fundamentally the electric response is stronger because how the different fields interact with matter. The interactions differ in that the electric field is able to directly influence the motion of electric charges in matter, whereas there are no known magnetic charges that the magnetic field interacts with. The electric dipole of an atom comes from the separation of the oppositely charged electrons and nuclei. The magnetic dipoles of an atom originate from the motion of electric charges that are present in the angular momentum of orbital electrons and intrinsic spin of electrons and nuclei. Hence, typical electric dipole moments are characterized

by the electron charge and the Bohr radius, $d \sim ea_0$, and the magnetic dipole moments are characterized by the Bohr magneton, $\mu \sim \mu_B = \frac{e\hbar}{2m_e c} = \frac{1}{2}\alpha e a_0$ [22], where $\alpha \approx 1/137$ is the fine structure constant. The fact that magnetic dipole moments are typically two orders of magnitude smaller than electric dipole moments is related to the weak magnetic response observed in most materials. Furthermore, achieving negative permittivity and permeability simultaneously requires atomic densities greater than 10^{18} cm^{-3}, which is impractical.

4.2 Previous atomic system approaches

As mentioned above, Veselago's original proposal for achieving a negative index of refraction requires $\epsilon < 0$ and $\mu < 0$ simultaneously. Using this idea, Oktel and Müstecaplioğlu [98] were the first to study the possibility of negative refraction in driven atomic systems. They proposed a model three-level system that induces a magnetic resonance between two levels with a non-zero magnetic dipole matrix element by using laser driven quantum coherent techniques to establish a coherence between the levels. Simultaneously the probe beam acts in an on resonant electric dipole transition as part of the process forming the magnetic resonance coherence. A similar technique for negative refraction in atomic vapors was independently proposed by Shen shortly after [132]. The ideas of Oktel and Müstecaplioğlu were built upon by Thommen and Mandel [145] in a proposed four-level system that does not require a common ground state for the electric and magnetic transitions.

As mentioned above, in the optical region of the spectrum the chief difficulty of this approach is the weakness of the magnetic response. Since typical magnetic dipole moments are weaker than electric dipole moments, achieving negative permeability requires impractically large atomic densities. To alleviate this problem, a chiral route to negative refraction has recently been suggested [105, 92]. Here, the key idea is to use a magnetoelectric cross coupling where the medium's electric polarization is coupled to the magnetic field of the wave, and the medium's magnetization is coupled to the electric field. As we will discuss below, under such conditions, negative refraction can be achieved without requiring a negative permeability. Building on this idea, Walsworth and colleagues have recently suggested a promising scheme that achieves negative refraction with

low absorption using quantum interference [62, 63]. Their scheme utilizes the dark state of Electromagnetically Induced Transparency (EIT) to reduce absorption while enhancing the chiral response. This scheme appears to be the most promising of the previously suggested approaches and achieves negative refraction with low absorptive loss at a density of about 5×10^{16} cm^{-3}.

All of the recent suggestions mentioned above require a strong magnetic dipole and a strong electric dipole transition at almost exactly the same wavelength. This requirement puts a stringent constraint on the energy level structure of systems in which negative refraction can be achieved. The approach [134] we consider overcomes this constraint and furthermore achieves negative refraction with more conservative atomic system parameters (including atomic density and linewidth) compared to previous suggestions. We achieve these benefits at the expense of requiring two intense control lasers. Together with the probe laser, these control lasers induce two Raman transitions: one absorptive and one amplifying in nature. The interference of these two transitions results in a strong enhancement of the permittivity while minimizing absorption. We then coherently couple to a magnetic dipole transition to obtain a chiral response and to achieve a negative index of refraction through magnetoelectric cross coupling.

Before proceeding with a detailed description of our suggestion, we summarize the chiral approach to negative refraction. Consider a probe beam with electric field and magnetic field components $\mathcal{E}_p$ and $\mathcal{B}_p$, respectively. In a material with magnetoelectric cross coupling, the medium polarization, P_p, and the magnetization, M_p are given by [62, 63]:

$$\begin{aligned} P_p &= \epsilon_0 \chi_{\mathcal{E}} \mathcal{E}_p + \frac{\xi_{\mathcal{EB}}}{c\mu_0} \mathcal{B}_p \quad , \\ M_p &= \frac{\xi_{\mathcal{BE}}}{c\mu_0} \mathcal{E}_p + \frac{\chi_{\mathcal{B}}}{\mu_0} \mathcal{B}_p \quad , \end{aligned} \tag{4.1}$$

where $\chi_{\mathcal{E}}$, $\chi_{\mathcal{B}}$ are the electric and magnetic susceptibilities, and $\xi_{\mathcal{EB}}$, $\xi_{\mathcal{BE}}$ are the complex magnetoelectric coupling (chirality) coefficients, respectively. The index of refraction of the medium for a plane wave of a particular circular polarization can be found by using Eqs. (4.1) and Maxwell's equations (see Appendix B for details):

$$n = \sqrt{\epsilon\mu - \frac{(\xi_{\mathcal{EB}} + \xi_{\mathcal{BE}})^2}{4}} + \frac{i}{2}(\xi_{\mathcal{EB}} - \xi_{\mathcal{BE}}) \quad . \tag{4.2}$$

Here, $\epsilon = 1 + \chi_{\mathcal{E}}$ and $\mu = 1 + \chi_{\mathcal{B}}$ are the relative permittivity and permeability of the medium. As shown in Eq. (4.2), the chirality coefficients result in additional contributions to the index of refraction. The key idea behind the chiral approach is that, in the optical region, one typically has the scaling $\chi_{\mathcal{B}} \sim \alpha^2\chi_{\mathcal{E}}$ and $(\xi_{\mathcal{EB}}, \xi_{\mathcal{BE}}) \sim \alpha\chi_{\mathcal{E}}$. Since the value of the chirality coefficients are smaller only by a factor of α instead of α^2, negative refraction can be achieved without the need for negative permeability and at much smaller atomic densities compared to non-chiral schemes. Negative refraction with chirality requires appropriate phase control of the chirality coefficients which can be achieved through coherent magnetoelectric coupling. One typically chooses the phase such that the chirality coefficients are imaginary, $\xi_{\mathcal{EB}} = -\xi_{\mathcal{BE}} = i\xi$, and Eq. (4.2) reads $n = \sqrt{\epsilon\mu} - \xi$. Achieving $n < 0$ then requires a sufficiently large chiral response such that $\xi > \sqrt{\epsilon\mu}$. Furthermore, to reduce absorption, it is critical to keep the imaginary part of the refractive index to be as low as possible. The performance of negative index materials is typically characterized by the figure of merit, FoM=-Re(n)/|Im(n)|.

4.3 Negative refraction using Raman transitions with cross coupling

We proceed with a detailed description of our suggestion. Noting Fig. 4.2, we consider a six-level system interacting with four laser beams. We wish to achieve a negative index of refraction for the probe laser beam with field components $\mathcal{E}_p$ and $\mathcal{B}_p$, respectively. We take the atomic system to have a strong magnetic transition with dipole moment μ_{gm} near the frequency of the probe laser beam. As mentioned above, the system does not have a strong electric dipole transition near the probe laser frequency. The electric dipole response is obtained by using two-photon Raman transitions through the excited states $|a\rangle$ and $|b\rangle$. At the heart of the scheme is the "refractive index enhancement with vanishing absorption" technique [165, 4, 113, 166], described in Chap. 2. Starting with the ground state $|g\rangle$, we induce two Raman transitions using the probe laser and two intense control lasers with electric field amplitudes $\mathcal{E}_{\mathcal{C}1}$ and $\mathcal{E}_{\mathcal{C}2}$. Since the order at which the probe laser beam is involved in each Raman transition is different, this scheme achieves two resonances: one amplifying and one absorptive in nature. The strength and position of these two resonances can be controlled by varying the intensities and frequencies of the control laser beams. It is the

interference of these two resonances that results in the control of the index of refraction while maintaining small absorption. The magnetoelectric cross coupling is achieved through coherent coupling of states $|2\rangle$ and $|m\rangle$ with a separate laser beam of Rabi frequency Ω_{2m}. States $|g\rangle$, $|1\rangle$, $|2\rangle$ and $|m\rangle$ have the same parity, which is opposite to the parity of states $|a\rangle$ and $|b\rangle$. Since states $|2\rangle$ and $|m\rangle$ have the same parity, the coherent coupling Ω_{2m} cannot be electric dipole, but instead can be achieved through the magnetic field of a strong laser or through a separate two-photon transition (not shown). The two-photon detunings from the two Raman transitions are defined as: $\delta\omega_1 = (\omega_1 - \omega_g) - (\omega_{\mathcal{C}1} - \omega_p)$ and $\delta\omega_2 = (\omega_2 - \omega_g) - (\omega_p - \omega_{\mathcal{C}2})$. The quantity $\delta\omega_{\mathcal{B}} = (\omega_m - \omega_g) - \omega_p$ is the detuning of the probe laser beam from the $|g\rangle \rightarrow |m\rangle$ magnetic transition.

Without loss of generality, we have chosen the probe fields $\mathcal{E}_p$ and $\mathcal{B}_p$ to have σ_+ polarization while the coupling fields Ω_{2m}, $\mathcal{E}_{\mathcal{C}1}$, and $\mathcal{E}_{\mathcal{C}2}$ have σ_- polarization. These circular polarized fields interact within the Zeeman sublevel structure of the atom. For a system where the particular fields are oppositely circular polarized, we would expect the terms in Eq. (4.2) to interfere differently, which could lead to an enhanced positive index of refraction. For a linear polarization of the fields we would expect the medium to exhibit unusually high optical rotation of the probe beam.

We start by expanding the total wave function for the atomic system, $|\psi\rangle$, in the interaction picture:

$$\begin{aligned} |\psi\rangle &= c_g \exp(-i\omega_g t)|g\rangle + c_1 \exp(-i\omega_1 t)|1\rangle + c_2 \exp(-i\omega_2 t)|2\rangle \\ &+ c_m \exp(-i\omega_m t)|m\rangle + c_a \exp(-i\omega_a t)|a\rangle + c_b \exp(-i\omega_b t)|b\rangle \quad , \end{aligned} \tag{4.3}$$

where the quantities c_i are the complex probability amplitudes of the respective levels. The total Hamiltonian of the system can be written as $\hat{H}_{total} = \hat{H}_0 + \hat{H}_{int}$ where $\hat{H}_0$ is the unperturbed Hamiltonian and $\hat{H}_{int}$ is the interaction Hamiltonian that includes the interactions of the atom with the electric field and magnetic field components of the incident waves:

$$\begin{aligned} \hat{H}_0 &= \hbar\omega_g|g\rangle\langle g| + \hbar\omega_1|1\rangle\langle 1| + \hbar\omega_2|2\rangle\langle 2| + \hbar\omega_m|m\rangle\langle m| + \hbar\omega_a|a\rangle\langle a| + \hbar\omega_b|b\rangle\langle b| \quad , \\ \hat{H}_{int} &= -d_{ga}\mathcal{E}|g\rangle\langle a| - d_{gb}\mathcal{E}|g\rangle\langle b| - d_{1a}\mathcal{E}|1\rangle\langle a| - d_{2b}\mathcal{E}|2\rangle\langle b| \\ &- \mu_{gm}\mathcal{B}|g\rangle\langle m| - \mu_{2m}\mathcal{B}|2\rangle\langle m| + h.c. \quad . \end{aligned} \tag{4.4}$$

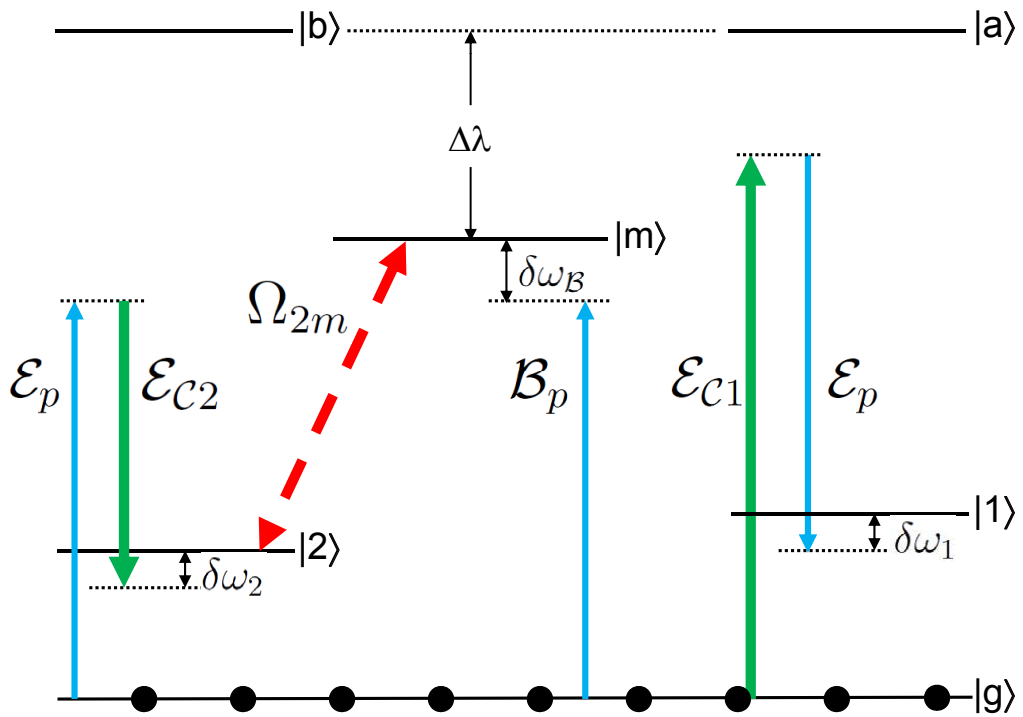

Figure 4.2 Schematic of the proposed scheme. $\mathcal{E}_p$ and $\mathcal{B}_p$ are the electric field and magnetic field components of a weak far-off resonant probe beam (blue). $|g\rangle \rightarrow |m\rangle$ is a magnetic dipole transition induced by the probe magnetic field $\mathcal{B}_p$. Two strong control lasers (green), $\mathcal{E}_{\mathcal{C}1}$ and $\mathcal{E}_{\mathcal{C}2}$, induce two electric dipole Raman transitions for the probe beam. The Raman transitions can be far-detuned from the excited states $|a\rangle$ and $|b\rangle$. Therefore, the system does not require the magnetic ($|g\rangle \rightarrow |m\rangle$) and electric ($|g\rangle \rightarrow |a\rangle$ and $|g\rangle \rightarrow |b\rangle$) transitions to be near the same frequency. Ω_{2m} (red dashed) induces magnetoelectric cross coupling (chirality).

Here, the quantities d_{ij} and μ_{ij} are the electric dipole and magnetic dipole transition matrix elements between respective levels, $\mathcal{E}$ and $\mathcal{B}$ are the total electric and magnetic fields, and $h.c.$ refers to Hermitian conjugate. The electric and magnetic fields include contributions from all relevant laser beams and they are:

$$\begin{aligned} \mathcal{E} &= Re\left\{\mathcal{E}_p \exp(-i\omega_p t) + \mathcal{E}_{\mathcal{C}1} \exp(-i\omega_{\mathcal{C}1} t) + \mathcal{E}_{\mathcal{C}2} \exp(-i\omega_{\mathcal{C}2} t)\right\} \quad , \\ \mathcal{B} &= Re\left\{\mathcal{B}_p \exp(-i\omega_p t) + \mathcal{B}_{2m} \exp(-i\omega_{2m} t)\right\} \quad . \end{aligned} \tag{4.5}$$

In the above, for concreteness, we have taken the magnetoelectric cross coupling to be induced by a third intense laser beam with magnetic field $\mathcal{B}_{2m}$. Using Eqs. (4.3) and (4.4) and ignoring the

dissipative processes for the moment, we write the Schrödinger's equation for the time evolution of the probability amplitudes:

$$\begin{aligned}
\dot{c}_g &= \frac{i}{\hbar}\left[d_{ga}\mathcal{E}c_a\exp(i(\omega_g-\omega_a)t)+d_{gb}\mathcal{E}c_b\exp(i(\omega_g-\omega_b)t)+\mu_{gm}\mathcal{B}c_m\exp(i(\omega_g-\omega_m)t)\right] \quad , \\
\dot{c}_1 &= \frac{i}{\hbar}\left[d_{1a}\mathcal{E}c_a\exp(i(\omega_1-\omega_a)t)\right] \quad , \\
\dot{c}_2 &= \frac{i}{\hbar}\left[d_{2b}\mathcal{E}c_b\exp(i(\omega_2-\omega_b)t)+\mu_{2m}\mathcal{B}c_m\exp(i(\omega_2-\omega_m)t)\right] \quad , \\
\dot{c}_m &= \frac{i}{\hbar}\left[\mu^*_{gm}\mathcal{B}c_g\exp(i(\omega_m-\omega_g)t)+\mu^*_{2m}\mathcal{B}c_2\exp(i(\omega_m-\omega_2)t)\right] \quad , \\
\dot{c}_a &= \frac{i}{\hbar}\left[d^*_{1a}\mathcal{E}c_1\exp(i(\omega_a-\omega_1)t)+d^*_{ga}\mathcal{E}c_g\exp(i(\omega_a-\omega_g)t)\right] \quad , \\
\dot{c}_b &= \frac{i}{\hbar}\left[d^*_{2b}\mathcal{E}c_2\exp(i(\omega_b-\omega_2)t)+d^*_{gb}\mathcal{E}c_g\exp(i(\omega_b-\omega_g)t)\right] \quad . \qquad [4.6]
\end{aligned}$$

We will focus on the case where the single-photon detunings from the excited electronic states are much larger than the coupling rates. This allows adiabatic elimination of the probability amplitudes of the excited electronic levels $|a\rangle$ and $|b\rangle$. This is an important simplification for the analytical results since it reduces the problem to an effective four-level system. We note, however, that we do not make this simplification in the numerical results of the next section and solve the density-matrix for the full six levels. As we will discuss, the numerical results for the full system are in reasonable agreement with the analytical solutions. We take all the relevant detunings to be small compared to the absolute laser frequencies and make the rotating wave approximation. Integrating out the differential equations for c_a and c_b we obtain:

$$\begin{aligned}
c_a &= \frac{d^*_{1a}}{2\hbar}c_1\sum_{q=p,\mathcal{C}1,\mathcal{C}2}\frac{\mathcal{E}_q\exp(i(\omega_a-\omega_1-\omega_q)t)}{\omega_a-\omega_1-\omega_q}+\frac{d^*_{ga}}{2\hbar}c_g\sum_{q=p,\mathcal{C}1,\mathcal{C}2}\frac{\mathcal{E}_q\exp(i(\omega_a-\omega_g-\omega_q)t)}{\omega_a-\omega_g-\omega_q} \quad , \\
c_b &= \frac{d^*_{2b}}{2\hbar}c_2\sum_{q=p,\mathcal{C}1,\mathcal{C}2}\frac{\mathcal{E}_q\exp(i(\omega_b-\omega_2-\omega_q)t)}{\omega_b-\omega_2-\omega_q}+\frac{d^*_{gb}}{2\hbar}c_g\sum_{q=p,\mathcal{C}1,\mathcal{C}2}\frac{\mathcal{E}_q\exp(i(\omega_b-\omega_g-\omega_q)t)}{\omega_b-\omega_g-\omega_q} \qquad [4.7]
\end{aligned}$$

By using the algebraic expressions for the probability amplitudes of Eq. (4.7) and after transforming to a rotating frame (details in Appendix A), the Schrödinger's equation for the simplified four level system is:

$$\dot{c_g} \quad + \quad \frac{Im(A)}{2}c_g = i\frac{B_1}{2}c_1 + i\frac{B_2}{2}c_2 + i\frac{\Omega_{gm}}{2}c_m \quad ,$$

$$
\begin{aligned}
\dot{c_1} &+ i\left[\delta\omega_1 - \frac{Re(F_1 - A)}{2}\right] c_1 + \left[\gamma_1 + \frac{Im(F_1)}{2}\right] c_1 = i\frac{B_1^*}{2} c_g \quad , \\
\dot{c_2} &+ i\left[\delta\omega_2 - \frac{Re(F_2 - A)}{2}\right] c_2 + \left[\gamma_2 + \frac{Im(F_2)}{2}\right] c_2 = i\frac{B_2^*}{2} c_g + i\frac{\Omega_{2m}}{2} c_m \quad , \\
\dot{c_m} &+ i\left[\delta\omega_{\mathcal{B}} + \frac{Re(A)}{2}\right] c_m + \gamma_m c_m = i\frac{\Omega_{gm}^*}{2} c_g + i\frac{\Omega_{2m}^*}{2} c_2 \quad . \qquad [4.8]
\end{aligned}
$$

Here, we have added the decay rates of the levels, γ_1, γ_2, and γ_m, phenomenologically. At this stage of the formalism, since we are not using the density matrix, the decay processes are assumed to be to states outside the system. $\Omega_{gm} = \mu_{gm}\mathcal{B}_p^*/\hbar$ is the Rabi frequency due to magnetic field of the probe laser beam that couples states $|g\rangle$ and $|m\rangle$. $\Omega_{2m} = \mu_{2m}\mathcal{B}_{2m}^*/\hbar$ is the magnetoelectric cross coupling rate. The quantities that appear in Eq. (4.8), within the rotating wave approximation, are given by

$$
\begin{aligned}
A &= \mathrm{a}_p \left|\mathcal{E}_p\right|^2 + \mathrm{a}_{\mathcal{C}1} \left|\mathcal{E}_{\mathcal{C}1}\right|^2 \quad , \quad B_1 = b_1 \mathcal{E}_p \mathcal{E}_{\mathcal{C}1}^* \quad , \quad B_2 = b_2 \mathcal{E}_p^* \mathcal{E}_{\mathcal{C}2} \quad , \\
F_1 &= f_{1,p} \left|\mathcal{E}_p\right|^2 \quad , \quad F_2 = f_{2,\mathcal{C}2} \left|\mathcal{E}_{\mathcal{C}2}\right|^2 \quad , \\
\mathrm{a}_p &= \frac{1}{2\hbar^2}\left[\frac{\left|d_{gb}\right|^2}{\omega_b - \omega_g - \omega_p - i\Gamma_b}\right] \quad , \\
\mathrm{a}_{\mathcal{C}1} &= \frac{1}{2\hbar^2}\left[\frac{\left|d_{ga}\right|^2}{\omega_a - \omega_g - \omega_{\mathcal{C}1} - i\Gamma_a}\right] \quad , \\
b_1 &= \frac{1}{2\hbar^2}\left[\frac{d_{ga} d_{1a}^*}{\omega_a - \omega_g - \omega_{\mathcal{C}1} - i\Gamma_a}\right] \quad , \\
b_2 &= \frac{1}{2\hbar^2}\left[\frac{d_{gb} d_{2b}^*}{\omega_b - \omega_g - \omega_p - i\Gamma_b}\right] \quad , \\
f_{1,p} &= \frac{1}{2\hbar^2}\left[\frac{\left|d_{1a}\right|^2}{\omega_a - \omega_1 - \omega_p - i\Gamma_a}\right] \quad , \\
f_{2,\mathcal{C}2} &= \frac{1}{2\hbar^2}\left[\frac{\left|d_{2b}\right|^2}{\omega_b - \omega_2 - \omega_{\mathcal{C}2} - i\Gamma_b}\right] \quad . \qquad [4.9]
\end{aligned}
$$

Here, the quantities Γ_a and Γ_b are the decay rates of the excited levels $|a\rangle$ and $|b\rangle$, respectively.

4.4 Analytical steady-state solutions

We proceed with a perturbative, steady-state analytical solution for the system. For this purpose, we take the laser intensities to be sufficiently weak such that most of the population stays in the

ground atomic state, $c_g \approx 1$. For time-scales long when compared with the inverse of the decay rates, the steady-state solutions for the probability amplitudes of the relevant levels are:

$$
\begin{aligned}
c_1 &\approx \frac{B_1^*}{2\left[\delta\omega_1 - \frac{Re(F_1-A)}{2} - i\left(\gamma_1 + \frac{Im(F_1)}{2}\right)\right]} \quad , \\
c_2 &\approx \frac{2B_2^*\left[\delta\omega_{\mathcal{B}} + \frac{Re(A)}{2} - i\gamma_m\right] + \Omega_{2m}\Omega_{gm}^*}{4\left[\delta\omega_2 - \frac{Re(F_2-A) - i\left(\gamma_2 + \frac{Im(F_2)}{2}\right)}{2}\right]\left[\delta\omega_{\mathcal{B}} + \frac{Re(A)}{2} - i\gamma_m\right] - |\Omega_{2m}|^2} \quad , \\
c_m &\approx \frac{\Omega_{gm}^*}{2\left[\delta\omega_{\mathcal{B}} + \frac{Re(A)}{2} - i\gamma_m\right]} \\
&+ \frac{B_2^*\Omega_{2m}^*}{4\left[\delta\omega_{\mathcal{B}} + \frac{Re(A)}{2} - i\gamma_m\right]\left[\delta\omega_2 - \frac{Re(F_2-A)}{2} - \frac{|\Omega_{2m}|^2}{4\left(\delta\omega_{\mathcal{B}} + \frac{Re(A)}{2} - i\gamma_m\right)} - i\left(\gamma_2 + \frac{Im(F_2)}{2}\right)\right]} \\
&+ \frac{|\Omega_{2m}|^2\,\Omega_{gm}^*}{8\left[\delta\omega_{\mathcal{B}} + \frac{Re(A)}{2} - i\gamma_m\right]^2\left[\delta\omega_2 - \frac{Re(F_2-A)}{2} - \frac{|\Omega_{2m}|^2}{4\left(\delta\omega_{\mathcal{B}} + \frac{Re(A)}{2} - i\gamma_m\right)} - i\left(\gamma_2 + \frac{Im(F_2)}{2}\right)\right]}
\end{aligned}
\qquad [4.10]
$$

As we will discuss in the next section, we verify the validity of this steady-state solution by using full numerical simulations of the density matrix. With the analytical solutions for the probability amplitudes, we form coherences and calculate the medium's response at the probe laser frequency. The polarization and the magnetization of the medium are:

$$
\begin{aligned}
P_p &= 2\hbar N\left(\mathrm{a}_p\,|c_g|^2\,\mathcal{E}_p + b_1^* c_g c_1^* \mathcal{E}_{\mathcal{C}1} + b_2 c_g^* c_2 \mathcal{E}_{\mathcal{C}2}\right) \equiv N\left(\alpha_{\mathcal{E}\mathcal{E}}\mathcal{E}_p + \alpha_{\mathcal{E}\mathcal{B}}\mathcal{B}_p\right) \quad , \\
M_p &= 2N c_g^* c_m \mu_{gm} \equiv N\left(\alpha_{\mathcal{B}\mathcal{E}}\mathcal{E}_p + \alpha_{\mathcal{B}\mathcal{B}}\mathcal{B}_p\right) \quad ,
\end{aligned}
\qquad [4.11]
$$

where N is the number of atoms per unit volume. In the expressions above, the quantities $\alpha_{\mathcal{E}\mathcal{E}}$, $\alpha_{\mathcal{B}\mathcal{B}}$, $\alpha_{\mathcal{E}\mathcal{B}}$, and $\alpha_{\mathcal{B}\mathcal{E}}$ are the electric, magnetic, and cross coupling polarizabilities and they are given by:

$$
\begin{aligned}
\alpha_{\mathcal{E}\mathcal{E}} &= 2\hbar\mathrm{a}_p + \frac{\hbar\,|b_1|^2\,|\mathcal{E}_{\mathcal{C}1}|^2}{\left[\delta\tilde{\omega}_1 + i\left(\gamma_1 + \frac{Im(F_1)}{2}\right)\right]} + \frac{\hbar\,|b_2|^2\,|\mathcal{E}_{\mathcal{C}2}|^2}{\left[\delta\tilde{\omega}_2 - \frac{|\Omega_{2m}|^2}{4\left(\delta\tilde{\omega}_{\mathcal{B}} - i\gamma_m\right)} - i\left(\gamma_2 + \frac{Im(F_2)}{2}\right)\right]} \quad , \\
\alpha_{\mathcal{B}\mathcal{B}} &= \frac{|\mu_{gm}|^2}{\hbar\left[\left(\delta\tilde{\omega}_{\mathcal{B}} - i\gamma_m\right) - \frac{|\Omega_{2m}|^2}{4\left(\delta\tilde{\omega}_2 - i\left(\gamma_2 + \frac{Im(F_2)}{2}\right)\right)}\right]} \quad ,
\end{aligned}
$$

$$\alpha_{\mathcal{EB}} = \frac{b_2\mu^*_{gm}\mathcal{E}_{\mathcal{C}2}\Omega_{2m}}{2\left(\delta\tilde{\omega}_{\mathcal{B}}+-i\gamma_m\right)\left[\delta\tilde{\omega}_2-\frac{|\Omega_{2m}|^2}{4\left(\delta\tilde{\omega}_{\mathcal{B}}-i\gamma_m\right)}-i\left(\gamma_2+\frac{Im(F_2)}{2}\right)\right]} \quad ,$$

$$\alpha_{\mathcal{BE}} = \frac{b^*_2\mu_{gm}\mathcal{E}^*_{\mathcal{C}2}\Omega^*_{2m}}{2\left(\delta\tilde{\omega}_{\mathcal{B}}-i\gamma_m\right)\left[\delta\tilde{\omega}_2-\frac{|\Omega_{2m}|^2}{4\left(\delta\tilde{\omega}_{\mathcal{B}}-i\gamma_m\right)}-i\left(\gamma_2+\frac{Im(F_2)}{2}\right)\right]} \quad , \qquad [4.12]$$

where we have introduced a simplified notation for the detunings that includes the AC Stark shifts,

$$\begin{aligned}
\delta\tilde{\omega}_{\mathcal{B}} &= \delta\omega_B+\frac{Re(A)}{2} \quad , \\
\delta\tilde{\omega}_1 &= \delta\omega_1-\frac{Re(F_1-A)}{2} \quad , \\
\delta\tilde{\omega}_2 &= \delta\omega_2-\frac{Re(F_2-A)}{2} \quad . \qquad [4.13]
\end{aligned}$$

It is well-known that when the refractive index is strongly modified, the microscopic local fields can be substantially different than the averaged macroscopic fields. To calculate the susceptibilities, chirality coefficients, and the refractive index, we include both electric and magnetic Clausius-Mossotti-type local field effects [21, 61]. For electric and magnetic fields, the relationships between microscopic local fields and macroscopic quantities are:

$$\begin{aligned}
\mathcal{E}_p^{micro} &= \mathcal{E}_p+\frac{1}{3\epsilon_0}P_p \quad , \\
\mathcal{B}_p^{micro} &= \mathcal{B}_p+\frac{\mu_0}{3}M_p \quad . \qquad [4.14]
\end{aligned}$$

Solving Eq. (4.11) together with the local field corrections of Eq. (4.14), we get the following expressions for the electric and magnetic susceptibilities and the chirality coefficients:

$$\begin{aligned}
\chi_{\mathcal{E}} &= N\frac{1}{\kappa\epsilon_0}\left[\alpha_{\mathcal{EE}}+N\frac{\mu_0}{3}\left(\alpha_{\mathcal{EB}}\alpha_{\mathcal{BE}}-\alpha_{\mathcal{EE}}\alpha_{\mathcal{BB}}\right)\right] \quad , \\
\chi_{\mathcal{B}} &= N\frac{\mu_0}{\kappa}\left[\alpha_{\mathcal{BB}}+N\frac{1}{3\epsilon_0}\left(\alpha_{\mathcal{EB}}\alpha_{\mathcal{BE}}-\alpha_{\mathcal{EE}}\alpha_{\mathcal{BB}}\right)\right] \quad , \\
\xi_{\mathcal{EB}} &= N\frac{\mu_0 c}{\kappa}\alpha_{\mathcal{EB}} \quad , \\
\xi_{\mathcal{BE}} &= N\frac{\mu_0 c}{\kappa}\alpha_{\mathcal{BE}} \quad , \qquad [4.15]
\end{aligned}$$

where the quantity κ largely determines the density-dependent local field enhancement and is:

$$\kappa = 1-N\frac{1}{3\epsilon_0}\alpha_{\mathcal{EE}}-N\frac{\mu_0}{3}\alpha_{\mathcal{BB}}-N^2\frac{\mu_0}{9\epsilon_0}\left[\alpha_{\mathcal{EB}}\alpha_{\mathcal{BE}}-\alpha_{\mathcal{EE}}\alpha_{\mathcal{BB}}\right] \quad . \qquad [4.16]$$

Eqs. (4.11-4.16) represent the final results of this section. Given a certain set of parameters for our system such as matrix elements, laser intensities, and the atomic density, we use these equations to calculate the susceptibilities and the chirality coefficients. It is important to note that these equations are valid in the perturbative limit which will break down for sufficiently intense control laser beams. With the susceptibilities and chirality coefficients known, we then use Eq. (4.2) to calculate the real and imaginary parts of the refractive index.

4.5 Results for a model atomic system

In this section we present results for a model atomic system. For this purpose, we consider a probe beam at a wavelength of $\lambda_p = 500$ nm. We assume the ideal case of pure radiative broadening for the excited electronic levels $|a\rangle$ and $b\rangle$ and take the radiative decay rates of these states to be $\Gamma_a = \Gamma_b = 2\pi \times 14.3$ MHz. The dipole matrix elements, d_{ia} and d_{ib} are calculated using the Wigner-Weisskopf result and assuming equal branching ratios, $d_{ia} = \sqrt{\pi\epsilon_0\Gamma_a\hbar c^3/\omega_p^3}$, $d_{ib} = \sqrt{\pi\epsilon_0\Gamma_b\hbar c^3/\omega_p^3}$. We apply a similar procedure and assume a radiative decay rate of $\alpha^2\Gamma_a$ for the magnetic level $|m\rangle$ and calculate the corresponding magnetic dipole matrix element, μ_{gm}. To simulate a realistic system, we assume an additional broadening mechanism (collisions for example) with a rate $\gamma_c = 2\pi \times 1$ MHz and add this broadening to the linewidths of states $|1\rangle$, $|2\rangle$, and $|m\rangle$. We take the wavelengths of electric dipole ($|g\rangle \rightarrow |a\rangle, |b\rangle$) and magnetic dipole ($|g\rangle \rightarrow |m\rangle$) transitions to be different by $\Delta\lambda = 0.1$ nm. As we will discuss below, this difference can be larger at the expense of an increase in the required control laser intensities. We take the magnetoelectric coupling laser beam to be resonant with the $|2\rangle \rightarrow |m\rangle$ transition and therefore take $\delta\tilde{\omega}_{\mathcal{B}} = \delta\tilde{\omega}_2$.

Figure 4.3 shows the susceptibilities and the chirality coefficients, $\chi_{\mathcal{E}}$, $\chi_{\mathcal{B}}$, $\xi_{\mathcal{EB}}$, and $\xi_{\mathcal{BE}}$, *without* the local-field corrections as the frequency of the probe laser beam is varied for an atomic density of $N = 5 \times 10^{16}$ cm^{-3}. Here, we assume that the control laser frequencies are appropriately adjusted such that the two Raman resonance frequencies coincide as the probe laser frequency is scanned, $\delta\tilde{\omega}_1 = -\delta\tilde{\omega}_2$. We take the intensities of the two control laser beams to be $I_{\mathcal{C}1} = 0.27$ MW/cm^2 and $I_{\mathcal{C}2} = 1.00$ MW/cm^2 and assume $\Omega_{2m} = i2\pi \times 1.36$ MHz. The intensities of the control

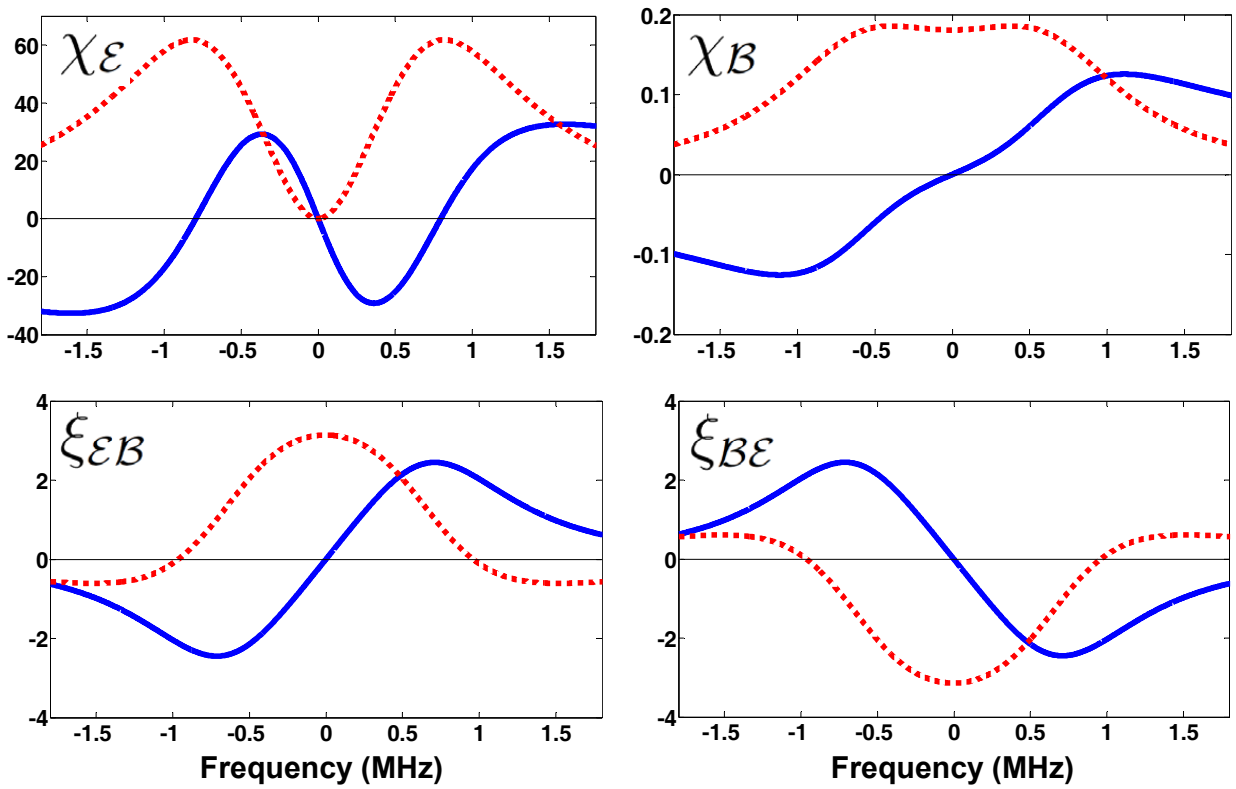

Figure 4.3 The real (solid blue line) and imaginary (dotted red line) parts of the susceptibilities and the chirality coefficients without the local-field corrections. See text for parameters. Since the electric dipole response is due to Raman transitions, its strength is controlled by the intensity of the control laser beams. As a result, compared to earlier suggested schemes, the magnitude of $\chi_{\mathcal{E}}$ is more comparable to the chirality coefficients in our approach.

lasers are adjusted to these values to have near cancellation of absorption. As shown in Fig. 4.3, the magnetoelectric coupling causes an EIT-like level splitting for $\chi_{\mathcal{E}}$. The imaginary part of $\chi_{\mathcal{E}}$ becomes small near $\delta\tilde{\omega}_{\mathcal{B}} = 0$ due to the interference of the two Raman resonances. One of the key differences of our approach compared to the scheme of Fleischhauer [62, 63] is that since the electric dipole response is due to Raman transitions, its strength is controlled by the intensity of the control laser beams. As a result, we do not have the usual scaling $\chi_{\mathcal{B}} \sim \alpha^2\chi_{\mathcal{E}}$ and $(\xi_{\mathcal{EB}}, \xi_{\mathcal{BE}}) \sim \alpha\chi_{\mathcal{E}}$, and the magnitude of $\chi_{\mathcal{E}}$ can be made more comparable to the chirality coefficients.

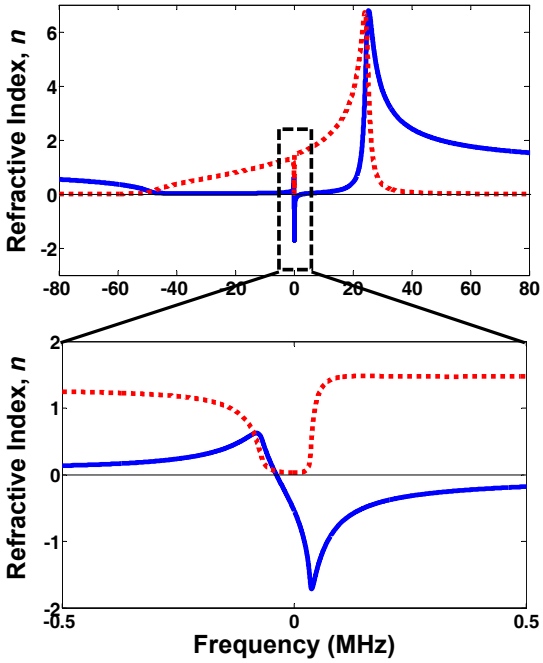

Figure 4.4 The real (solid blue) and imaginary (dotted red) parts of the index of refraction for an atomic density of $N = 5 \times 10^{16}$ cm^{-3}. The top plot shows a wide frequency scan of the resonant behavior and shows that far-off resonance the medium returns to $n = 1$. The bottom plot shows the detailed features that occur at the Raman and magnetic resonances. The index of refraction becomes negative and reaches a value of $n = -1$ with a figure of merit FoM> 20.

Noting Eqs. (4.15) and (4.16) there is a strong density dependent enhancement of both the electric and magnetic susceptibilities and the chirality coefficients. For sufficiently high densities, the local field effects cause an enhancement of a susceptibility resonance and a shift of its frequency position [61]. Figure 4.4 shows the real and imaginary parts of the refractive index as the probe frequency is scanned for the parameters of Fig. 4.3. In this figure we observe a very large off resonant peak which has a density dependent position arising from the local field effects. This large off resonant peak is a characteristic of the enhanced electric susceptibility, which overshadows the contributions of the other susceptibilities when seen in this broad frequency scan of the refractive index. At the densities of interest, the magnetic susceptibility and chirality coefficients are amplified but have negligible frequency shifts since the quantity κ is dominated by the electric

polarizability. The inset in Fig. 3 shows a zoomed in view of the refractive index at the original Raman and magnetic resonance frequency. The enhancement of the chirality terms in Eq.(4.2) within this region causes the refractive index of the medium to sharply decrease, becoming negative and this is accompanied by a flattening of the absorption approaching zero. For these parameters the refractive index reaches $n = -1$ with FoM> 20. It should be noted that in our technique it is necessary to have very low absorption in the electric susceptibility such that the local field effects can optimally enhance the negative refraction of the medium.

To show the critical dependence on atomic density, Fig. 4.5 shows the refractive index for $N = 2 \times 10^{16}$ cm^{-3} and $N = 1 \times 10^{17}$ cm^{-3} with parameters otherwise identical to those of Fig. 4.4. For $N = 1 \times 10^{17}$ cm^{-3}, we obtain an index of refraction of $n = -2.77$ with low absorption. For $n = -1$ the figure of merit is FoM≈ 40.

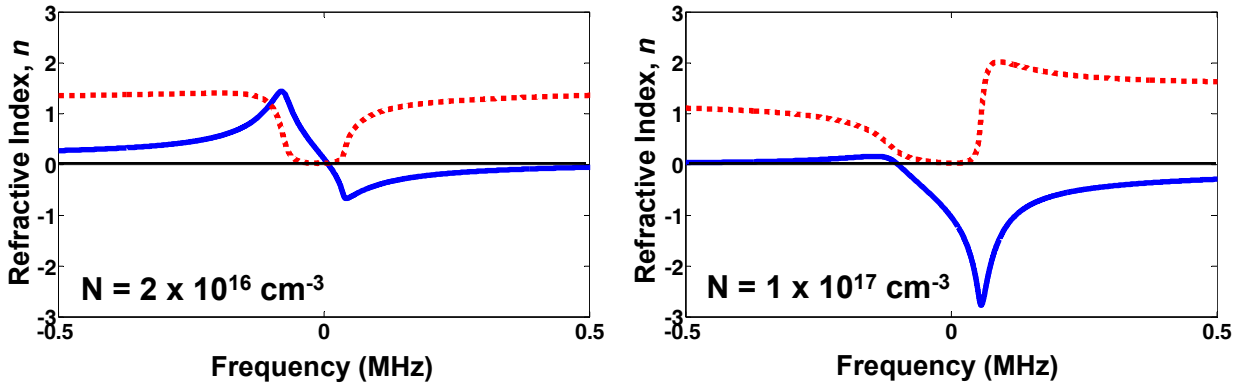

Figure 4.5 The real (solid blue) and imaginary (dotted red) parts of the index of refraction for an atomic density of $N = 2 \times 10^{16}$ cm^{-3} (left) and $N = 1 \times 10^{17}$ cm^{-3} (right). The other parameters are identical to those used in Fig. 4.4. For $N = 1 \times 10^{17}$ cm^{-3}, we obtain an index of refraction of $n = -1$ with a FoM ≈ 40.

Figure 4.6 shows the FoM achieved at the point Re$(n) = -1$ and the maximum FoM of the medium as the atomic density is varied with parameters otherwise identical to Figs. 4.3-4.5. For these parameters, the threshold density for a negative refractive index is $N = 6 \times 10^{15}$ cm^{-3}.

As mentioned above, for Figs. 4.3-4.6, the wavelengths for the electric dipole ($|g\rangle \rightarrow |a\rangle, |b\rangle$) and magnetic dipole ($|g\rangle \rightarrow |m\rangle$) transitions are assumed to be different by $\Delta\lambda = 0.1$ nm. This

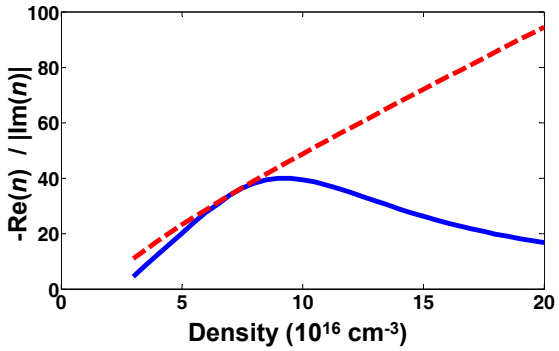

Figure 4.6 The figure of merit, FoM=-Re$(n)/|$Im$(n)|$ characterizes the performance of a negative index material. The solid blue line plots the FoM at the frequency position where Re$(n) = -1$ as the density of atoms is varied. The dashed red line plots the FoM at the frequency position where FoM is maximized. The maximum FoM increases with increasing atomic density, however at higher densities the maximum FoM occurs at frequencies where Re$(n) < -1$.

wavelength separation can be larger at the expense of an increase in the required control laser intensities. Figure 4.7 demonstrates this result. Here we plot the control laser intensity that is required to obtain results comparable to those of Figs. 4.3-4.6 as the wavelength separation between the transitions, $\Delta\lambda$, is varied. The transition wavelengths may be different by as much as $\Delta\lambda = 10$ nm and the scheme will still work with intensities that can be achieved with continuous-wave (CW) lasers (10 watt laser beam focused down to about one micron). This increases the flexibility on the energy level structure and, as we discuss in the next chapter, may allow experimental implementation in a real atomic system.

We next discuss the sensitivity of our technique to various system parameters. As mentioned before, in our technique, it is critical to have vanishing absorption by appropriately interfering the two Raman transitions. We have varied parameters of the first control laser, which takes part in the gain Raman transition, to simulate fluctuations that would lead to imperfect interference of the Raman resonances. The solid lines in Fig. 4.8 show the real and imaginary parts of the refractive index for parameters identical to those of Fig. 4.4 ($N = 5 \times 10^{16}$ cm^{-3}). For the dashed lines, the intensity of the first control laser is decreased by 1 % , whereas for the dotted lines it is decreased by 2 % of the optimized value ($I_{c1} = 0.27$ MW/cm^2). We still observe $n \approx -1$ with a reasonably

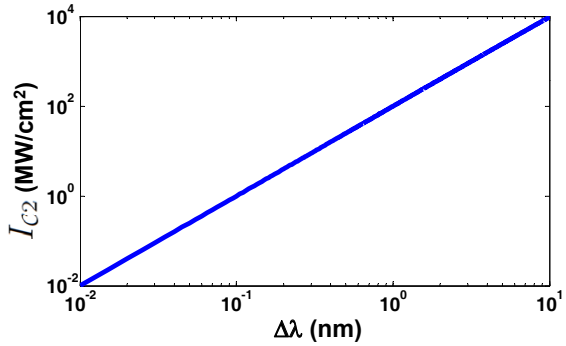

Figure 4.7 The control laser intensity, $I_{\mathcal{C}2}$, required to obtain results comparable to Figs. 4.3-4.6 as a function of the wavelength separation between the transitions, $\Delta\lambda$. The control laser intensity, $I_{\mathcal{C}1}$, follows a similar behavior (not shown).

good FoM. Similarly, to address frequency jitter sensitivity, the solid lines in Fig. 4.9 show the real and imaginary parts of the refractive index for parameters identical to those of Fig. 4.4. For the the dashed lines, the frequency of the first control laser is shifted off resonance by 0.25 MHz, whereas for the dotted lines it is shifted by -0.25 MHz. We observe qualitatively similar behavior of negative refraction with reduced absorption.

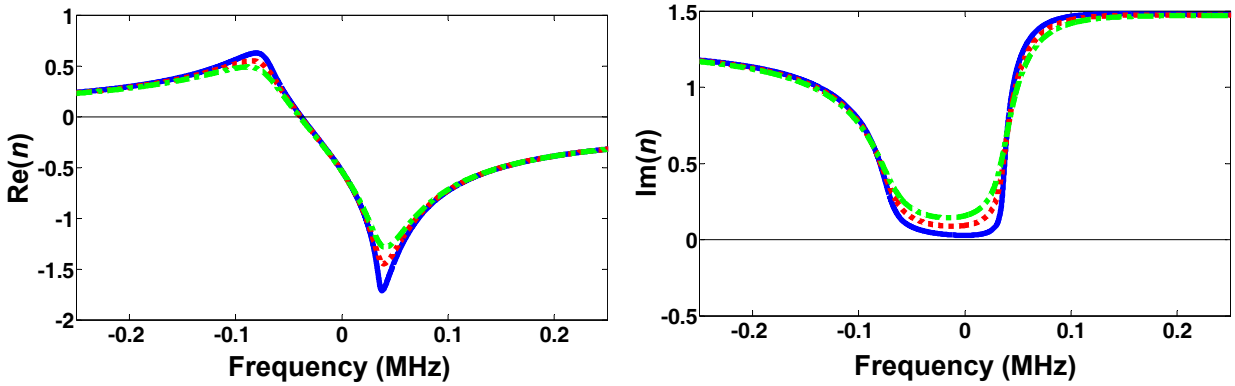

Figure 4.8 The real (left) and imaginary (right) parts of the index of refraction where the intensity of laser field $\mathcal{E}_{\mathcal{C}1}$ is at 100% (solid blue), 99 % (red dotted) and 98 % (green dash-dotted) of the optimized value of $I_{\mathcal{C}1} = 0.27$MW/cm^2 used in Figs. 4.3-4.5). The laser field $\mathcal{E}_{\mathcal{C}1}$ interacts in the gain Raman resonance, which leads to reduced absorption.

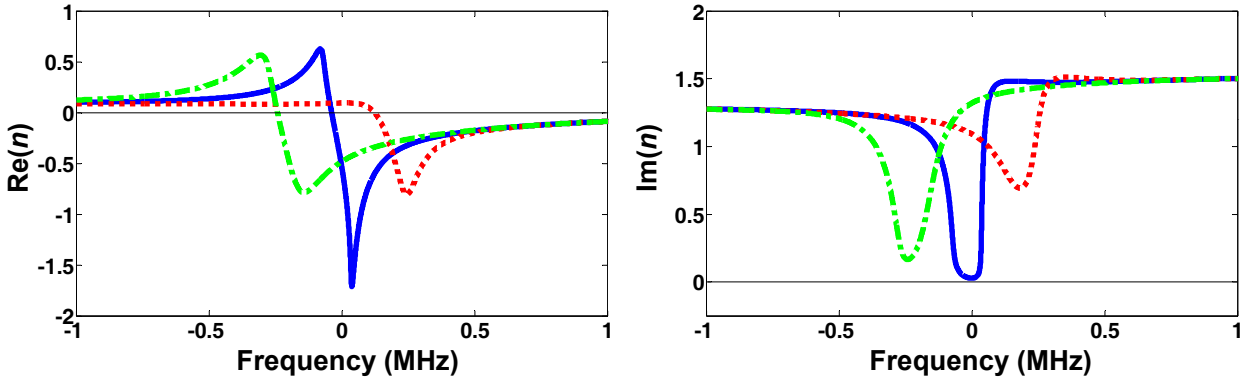

Figure 4.9 The real (left) and imaginary (right) parts of the index of refraction where the frequency of laser field $\mathcal{E}_{\mathcal{C}1}$ is tuned on resonance (solid blue) and off resonance by 0.25 MHz (red dotted) and by -0.25 MHz (green dash-dotted). As expected when the laser field is tuned off resonance the performance of the system as a negative index material decreases, but the features of negative refraction and reduced absorption remain qualitatively unchanged.

4.6 Numerical simulations

In this section, we present exact numerical simulations to verify the predictions of the analytical results. For this purpose, we use the density matrix formalism and numerically solve the evolution of the density matrix elements, $\rho_{ij} \equiv c_i c_j^*$, for the full six-level system. The equations that describe the evolution of the 6×6 density matrix are shown in Appendix C. For a given set of system parameters, we numerically integrate these equations with the initial condition that the atoms start in the ground state, $\rho_{gg} = 1$, and the laser fields are off and gradually turned on to full power in ≈ 400 ns. We use fourth-order Runge-Kutta as our numerical integration algorithm with a typical time grid spacing of ≈ 1 ps.

For the intensity values used in Figs. 4.3-4.6, using Eq. (4.13), the AC stark shifts calculated in our analytical formalism are on the order of 1 GHz, which is significantly higher than the linewidth of the resonances. Since the magnetic and two Raman resonances each experience a different AC Stark shift, we include adjustments to the tunings of the control lasers to ensure that all three resonances are aligned at the same frequency position. Initially we applied these analytical shift offsets in our numerical simulations, but we observed that frequency positions of the resonances

could be misaligned by as much as 30 MHz. This is because of the break down of the perturbative approximation and therefore the analytical estimates of the Stark shifts are underestimated. To compensate for this effect, we empirically applied additional shifts to the control laser frequencies such that all the resonances were aligned at the same frequency.

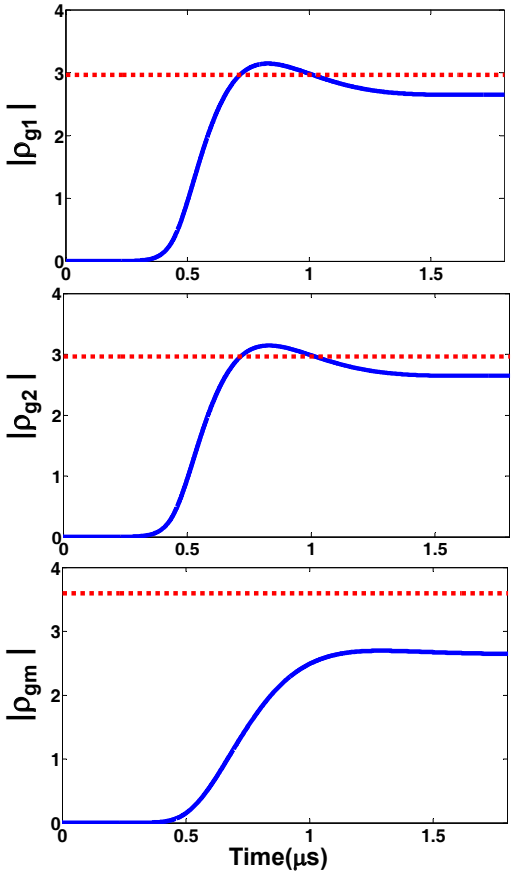

Figure 4.10 The numerically solved values (solid blue lines) of the coherences ρ_{g1}, ρ_{g2}, and ρ_{gm} (in arbitrary units) as they evolve in time with the intensity of the laser beams gradually applied. The coherences approach a steady state value in a little under 2 μs. The analytical formalism steady state solutions (red dotted lines) of the coherences are shown for comparison. The frequency of the probe beam is taken to be on the Raman and magnetic resonances.

Figure 4.10 shows the numerically calculated coherences, ρ_{g1}, ρ_{g2}, and ρ_{gm} for the parameters of Figs 4.3-4.6. For comparison, the coherences calculated through the analytical steady-state solutions of Eq. (4.10) are also plotted. As expected, the system quickly reaches steady state on

time scales on the order of $1/\gamma_1 \approx 100$ ns. Once the system reaches steady-state, there is reasonable agreement between the numerical calculations and the analytical solutions. The discrepancy between the numerical and analytical solutions is due to effects that are related to the high intensity of the lasers, such as depopulation of the ground state and the break down of the perturbative approximation. We have checked that in the case of low intensity laser fields there is very close agreement between the numerically and analytically calculated coherences. However these lower intensity values are not sufficient to attain negative refraction.

Using the equations of the density matrix we numerically integrated the coherences as a function of time for a given frequency position until they reached a steady state value. We then repeated this integration procedure for each frequency value in an array of equally spaced points to see the frequency dependence of the coherences as the probe beam is scanned across the resonance. The agreement between the numerical and analytical solutions can also be seen in Fig. 4.11, which plots the numerically solved values of the coherences and the analytical solutions as the probe frequency is scanned across the resonance.

There remained a discrepancy between the resulting coherences of our numerical simulation and our analytical results with the same parameters seen in Figs. 4.3-4.6 The strengths of the two Raman resonances were not properly balanced so as to lead to vanishing absorption. As was mentioned earlier in Section 4, the local field effects that result in negative refraction with minimal absorption are correlated to the vanishing absorption of the Raman resonances. To resolve this, we adjusted the strength of the gain Raman resonance from $I_{\mathcal{C}1} = 0.27$ MW/cm^2 to 0.485 MW/cm^2 in our numerical simulations. Using this adjusted intensity, we were able to numerically calculate a refractive index that closely resembled our analytical results as seen in Fig. 4.12.

To gain insight to the discrepancies between numerical and analytical results we considered the break down of the perturbative approximation in our analytical approach. Figure 4.13 shows the evolution of the population of the ground state, ρ_{gg}. Although the system initially starts in the ground state ($\rho_{gg} = 1$), the population of this state drops to $\rho_{gg} = 0.814$ as the laser fields are applied. The system, therefore, remains reasonably within the perturbative approximation since only about 18.6 % of the population is moved from the ground state.

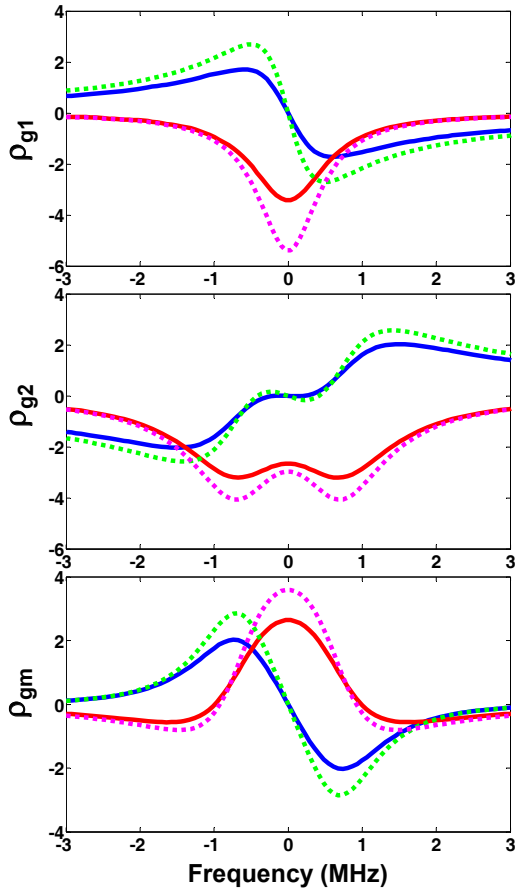

Figure 4.11 The real (solid blue) and imaginary (solid red) parts of the numerically solved steady state values of the coherences ρ_{g1}, ρ_{g2}, and ρ_{gm} (in arbitrary units) as they are scanned across resonance. These are compared to the real (dotted green) and imaginary (dotted magenta) parts of the coherences calculated using the analytical steady state solutions with the same parameters.

4.7 Conclusions

To summarize, we have outlined a Raman based approach for achieving negative index of refraction with low absorption in the optical region of the spectrum. Differing from the meta-material approach, our technique utilizes atomic systems that are driven with lasers in their internal states. The key advantage of our approach is that our technique does not require the simultaneous presence of an electric dipole and a magnetic dipole transition near the same wavelength. This gives

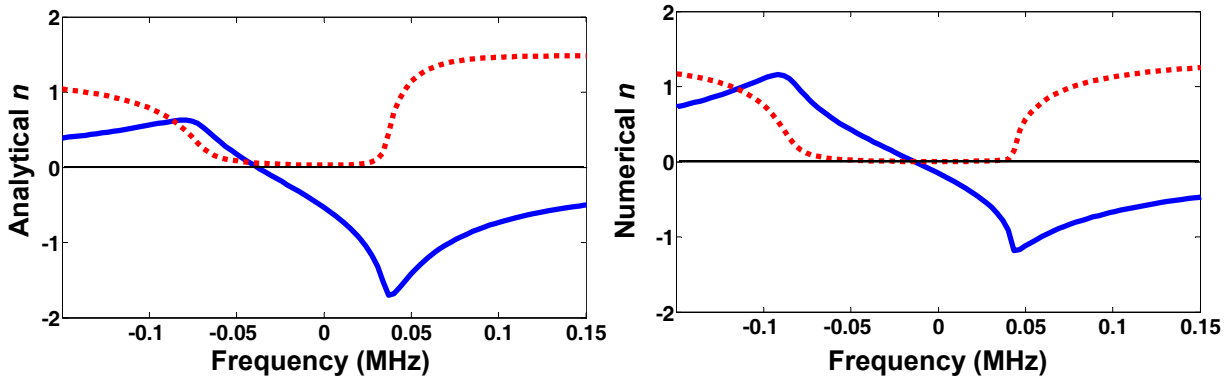

Figure 4.12 The real (solid blue) and imaginary (dotted red) parts of the index of refraction as calculated using our analytical formalism (left) and our numerically solved model (right) for a density of $N = 5 \times 10^{16}$ cm^{-3}. All of the parameters are the same, except the intensity of laser field $\mathcal{E}_{C1}$ was adjusted to $I_{C1} = 0.485$ MW/cm^2 in the numerical model from the value used in previous figures of $I_{C1} = 0.27$ MW/cm^2, which was used in the analytical result.

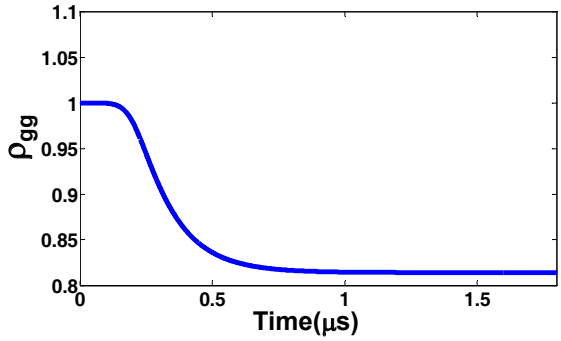

Figure 4.13 The ground state population of the system in our numerical simulation initially starts at 100 % and decreases in time as the laser fields are gradually turned on, eventually reaching a steady state value of 81.4 %.

large flexibility in the requirements for the energy level structure, which allows for the possibility of experimental implementations using the rich structure of rare-earth atoms.

There are many open questions that yet need to be addressed. One future direction would be to perform detailed theoretical modeling to identify the most suitable atomic species and experimental system for observing negative refraction. As discussed above a careful evaluation of the

achievable atomic densities and the linewidths is needed. A first step in this direction will be discussed in the next chapter. If achieved, negative refraction in atomic systems may have significant implications for a number of research areas. As mentioned above, one key practical application is in optical imaging science. As the frontiers of science and engineering approach the nanoscale, it becomes ever more important to devise optical imaging techniques with nanometer resolution. In recent years, overcoming the diffraction barrier has been the subject of intense theoretical and experimental research [54, 64, 10, 55, 12, 25, 59, 7]. Perfect lenses constructed from negative index materials may provide a unique approach for resolving nanoscale objects and may therefore have far reaching practical implications. These devices may also be used to reduce the smallest feature size of a lithographic mask. This is particularly important since lithographic resolution currently determines the size and the processing power of every semiconductor integrated circuit.

Chapter 5

Implementations of negative index approach using rare-earth atoms

5.1 Introduction and background

Rare earths of the lanthanide series have some of the most complex electronic spectra of known elements due to the rich structure of the open f-shell. Although the first spectra of rare-earths were obtained as early as the 1930s, detailed investigation and understanding of their electronic structure had to wait until the 1960s when tunable laser sources were developed and computers became powerful enough to enable reasonably accurate calculations [83, 159, 143, 157]. The interest in rare-earths has been continually growing over the last two decades due to applications in diverse research areas including quantum information storage and precision measurement of the electron electric dipole moment.

In this chapter we investigate the possibility of experimental implementations of our technique for negative refraction by considering systems of rare-earth atoms. The technique for negative refraction that we have discussed is flexible in that it doesn't require a strong magnetic and a strong electric dipole transition at almost exactly the same wavelength, however the trade-off is that the greater the difference between the transition wavelengths, the greater the required intensity of the Raman coupling lasers. We consider the rich level structure of the rare-earth atoms, where ideally we can find systems that have strong optical electric and magnetic dipole transitions with closely spaced wavelengths and suitable hyperfine structure that can be used to induce Raman transitions with the probe and coupling lasers. In our investigation of rare-earth atom transitions we use Cowan's atomic structure code [22] to calculate theoretical estimates for transition wavelengths

and dipole matrix elements by using ab initio relativistic Hartree-Fock methods. We will consider both systems of neutral atom vapors and crystal solids doped with rare-earth ions.

5.2 Neutral rare-earth atom vapors

In this section, we discuss possible experimental implementations of our technique in two rare-earth atomic species: Erbium (Er) and Dysprosium (Dy). By using Cowan's atomic structure code [22], we have found suitable transitions from the ground level in both of these atomic species. Further research may identify different atomic species and transitions that are better suited to our technique. However, we feel the two schemes in Er and Dy serve as a good starting point and also demonstrate the flexibility of our scheme. Figure 5.1 details the transitions in Er where we consider the $4f^{12}(^3H_6)6s^2\ ^3H_6(J=6) \rightarrow 4f^{12}(^1I_6)6s^2\ ^1I_6(J'=6)$ magnetic dipole transition and the $4f^{12}(^3H_6)6s^2\ ^3H_6(J=6) \rightarrow 4f^{12}(^1G_4)6s6p(^1P_1^o)\ ^1H_5^o(J'=5)$ electric dipole transition. The wavelengths of these two transitions are in the ultraviolet, and they differ by only 2.2 nm (335.3 nm for the magnetic dipole and 337.5 nm for the electric dipole). The ^{167}Er isotope has a nuclear spin of $I = 7/2$ and occurs with a natural abundance of 23%. The resulting hyperfine levels [19, 58] can be used to induce Raman transitions with the probe and the control lasers. By using Cowan's code we have calculated the magnetic dipole reduced matrix element to be $\langle J||\hat{\mu}||J'\rangle = 0.1\mu_B$ (μ_B: Bohr magneton) and the electric dipole reduced matrix element to be $\langle J||\hat{d}||J'\rangle = 0.2ea_0$ (e: electron charge, a_0: Bohr radius), both of which are reasonably strong.

For Dysprosium, we consider the ^{161}Dy isotope (natural abundance of 19%, nuclear spin of $I = 5/2$) with a level structure similar to that of Fig. 5.1. We have identified the $4f^{10}(^5I_8)6s^2\ ^5I_8(J=8) \rightarrow 4f^{10}(^3K_7)6s^2\ ^3K_7(J'=7)$ and the $4f^{10}(^5I_8)6s^2\ ^5I_8(J=8) \rightarrow 4f^9(^2M^o_{17/2})5d_{3/2}6s^2\ ^5K^o_7(J'=7)$ magnetic and electric dipole transitions as suitable candidates for our technique. The wavelengths of these two transitions are 484 nm for the magnetic dipole and 484.8 nm for the electric dipole. The calculated reduced matrix elements for the two transitions are $\langle J||\hat{\mu}||J'\rangle = 0.06\mu_B$ and $\langle J||\hat{d}||J'\rangle = 0.19ea_0$, respectively. Although these matrix elements are slightly weaker than those of Erbium, ^{161}Dy has the key advantage that the electric and magnetic transition wavelengths are closer. The hyperfine splitting of the ground level for ^{161}Dy is about 1 GHz [18].

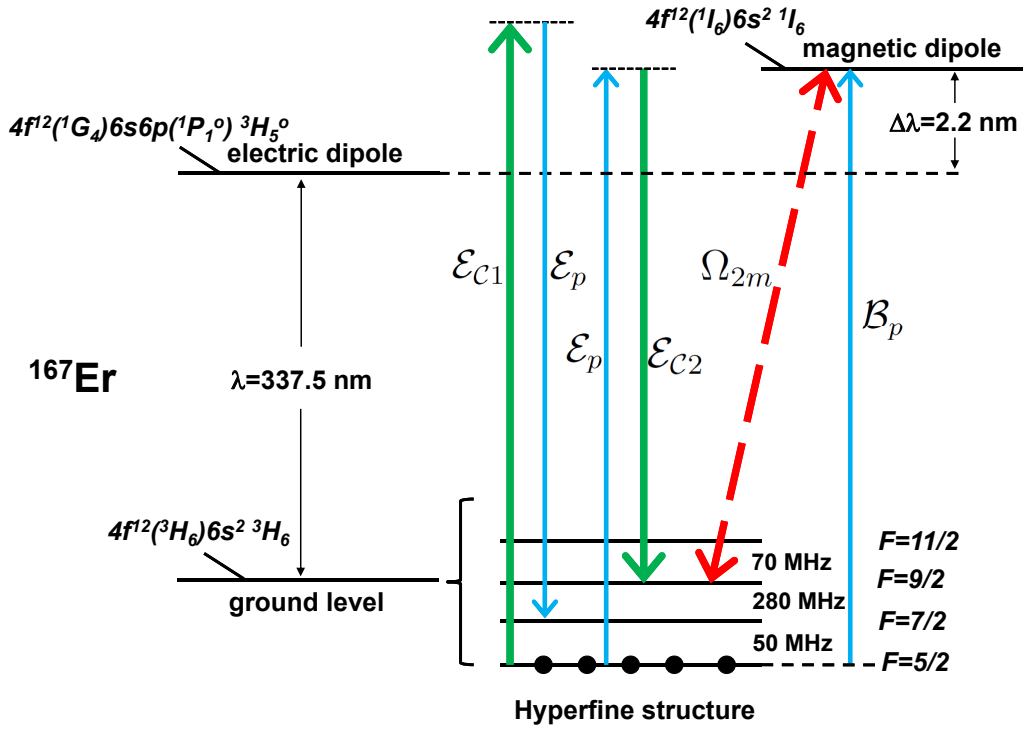

Figure 5.1 The proposed experimental scheme in atomic ^{167}Er. The hyperfine structure of the ground level is used to induce Raman transitions with the probe beam and the control lasers. For simplicity, the hyperfine structure of the excited levels is not shown. A similar level scheme can also be found for atomic ^{161}Dy (see text for details). The central wavelength for ^{161}Dy is 484.8 nm and the difference of the two transition wavelengths is $\Delta\lambda = 0.8$ nm.

Obtaining negative refraction with the parameters of Chap. 4 (densities exceeding 10^{16} cm^{-3} with optical transition linewidths at the MHz level) will undoubtedly be a very challenging experiment, and there are many open questions. For experimental implementation of our approach with rare-earth atom vapors, we consider laser-cooled and trapped high-density ultracold atomic clouds [88, 9, 8, 81] and magnetically trapped atom clouds cooled through buffer gas cooling [47]. A detailed theoretical modeling to investigate negative refraction with these three different atomic systems will be among our future investigations. The modeling will need to go beyond what we have discussed in the previous chapter and will include effects such as the collisional broadening of the magnetic transition, dipole-dipole interactions, and various inelastic and elastic collision processes. The collisional broadening and dipole-dipole interactions will determine the magnetic

transition and Raman linewidths and will have a direct effect on the magnitude of the refractive index that can be achieved. We note that, since the laser beams are far-detuned from the electric dipole transition, our scheme is less sensitive to the broadening of the excited electronic states. The inelastic and elastic collision processes will determine the largest achievable densities in the trap. The cross sections for most of these processes are not known, but some progress has been made experimentally [161]. Furthermore, it may be possible to calculate some of these cross sections using ab-initio methods [22].

Both Er and Dy have been laser cooled and trapped recently with trapped atom numbers as high as half a billion and atomic temperatures at the microKelvin level [88, 9, 8, 81]. Although the structure of these atoms is highly complex, laser cooling is possible because of the large magnetic moment of these atoms. The metastable states are trapped in a quadrupole magnetic field and laser cooling is achieved without any repumping lasers, the so-called "repumperless" MOT (magneto-optical trap).

It is well-known that MOTs are not suitable for achieving very high atomic densities due to effects such as radiation trapping. To obtain high density atomic clouds, one approach is to construct an optical dipole trap. Such dipole traps can be formed by focusing an intense very-far-detuned laser beam overlapping with the MOT cloud. Recently, ultracold atomic densities approaching 10^{15} cm^{-3} have been demonstrated in atomic Ytterbium (Yb) [142]. By using evaporative cooling in the optical trap, such clouds can be cooled to quantum degeneracy and of particular importance, degenerate gases of ultracold erbium, dysprosium, and ytterbium have recently been demonstrated [42, 80, 1]. These are very exciting developments, and we feel that high density clouds in optical dipole traps show considerable promise for studies of negative refraction. In addition to studies of negative refraction, such traps will likely have significant implications for other research areas including precision spectroscopy and dipolar physics [81].

An alternative approach to laser cooling is buffer gas cooling and magnetic trapping [47]. Although buffer gas cooling only achieves milliKelvin level temperatures, the trapped atom numbers are significantly higher. Using this approach, Doyle and colleagues have demonstrated trapping of about 10^{12} atoms in many of the rare-earth species, including Er and Dy [47]. Due to the large

initial trapped atom number, buffer gas cooling and magnetic trapping may serve as an excellent starting point for producing high-density clouds. By using evaporative cooling in the magnetic trap, or by transferring atoms to a dipole trap and then performing evaporative cooling, it may be possible to achieve densities exceeding 10^{15} cm^{-3} using this approach.

5.3 Rare-earth doped crystals

Rare-earth doped crystals at cryogenic temperatures show considerable promise for the experimental demonstration of our technique. We noted in the above section that a number of neutral rare-earth species have been laser cooled and trapped recently, however, these ultracold clouds currently do not have the necessary densities for achieving negative refraction. The highest demonstrated density in these systems is $\approx 10^{14}$ /cm^3, which is more than two orders of magnitude smaller than the densities required for negative refraction. Rare-earth ions in doped crystals at cryogenic temperatures offer a more promising alternative route for negative refraction because of the high densities available. The quantum description of rare-earth doped crystals has a discrete level structure that resembles a free ion for the 4f levels rather than the band structure of a solid-state system and many quantum coherence effects such as EIT and quantum memories have recently been observed in these systems [45, 46, 147, 65, 66, 67, 72]. Below we discuss negative refraction in two types of crystals, Tb^{+3}:CaF_2 and Pr^{+3}:LaF_3.

We first would like to summarize a number of defining features of these systems [83]:

(i) Rare-earths typically form trivalent ions in crystals with only $4f$ electrons remaining in the outer shell in the ground configuration, for example [Xe]$4f^8$ for Tb^{+3}, and [Xe]$4f^2$ for Pr^{+3}. The $4f$ shell is tightly bound to the nucleus and the $4f$ electronic configuration interacts weakly with the crystal environment. As a result, the intra-configurational $4f \rightarrow 4f$ transitions are sharp, and they are very much like free-ion transitions that are only weakly perturbed by the crystal field. At cryogenic temperatures, homogeneous linewidths well-below 1 MHz are routinely observed for the $4f \rightarrow 4f$ transitions [83, 84, 35]. Optically excited fluorescence level lifetimes exceeding 1 ms have also been demonstrated in these systems. Furthermore, due to the absence of atomic motion,

there is no Doppler broadening nor atomic diffusion. Because of these properties, rare-earth doped crystals more closely resemble ultracold clouds than warm vapors.

(ii) These systems routinely use doping fractions exceeding 0.1%, which corresponds to rare-earth ion densities of about 10^{20} /cm^3. These densities are much higher than what can be achieved in neutral ultracold clouds or atomic vapors. The rare-earth ion-ion interactions do not significantly affect the $4f$ configuration at these densities.

(iii) Because of the interaction with the crystal field, there is an inhomogeneous broadening of the intra-configurational $4f \rightarrow 4f$ lines [83, 84]. This broadening depends on the crystal host and the specific levels, but is typically a few GHz in crystals such as CaF_2 and LaF_3. This broadening is unusually small for a solid state system, which is again a result of the $4f$ configuration being relatively well shielded from the crystalline environment. Although a quantitative understanding of this broadening has not yet been developed, it is known to be a result of crystal strains and local variations in the crystal field.

(iv) The inhomogeneous broadening can be overcome at the expense of a reduction in effective atomic density using spectral hole burning techniques [71, 87, 70]. These techniques lie at the heart of the recent EIT and quantum memory demonstrations in these systems. The idea is to selectively optically pump a subset of the atoms whose resonance frequencies are within about 1 MHz of each other, using an appropriate optical pumping laser. One essentially burns a 1 MHz wide hole under the broad GHz inhomogeneous profile, and only uses atoms whose resonance frequencies lie within the hole. This reduces the usable atomic density to 10^{20} /cm$^3\times$ (1 MHz/1 GHz) = 10^{17} /cm^3, which is still quite large compared to what can be achieved using other approaches. One therefore obtains an "ultra-cold" atomic system with a density of about 10^{17} /cm^3 with $4f \rightarrow 4f$ transition linewidths of about 1 MHz.

(v) Other electronic configurations such as $4f5d$ extend significantly beyond the $4f$ shell, and strongly interact with the crystal field [158, 149, 151]. Free-ion levels are split through the crystal field and form a band of levels. Some of these levels may be lifetime broadened and the corresponding $4f^x \rightarrow 4f^{x-1}5d$ inter-configurational transitions to these levels may have narrow

linewidths [150]. However, some levels of the $4f5d$ configuration are strongly coupled to the crystal conduction band, and the corresponding excitations may exhibit broad features.

(vi) The hyperfine levels of the ground level are stable and long-lived, and they can be used to induce Raman transitions for the probe laser beam.

In a free ion, intra-configurational $4f^x \rightarrow 4f^x$ transitions are electric dipole forbidden since both lower and upper states have the same parity. In a crystal, these transitions become weakly electric dipole allowed due to mixing with the crystal field. However, this mixing is typically small, and intra-configurational transitions remain strongly magnetic dipole in nature. For implementation of our approach in rare-earth doped crystals, we plan to use magnetic dipole $4f^x \rightarrow 4f^x$ intra-configurational transitions and detuned electric dipole excitation using the inter-configurational $4f^x \rightarrow 4f^{x-1}5d$ transitions. We next present an evaluation of this approach in two different rare-earth doped systems.

5.3.1 Negative refraction in Tb^{+3}:CaF_2

Our current understanding indicates that Tb^{+3}:CaF_2 is one of the most promising systems for studies of negative refraction [102, 97, 96, 27]. Tb^{+3} is the rare-earth ion with the smallest energy spacing between the $4f$ and $4f5d$ configurations. As a result, the electric dipole response can be obtained using detuned excitation from the ground level to the $4f5d$ configuration. CaF_2 host crystal has excellent mechanical and optical properties with good transmission through much of the optical region all the way down to 130 nm. The detailed energy level diagram is shown in Fig. 5.2. The ground level of Tb^{+3} is $4f^8\ ^7F_6$ and has been established both experimentally and also through Hartree-Fock calculations [97, 16, 144]. By using Cowan's atomic structure code [22], we have identified a strong intra-configurational $4f^8\ ^7F_6 \rightarrow 4f^8\ ^5F_5$ magnetic dipole transition at a wavelength of 282 nm, with a transition strength of $\langle J||\hat{\mu}||J'\rangle = 0.2\mu_B$. Although this transition has not been observed experimentally, we have found two publications that calculate this transition wavelength to within a few nm of the predictions of the Cowan's code [97, 16]. The lowest level of the $4f^7 5d$ configuration is the so-called high-spin (HS) band which has recently been observed experimentally in Tb^{+3}:CaF_2 using synchrotron light from DESY [149]. In CaF_2 crystal, this band

starts at a wavelength of 265 nm with the levels split through the crystal field to a total width of about 5 nm. As shown in Fig. 5.2, the predicted wavelength difference between the magnetic dipole transition and the HS band is $\Delta\lambda = 17$ nm.

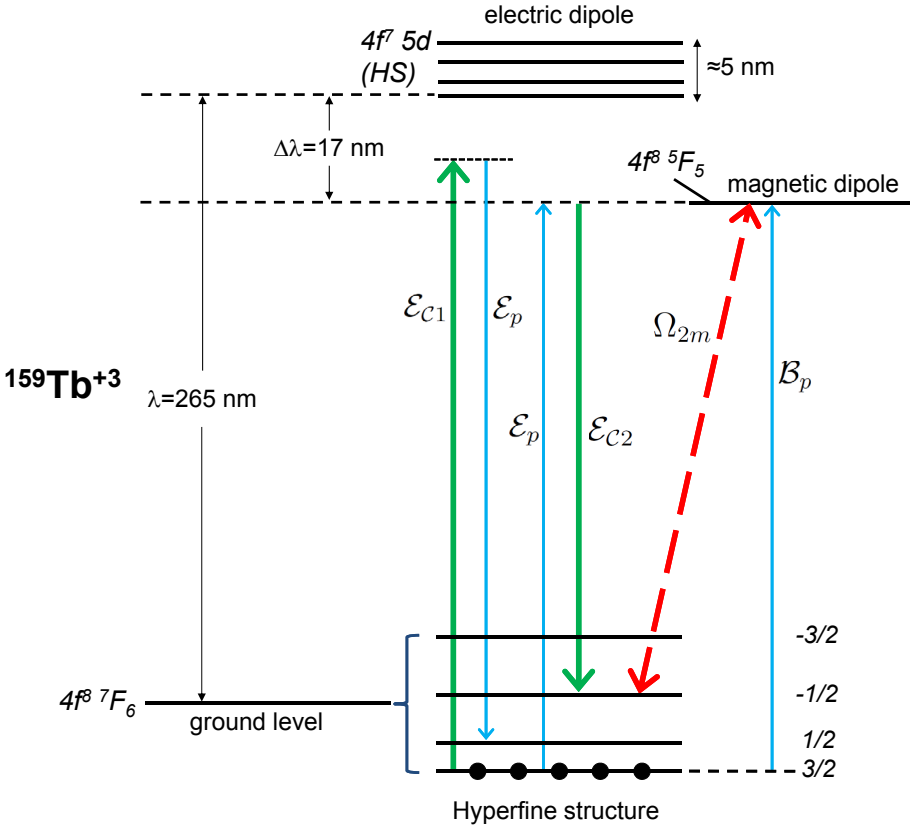

Figure 5.2 The proposed scheme for achieving negative refraction in ^{159}Tb^{+3}. We plan to use intra-configurational $4f^8\ ^7F_6 \rightarrow 4f^8\ ^5F_5$ magnetic dipole transition at a wavelength of 284 nm. The electric dipole response is obtained by Raman excitation through the $4f^7 5d$ configuration. The laser beams are detuned by $\Delta\lambda = 17$ nm from the bottom of the $4f^7 5d$ configuration (the HS band). The hyperfine structure of the ground level in the presence of an external magnetic field is also shown.

Hyperfine structure: The hyperfine structure of Tb^{+3} has been studied in detail in a number of publications [76, 103]. The crystal electric field lifts the degeneracy of the M_J levels and the ground level is a $M_J = \pm 6$ doublet. The stable isotope of terbium is ^{159}Tb with a nuclear spin of $I = 3/2$. In atomic physics literature, hyperfine coupling is typically characterized by total angular momentum $F = I + J$ where the states are represented using quantum numbers $JIFM_F$.

In the presence of external fields for which the interaction with the fields is large compared to the interaction between I and J, it is physically more meaningful to work in the decoupled basis with quantum numbers JM_JIM_I. Without any applied external magnetic field, the hyperfine interaction results in a pair of degenerate doublets, $M_I = \pm 1/2$ and $M_I = \pm 3/2$, that are split by about 10 MHz due to the crystal electric field. The degeneracy can be lifted through the Zeeman effect by applying an external DC magnetic field, producing the hyperfine structure shown in Fig. 5.2. The Zeeman shift of the levels is about 0.1 MHz/Gauss, and as a result it is easy to achieve frequency splittings between the hyperfine levels of about 100 MHz. Due to the relatively small spread in frequency, the probe, control, and magnetoelectric cross coupling lasers can be obtained from the same laser system using, for example, acousto-optic modulators.

Spectral hole burning: The experiment will start with optically pumping the atoms to a selected hyperfine level such as $M_I = 3/2$ as shown in Fig. 5.3. As experimentally demonstrated in a number of papers [76, 103], this can be achieved using frequency-selective excitation through the hyperfine structure of the $4f^8\,{}^5D_4$ level near an excitation wavelength of 488 nm. Although the $4f^8\,{}^7F_6 \rightarrow 4f^8\,{}^5D_4$ transition is electric dipole and magnetic dipole forbidden in a free-ion, it becomes slightly dipole allowed due to mixing with the crystal field. Optical pumping is accomplished using three laser beams, E_{h1}, E_{h2}, and E_{h3}, that excite the atoms from levels M_I=1/2, -1/2, and -3/2, respectively. By choosing the intensity of these lasers appropriately, one can burn a spectral hole of about 1 MHz wide in the absorption spectrum from these three levels. This essentially means that only atoms whose resonant frequencies lie within 1 MHz of each other are continually excited to $4f^8\,{}^5D_4$ and are optically pumped to the M_I=3/2 ground hyperfine level, which is not addressed by the laser beams (producing an "anti-hole" in the absorption spectrum from this level). At cryogenic temperatures, spectral hole and anti-hole lifetimes (i.e., the duration that the atoms stay pumped after optical pumping lasers are turned-off) can be very long. For example, spectral hole lifetimes exceeding 10 minutes have been reported in Tb^{+3}:$LiYF_4$ [76].

Numerical calculations in Tb^{+3}: We next present preliminary numerical calculations for evaluating our approach in Tb^{+3}:CaF_2. The principle approximations that we make in these calculations are: (i) We ignore the mixing of the $4f$ configuration with $4f5d$ due to the presence of the crystal

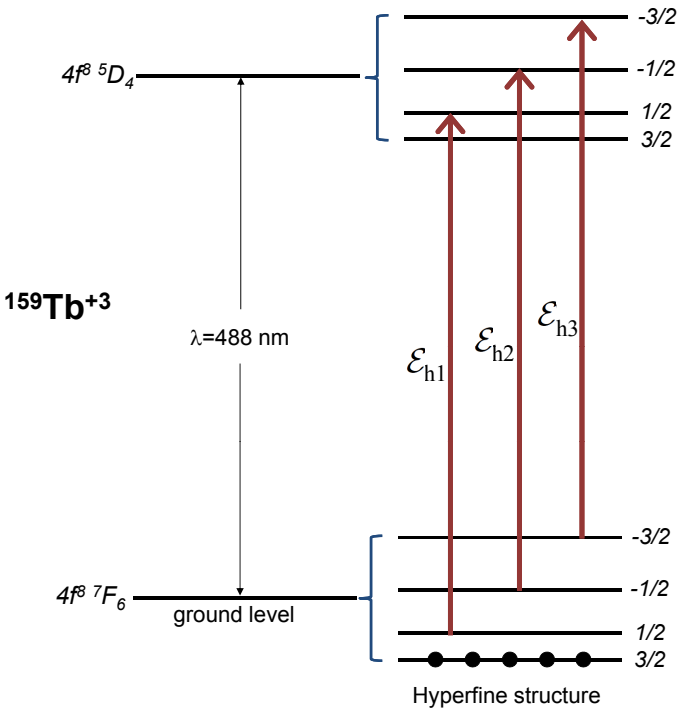

Figure 5.3 Spectral hole burning in $^{159}Tb^{+3}$. Three optical pumping lasers, E_{h1}, E_{h2}, and E_{h3}, address atoms that are in ground hyperfine levels M_I=1/2, -1/2, and -3/2, burning a spectral hole with a width of about 1 MHz in the absorption spectrum from these levels. The atoms whose resonance frequencies lie within the spectral hole are pumped to the M_I=3/2 ground level.

field. As a result of this mixing, the $4f^8\ ^7F_6 \rightarrow 4f^8\ ^5F_5$ magnetic dipole transition acquires a slight electric dipole character. Such mixing would not necessarily be detrimental; in fact it may result in additional useful contributions to the refractive index. (ii) For the magnetic dipole and Raman transitions we assume a homogeneous linewidth of 1 MHz, which is common for rare-earth doped crystals at cryogenic temperatures. Typically lifetime broadening and coupling to crystal phonon modes are the dominant contributions to the homogeneous linewidth [156]. (iii) We assume an inhomogeneous broadening of 1 GHz for the intra-configurational $4f \rightarrow 4f$ transitions (i.e. for the spectral hole burning and magnetic dipole transitions), which is again common for these systems. (iv) The intense control laser beams can, in principle, couple the $4f^8\ ^5F_5$ level to the high-lying levels of the $4f5d$ configuration. We ignore this coupling, since the data of Ref. [149] show that there aren't any levels at the correct energy in the $4f5d$ configuration (i.e. at the 282/2=141 nm

excitation wavelength from the ground level). (v) Meijerink and colleagues have recently observed lifetime broadened sharp inter-configurational $4f \rightarrow 4f5d$ transitions from the ground level in Tb^{+3}:CaF_2, including transitions to the HS band [149, 150]. However, in our scheme, one would expect a shorter lifetime of these levels due to interaction with the intense control laser beams that would couple the HS band to higher levels in the $4f5d$ configuration. To take into account this coupling, we perform a back-of-the-envelope calculation of the Fermi's golden rule transition rate. This gives a lifetime of ≈ 1 ns for the levels in the HS band, which is much shorter than the radiative lifetime. Although in our scheme the lasers are very far detuned from the HS band levels, the linewidth of these levels is important since it determines the power broadening of the Raman lines due to the control laser beams.

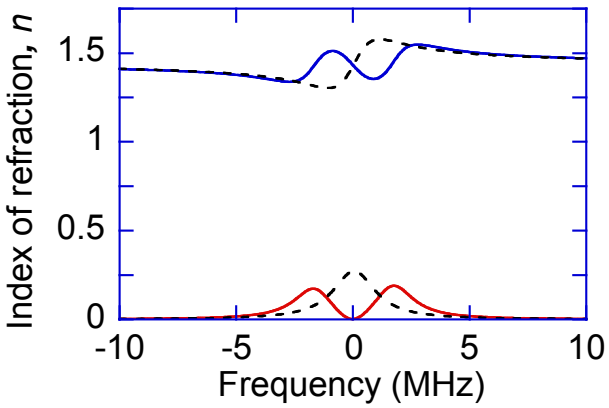

Figure 5.4 The real and the imaginary parts of the refractive index in 0.2% doped Tb^{+3}:CaF_2 with (solid lines) and without (dashed lines) magnetoelectric cross coupling. This simulation is performed using relatively conservative parameters.

Figure 5.4 shows the real (solid blue line) and the imaginary (solid red line) parts of the refractive index in Tb^{+3}:CaF_2 for relatively conservative parameters. We assume a doping density of 0.2%, and assume spectral hole burning with a width of 1 MHz under the broad inhomogeneous profile. This produces an effective Tb^{+3} density of 4.9×10^{16} /cm^3. We take the intensities of the two control lasers to be about 100 MW/cm^2, which is significantly lower than the optical damage threshold of the crystal host. These type of intensities are accessible even in the continuous-wave

domain; a 1 W beam focused to an area of 1 μm $\times$ 1 μm using a microscope objective lens yields this required intensity. We take the magnetoelectric cross coupling rate to be $\Omega_{2m} = i2\pi\times 3.3$ MHz. Although negative refraction is not achieved for these parameters, there are large variations in the refractive index, and the interference profile is such that absorption cancels at the line center. For comparison, the real and imaginary parts of the refractive index without cross-coupling ($\Omega = 0$) are also shown (dashed lines). As the figure illustrates, the lineshapes for the refractive index depend critically on the cross coupling. Experimentally, a first goal would be to observe these lineshapes and also the dependence of the refractive index on the magnetoelectric cross coupling rate. If demonstrated, to our knowledge, this would be the first observation of magnetoelectric response in a rare-earth doped crystal system.

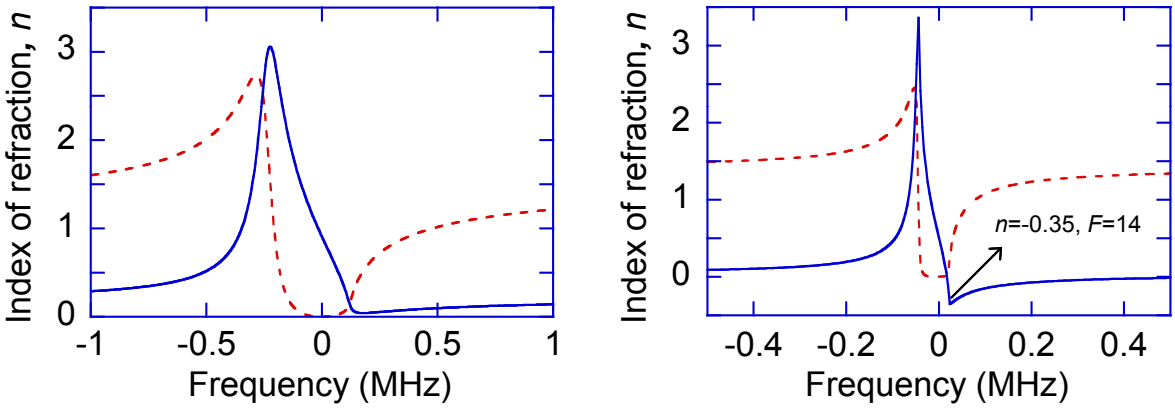

Figure 5.5 The real (solid blue lines) and the imaginary (dashed red lines) parts of the refractive index in (a) 0.5% doped and (b) 3% doped Tb^{+3}:CaF_2. For part (b) we achieve a refractive index of $n = -0.35$ with a figure of merit of $F = 14$.

Figure 5.5 shows speculative results for more stringent parameters. We assume a doping density of 0.5% for part (a) and 3% for part (b). We again assume hole burning with a width of 1 MHz, producing effective densities of 1.2×10^{17} /cm^3 and 7.3×10^{17} /cm^3 for parts (a) and (b), respectively. We take the intensities of the control beams to be pushed to the optical damage threshold of the crystal host, to about 10 GW/cm^2. For the numerical simulation of part (b), we achieve a refractive index of $n = -0.35$ with a figure of merit of $F = 14$. The long term goal of experimental efforts will be to demonstrate results similar to those shown in Fig. 5.5. To our knowledge,

these simulations are the first time that the possibility of observing negative refraction in a real atomic system is discussed. Although observing the results of Fig. 5.5 will undoubtedly be a challenging experiment, the assumed experimental parameters appear to be within reach. Furthermore, further research into rare-earth doped crystals may identify a system in which negative refraction is achieved with more easily accessible parameters compared to Tb^{+3}:CaF_2. In particular, more closely spaced electric dipole and magnetic dipole transitions with stronger matrix elements would significantly lower the intensity requirement on the control laser beams.

5.3.2 Negative refraction in Pr^{+3}:LaF_3

We have also identified Pr^{+3}:LaF_3 as another promising candidate for studies of negative refraction. Pr^{+3} doped systems have been studied extensively in quantum coherence experiments such as EIT [147, 65]. We have chosen lanthanum fluoride as the host crystal because the level positions of Pr^{+3}:LaF_3 have been experimentally measured in Ref. [34]. Much of the above discussion applies to this system [11, 79, 78, 89]. Figure 5.6 shows the detailed energy level structure. The ground state of Pr^{+3} is $4f^2\ ^3H_4$. We propose to use the excited level $4f^2\ ^3P_1$ as our starting level for this experiment. The atoms are transferred from the ground level to $4f^2\ ^3P_1$ using the spectral hole burning laser E_h near a wavelength of 455 nm. At cryogenic temperatures, the lifetime of level $4f^2\ ^3P_1$ can be as long as 100 μs [83]. As a result, once the atoms are optically pumped to this level, they will have sufficient time to interact with the probe and control laser beams.

We plan to use the $4f^2\ ^3P_1 \rightarrow 4f^2\ ^1S_0$ intra-configurational magnetic dipole transition near a wavelength of 392 nm. Cowan's code gives the strength of this transition to be $\langle J||\hat{\mu}||J'\rangle = 0.35\mu_B$. The transitions from the $4f^2\ ^3P_1$ level to the $4f5d$ configuration are strongly electric dipole and start at a wavelength of 360 nm. The stable isotope of praseodymium is ^{141}Pr with a nuclear spin of $I = 5/2$. The resulting hyperfine structure in the absence of a magnetic field is shown in Fig. 5.6. The ground level $4f^2\ ^3H_4$ has a similar hyperfine structure (not shown in Fig. 5.6), and by choosing E_h appropriately, the atoms can initially be pumped to $M_I = \pm 5/2$. With the atoms pumped, the probe and the control lasers will induce Raman transitions between

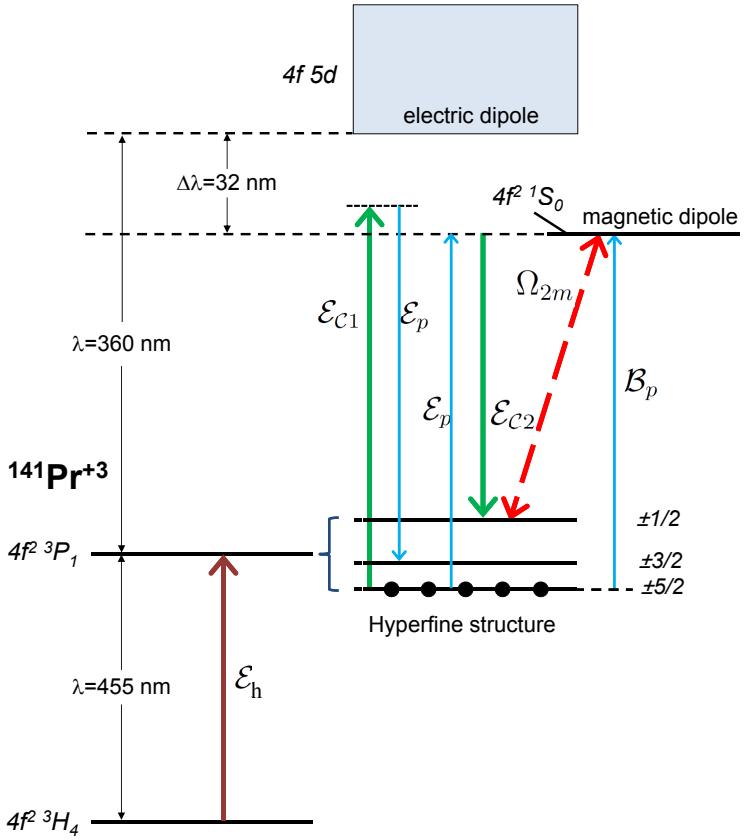

Figure 5.6 The proposed scheme for achieving negative refraction in $^{141}\mathrm{Pr}^{+3}$. The atoms are first optically pumped to $4f^2\ ^3P_1$. We plan to use the $4f^2\ ^3P_1 \rightarrow 4f^2\ ^1S_0$ intra-configurational magnetic dipole transition near a wavelength of 392 nm. The electric dipole response is obtained using detuned Raman excitation through the $4f5d$ configuration. The hyperfine structure of $4f^2\ ^3P_1$ in the absence of an external magnetic field is shown. For clarity, the hyperfine structure of the other levels are not shown.

the hyperfine levels. The scheme in Pr^{+3} has the key drawback that the probe, control, and cross-coupling laser beams address the excited $4f^2\ ^3P_1$ level, and not the ground level of the system.

5.4 Conclusions and future work

To summarize, we have proposed several atomic systems that potentially may be implemented to experimentally obtain a negative index of refraction with low absorption in the optical region of the spectrum. In contrast to other approaches that rely on metamaterials, we will use lasers to

drive internal states of atomic systems. Our technique does not require the simultaneous presence of an electric dipole and a magnetic dipole transition near the same wavelength, so we are able to consider implementations in existing appropriate level structures. We have evaluated our technique in rare-earth doped crystals and neutral atom vapors and identified Tb^{+3}:CaF_2 and Pr^{+3}:LaF_3 and ultracold Er and Dy as possible systems for experimentally demonstrating our approach. To our knowledge, this is the first time where a real atomic system has been identified and discussed for observing negative refraction.

In future proposed work, we plan to extend our preliminary calculations and perform detailed simulations for these systems of rare-earth atoms. In particular, for the rare-earth doped crystals improved models will need to take into account the mixing of the levels due to the presence of the crystal field and coupling of the magnetic dipole excited level to the $4f5d$ configuration due to the intense control laser beams. One of the challenges is how to accurately model the high energy levels of the $4f5d$ configuration, which are significantly perturbed by the crystal field, and may also be strongly coupled to the crystal conduction band. Recently, there have been a number of papers that calculate the discrete levels of the free-ion $4f5d$ configuration using relativistic Hartree-Fock methods [32, 31]. One approach would be to take these results as a starting point and assume a large broadening with a width of about 10 nm for each level due to coupling to the conduction band. Such calculations typically reveal more than 100 levels, although the strongest of the levels may be utilized as a first approximation.

We also plan to perform preliminary experiments in these systems in hot atom vapors or room temperature doped crystals, to study the spectroscopy of the electric and magnetic dipole lines. To our knowledge, the specific transition lines that we plan to study have never before been investigated in detail. Spectroscopy of the transitions is necessary to verify the transition wavelengths and magnetic and electric dipole transition strengths, line broadenings, hyperfine structure, and demonstrate spectral hole burning and optical pumping. The goal of these early experiments is to set the stage for future, more challenging negative refraction experiments at cryogenic or ultracold temperatures. Additionally, we expect these results will be of considerable interest to the broader EIT, quantum computing, and rare-earth physics communities.

The next goal would be to demonstrate magnetoelectric (chiral) response. Chiral response may be achieved at low densities and a basic form of chirality has already been demonstrated in Rb vapor [120]. As discussed in previous sections, the magnetoelectric coupling results in significant contributions to the refractive index. One approach would be to study the real and imaginary parts of the refractive index (absorption and phase shift) for the probe wave, as the strength or the phase of the cross coupling rate, Ω_{2m}, is varied. With $\Omega_{2m} = 0$ (no cross coupling), the system reduces to three resonances (two electric dipole Raman resonances and a magnetic resonance). As a starting point, these three resonances can be studied independently. As Ω_{2m} increases, the interference and the cross-coupling of these resonances will be observable.

Chapter 6

Conditional phase shifter via refractive index enhancement

6.1 Introduction and background

Traditionally photons have been considered to be noninteracting particles, but advances in nonlinear and quantum optics have shown that significant light-light interactions can occur in highly polarizable media [127, 13]. An important such interaction is cross phase modulation because of its potential applications to optical information processing. Cross phase modulation is a nonlinear interaction where the phase of a light field is modified by an amount determined by the intensity of another light field. The key challenge is to develop a technique to achieve a cross phase modulation phase shift of π radians between two weak light fields with minimal dissipation of the fields. Realization of this phase shift with single photon pulses could lead to development of quantum logic via a quantum phase gate [146]. In this chapter we suggest an implementation of a phase shifter where a conditional switch beam induces a cross phase modulation on a probe beam propagating in a refractive index enhanced medium.

Before proceeding further, we would like to discuss some important results in the nonlinear interaction of weak light beams in atomic media exhibiting electromagnetically induced transparency (EIT) [49]. EIT schemes with cold atoms are a popular choice to implement cross phase modulation of weak light pulses because of the resonantly enhanced giant Kerr nonlinearity and the suppression of the absorption of the beam [121, 50]. The double-EIT suggestion for cross phase modulation by Lukin and Imamoğlu [82], where two light pulses with matched slow group velocities interact strongly, has generated much interest over the last decade [110, 100, 86, 2, 154]. The fidelity of the double-EIT scheme as a phase shifter has been investigated as well [99, 116]. Also

of interest in weak light interaction is the photonic switching achieved by the absorptive analog of the giant Kerr nonlinearity [52], which has shown much experimental progress [163, 14, 60, 5, 26]. Further related work is listed in Refs. [85, 111, 117, 41, 40, 114, 15].

We propose a cross phase modulation scheme in a refractive index enhanced atomic medium. The phase shifter described here is built around the refractive index enhancement scheme in a far-off resonant atomic system [165, 4], that was discussed in chapter 2. We use a four level system as shown in Fig. 6.1. The system consists of a ground state $|g\rangle$, two excited Raman states $|1\rangle$ and $|2\rangle$, and an excited upper state $|e\rangle$. For simplicity, we take the two Raman states to be degenerate. The system is initially prepared with all atoms pumped into the ground state. We choose the states and the polarization of the laser beams appropriately such that there is no cross coupling, due to angular momentum selection rules. We achieve refractive index enhancement with vanishing absorption by interfering the two Raman resonances. The frequency separation between the two Raman resonance line-centers can be precisely tuned by choosing the frequencies of the two control lasers. The two photon detuning $\delta\omega_1$ ($\delta\omega_2$) corresponds to the amplifying (absorptive) resonance on the probe beam. The degree of interference between the resonances is characterized by how much the resonance curves overlap, which is quantified as $\Delta = \delta\omega_1 + \delta\omega_2$, the size of the separation between the two resonances when scanning the probe frequency.

6.2 Conditional phase shifter via interference

In this chapter, we propose using this refractive index enhancement scheme as a conditional phase shifter simply by adding a switch beam, $\mathcal{E}_s$, to the system. The switch beam is weak and couples the states $|1\rangle$ and $|2\rangle$ to $|e\rangle$ with a one photon detuning of $\delta\omega_s$ as shown in Fig. 6.1. The switch beam interacts with the probe beam by ac stark shifting the energy level of states $|1\rangle$ and $|2\rangle$. This shift of the energy levels effectively changes the two photon detunings, $\delta\omega_1$ and $\delta\omega_2$, of the Raman transitions and affects how strongly the Raman resonances of the probe beam interfere. For the ideal case of equal dipole matrix elements, $d_{1e} = d_{2e}$, the change in the detunings equally shifts the frequency positions of the resonances relative to the probe beam frequency. Therefore, for a probe beam tuned midway between the resonances(i.e. the point of vanishing absorption) the

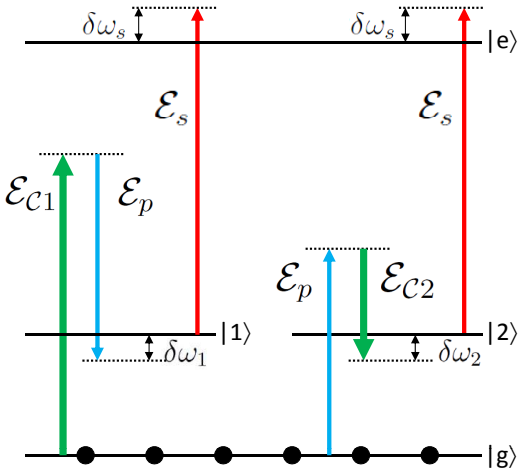

Figure 6.1 The schematic of the proposed scheme. A weak far-off resonant probe beam $\mathcal{E}_p$, and two strong control lasers, $\mathcal{E}_{\mathcal{C}1}$ and $\mathcal{E}_{\mathcal{C}2}$, two photon couple the ground state $|g\rangle$ to the excited Raman states $|1\rangle$ and $|2\rangle$. A weak switch beam $\mathcal{E}_s$ one photon couples the degenerate excited Raman states $|1\rangle$ and $|2\rangle$ to the excited upper state $|e\rangle$. Activation of the switch beam induces a conditional ac stark shift on $|1\rangle$ and $|2\rangle$ which alters the two-photon detunings $\delta\omega_1$ and $\delta\omega_2$ and modifies the propagation of the probe beam.

degree of the interference is modified by the switch beam but probe beam remains tuned midway between the resonances. The key idea behind this suggestion is that when the switch beam is applied, the modified interference of the resonances results in an altered phase accumulation for the probe beam while maintaining vanishing absorption.

We proceed with a detailed discussion of the scheme. When the single photon detunings from the excited state are large, the probability amplitude of the excited state can be adiabatically eliminated. In the perturbative limit where most of the population stays in the the ground state and neglecting power broadening, the steady state nonlinear susceptibility of the probe beam is given by [165]

$$\chi_{\mathcal{E}} = \frac{\hbar N}{\epsilon_0}\left(\frac{|\kappa_1|^2}{\delta\omega_1 + i\gamma_1} + \frac{|\kappa_2|^2}{\delta\omega_2 - i\gamma_2}\right) \quad . \tag{6.1}$$

The strength of the Raman coupling of the states $|1\rangle$ and $|2\rangle$ by the probe and control beams is related to the coupling coefficients

$$\kappa_1 \quad = \quad \frac{d_{ge}d_{1e}\mathcal{E}_{\mathcal{C}1}}{2\hbar^2\left(\omega_e - \omega_1 - \omega_p\right)} \quad ,$$

$$\kappa_2 \quad = \quad \frac{d_{ge} d_{2e} \mathcal{E}_{\mathcal{C}2}}{2\hbar^2 \left(\omega_e - \omega_g - \omega_p\right)} \quad , \qquad [6.2]$$

where the quantities d_{ij} are the relevant dipole matrix elements and γ_1 and γ_2 are the respective (amplitude) decay rates of the excited Raman states $|1\rangle$ and $|2\rangle$. For simplicity, we assume balanced parameters for both the amplifying and absorptive resonances such that $\kappa_1 = \kappa_2$ and $\gamma_1 = \gamma_2$, which we hereby refer to as κ and γ. Fig. 6.2 plots the susceptibility, $\chi_{\mathcal{E}}$, of the probe beam as its frequency, ω_p, is scanned across the Raman resonances. The real part $\chi'_{\mathcal{E}}$ is related to the index of refraction by $n = \sqrt{1 + \chi'_{\mathcal{E}}}$ and the imaginary part $\chi''_{\mathcal{E}}$ corresponds to the gain/absorption. The nonlinear phase accumulation of the probe and power absorption coefficient are given by

$$\begin{aligned} \phi &= \frac{\omega_p}{c} \frac{\chi'_{\mathcal{E}}}{2} l \quad , \\ \alpha &= \frac{\omega_p}{c} \chi''_{\mathcal{E}} l \quad , \end{aligned} \qquad [6.3]$$

where l is the medium length. With the condition that

$$\delta\omega_1 = \delta\omega_2 = \Delta/2 \quad , \qquad [6.4]$$

the probe beam is tuned at the midpoint between the resonances and constructive interference in $\chi'_{\mathcal{E}}$ gives enhanced index of refraction while destructive interference of $\chi''_{\mathcal{E}}$ gives vanishing absorption [165]. Also we note that the group velocity of the probe beam when tuned to vanishing absorption is $v_g \approx c$ because a local extremum of $\chi'_{\mathcal{E}}$, i.e. zero slope, coincides with $\chi''_{\mathcal{E}} = 0$ as seen in Fig. 6.2. As a result, there will not be a group velocity mismatch between the probe beam and an off-resonant switch beam.

The key idea of our phase shifter is to induce a conditional change in the separation of the Raman resonances, Δ, which results in a significant shift in the nonlinear phase accumulated by the probe beam. Comparison of the plots in Fig. 6.2, where $\Delta = 10\gamma, 5\gamma, \gamma, -\gamma$ respectively, shows there is a strong dependence of the refractive index on Δ. When the probe beam is tuned at the point for vanishing absorption, we apply the condition of Eq. (6.4) to Eq. (6.1) and use Eqs. (6.3) to express the phase accumulation as a function of the separation of the resonances, given by

$$\phi = \frac{\hbar\omega_p \left|\kappa\right|^2 N l}{c\epsilon_0} \frac{\frac{\Delta}{2}}{\gamma^2 + \left(\frac{\Delta}{2}\right)^2} \quad , \qquad [6.5]$$

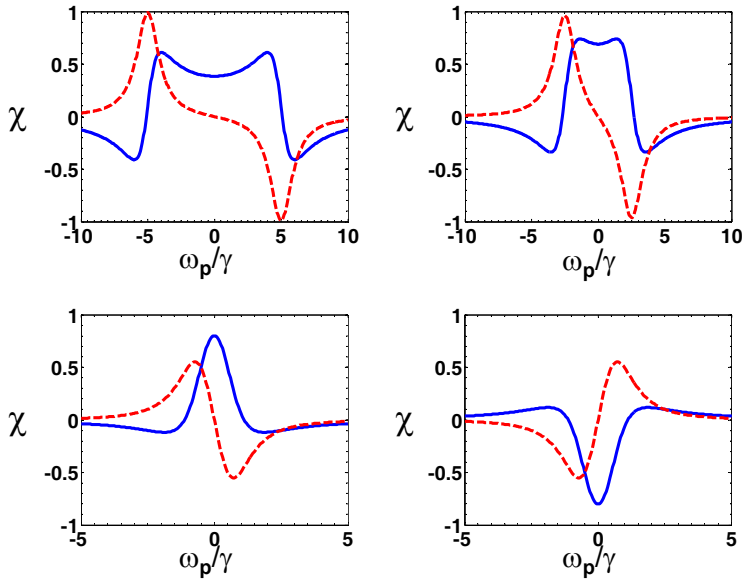

Figure 6.2 The real part $\chi'_{\mathcal{E}}$ (blue solid line) and the imaginary part $\chi''_{\mathcal{E}}$ (red dashed line) of the nonlinear susceptibility as a function of the probe beam frequency. Between the plots the separation of the resonances is varied to the respective values $\Delta = 10\gamma, 5\gamma, \gamma, -\gamma$. Note that the sign of $\chi'_{\mathcal{E}}$ changes accordingly when the sign of Δ changes.

and is plotted in Fig. 6.3. The largest phase accumulation occurs at $\Delta = \pm 2\gamma$ and has the value $\phi_{max} = \frac{\hbar\omega_p|\kappa|^2 Nl}{2\gamma c\epsilon_0}$. The largest variation of ϕ with respect to Δ occurs at $\Delta = 0$ where the slope is steepest. However in this region, where $|\Delta| \ll \gamma$, the values of ϕ are small because the resonances are closely overlapping causing near complete cancellation of the nonlinear interaction. The most efficient phase shift is achieved by varying Δ around the point $\Delta = 0$, where the steep slope optimally changes the phase accumulation. In the region $|\Delta| \gg \gamma$ the system becomes two isolated resonances and ϕ drops as $1/\Delta$ and the slope approaches zero.

Before we proceed with an analysis of the role of the switch beam, we first discuss how the fidelity of the phase shifter is affected by spontaneously emitted photons. A Heisenberg-Langevin analysis of the refractive index enhancement scheme has been conducted in Ref. [166] and this quantum treatment of the probe beam is consistent with the semiclassical derivation of Eqs. (6.1-6.3). The key result of this analysis is that due to the presence of the amplifying resonance there are spontaneously emitted photons into the probe beam, which we refer to as noise photons. The

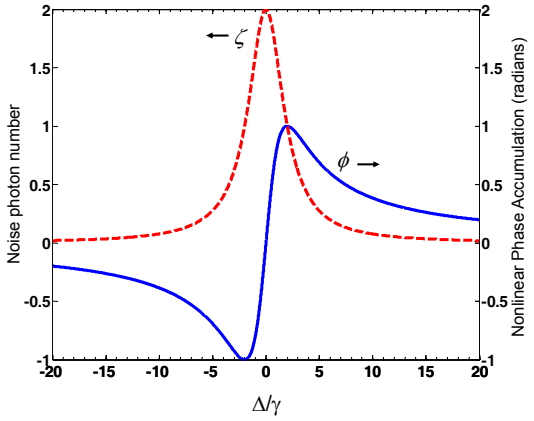

Figure 6.3 The nonlinear phase accumulation ϕ (blue solid line) and the number of spontaneous noise photons ζ (red dashed line) of the probe beam as a function of the separation between the resonances Δ. The peak of the noise curve coincides with the point of steepest variation in the phase accumulation, thus there is a trade-off between the efficiency of the phase shifter and noise emission. The plot is given for the case $\phi_{max} = 1$ radian by choosing the prefactor $\frac{\hbar\omega_p|\kappa|^2 Nl}{c\epsilon_0} = 2\gamma$.

number of noise photons added to the probe beam depends on the gain of the amplifying resonance and is given by

$$\zeta = \frac{\hbar\omega_p \left|\kappa\right|^2 Nl}{c\epsilon_0} \frac{\gamma}{\gamma^2 + \left(\frac{\Delta}{2}\right)^2} \quad , \qquad [6.6]$$

and is plotted as a function of the separation between the resonances Δ in Fig. 6.3. Note that the number of noise photons emitted into the probe beam is greatest when the amplifying and absorptive resonances are closest, in the region $|\Delta| \ll \gamma$. This result is unfortunate because it is ideal to operate the phase shifter in this region, where the slope of the phase accumulation is greatest but the noise added to the probe beam is unacceptably high. Therefore, there is a trade-off in the efficiency of the phase shifter and the noise added to the probe beam.

Next we examine how the presence of a weak switch beam in the scheme effectively shifts the phase of the probe beam. The switch beam ac stark shifts the excited Raman states $|1\rangle$ and $|2\rangle$. For simplicity, we assume equal dipole matrix elements, $d_{1e} = d_{2e}$, and therefore assume equal shift of both states. We define the size of this stark shift in frequency space as $\Delta_s/2$. The energy level shift of the Raman levels modifies the two photon detunings such that $\delta\omega_{1(2)} \rightarrow \delta\omega_{1(2)} + \Delta_s/2$. Thus

the switch beam is the conditional mechanism to change the separation of the Raman resonances such that $\Delta = \Delta_0 \rightarrow \Delta = \Delta_0 + \Delta_s$. Using these two conditional values for Δ, Eqs. (6.5) and (6.6) give the conditional phase shift, $\delta\phi$, and the effective noise photon number, ζ_{eff}:

$$\delta\phi = \frac{\hbar\omega_p |\kappa|^2 Nl}{c\epsilon_0} \left(\frac{\frac{\Delta_0+\Delta_s}{2}}{\gamma^2 + \left(\frac{\Delta_0+\Delta_s}{2}\right)^2} - \frac{\frac{\Delta_0}{2}}{\gamma^2 + \left(\frac{\Delta_0}{2}\right)^2} \right) \quad , \qquad [6.7]$$

$$\zeta_{eff} = \frac{\hbar\omega_p |\kappa|^2 Nl}{c\epsilon_0} \frac{\gamma}{\gamma^2 + \left(\frac{\Delta_{min}}{2}\right)^2} \quad , \qquad [6.8]$$

where $\Delta_{min} = min\{|\Delta_0|, |\Delta_0 + \Delta_s|\}$ is the value when the resonances are closest together, giving an upper bound on the noise photon number.

6.3 Performance of phase shifter

To consider the performance of our scheme we define a figure of merit for the effectiveness of the phase shifter: signal-to-noise ratio, $SNR = \delta\phi/\zeta_{eff}$. For ideal use of the phase shifter in information applications we desire a large phase change with as few noise photons as possible. For quantum information operations, an effective phase shifter requires a lower bound of $SNR = \pi$, where there is a π radian phase shift and a single noise photon. The efficiency of the phase shifter is also described in terms of the switch beam intensity, which we desire to minimize. In the ideal limit that a single switch beam photon could achieve a phase shift with $SNR = \pi$, the scheme could potentially be used to implement a quantum phase gate.

The SNR depends critically on the initial choice for the separation of the Raman resonances and the intensity of the switch beam because both $\delta\phi$ and ζ_{eff} are functions of the variables Δ_0 and Δ_s. The value Δ_0 can be set by appropriately choosing the frequencies of the control lasers. The shift in the separation of the resonances due to the switch beam, Δ_s, in the limit that $\delta\omega_s \gg \Gamma_e$ (where Γ_e is the (amplitude) decay rate of the the excited upper state $|e\rangle$), is given by

$$\Delta_s = \frac{\Omega_s^2}{2\delta\omega_s} \quad , \qquad [6.9]$$

where $\Omega_s = d_{1e}\mathcal{E}_s/\hbar$ is the Rabi frequency of the switch beam. We note that if we considered the complex detuning of the switch beam, $\delta\omega_s \rightarrow \delta\omega_s - i\Gamma_e$, the presence of the switch beam would

cause nonlinear absorption due to power broadening of the Raman states, $\gamma \rightarrow \gamma + \frac{\Omega_s^2 \Gamma_e}{4\delta\omega_s^2}$. However, the equally modified resonances will continue to destructively interfere, just as the original resonances did before, resulting in complete cancellation of nonlinear absorption of the probe beam. Power broadening will modify Eqs. (6.7) and (6.8) through the modified decay rate, γ. In this paper, for simplicity, we will focus our attention to the limit $\delta\omega_s \gg \Gamma_e$ such that power broadening is negligible. Using the Wigner-Weisskopf result [162], $d_{1e}^2 = \frac{3\pi\epsilon_0\hbar c^3\Gamma_e}{\omega_{1e}^3}$, the conditional change in the separation of the resonances can be reduced to

$$\Delta_s = n_s \left(\frac{3}{4\pi}\right)\left(\frac{\lambda_s^2}{A}\right)\left(\frac{\Gamma_e}{\delta\omega_s}\right)\left(\frac{1}{\tau}\right) \quad , \qquad [6.10]$$

where n_s is the number of switch beam photons, τ is the switch pulse duration and A is the cross sectional area of the switch beam. In the remainder of this paper, we will take ideal quantities for these parameters, $A = \frac{\lambda_s^2}{2\pi}$ (atomic cross section) and $\tau = 1/\gamma$ and assume $\delta\omega_s = 10\Gamma_e$. With these assumptions, Eq. (6.10) reduces to

$$\Delta_s = \xi\gamma n_s \quad , \qquad [6.11]$$

where we have the numerical factor $\xi = 0.15$.

As was mentioned before, the SNR depends critically on the initial choice for the separation of the two resonances. As we will show later, for a given number of switch photons, the SNR is optimized with respect to Δ_0 under the condition

$$\Delta_0 = -\frac{1}{2}\xi\gamma n_s \quad . \qquad [6.12]$$

Using Eqs. (6.11) and (6.12), the Eqs. (6.7) and (6.8) reduce to:

$$\delta\phi = \frac{\hbar\omega_p |\kappa|^2 Nl}{2\gamma c\epsilon_0} \frac{\xi n_s}{1 + \left(\frac{\xi n_s}{4}\right)^2} \quad , \qquad [6.13]$$

$$\zeta_{eff} = \frac{\hbar\omega_p |\kappa|^2 Nl}{2\gamma c\epsilon_0} \frac{2}{1 + \left(\frac{\xi n_s}{4}\right)^2} \quad , \qquad [6.14]$$

$$SNR = \frac{\xi n_s}{2} \quad . \qquad [6.15]$$

The SNR depends linearly on the size of the stark shift as seen in Fig. 6.4. For an effective phase shifter the lower bound is $SNR = \pi$, where there is a π radian phase shift and a single noise

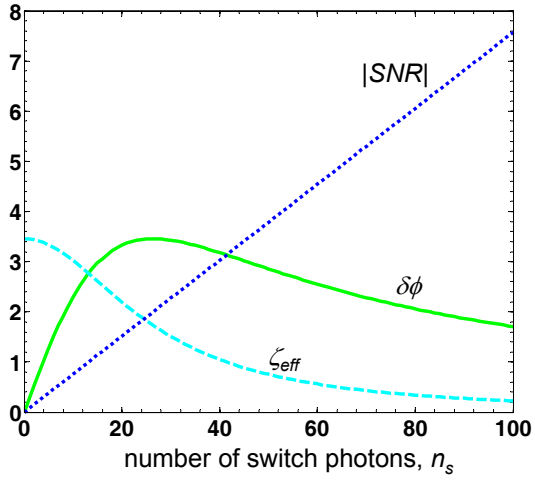

Figure 6.4 The phase shift $\delta\phi$ (green solid line), the effective noise ζ_{eff} (cyan dashed line), and the absolute value of the Signal-to-Noise ratio $|SNR|$ (blue dotted line) as functions of the number of photons in the switch beam, n_s, with the initial separation of the resonance optimally set to $\Delta_0 = -\frac{1}{2}\xi\gamma n_s$. The numerical factor is $\xi = 0.15$ for the switch beam parameters $\delta\omega_s = 10\Gamma_e$, $A = \lambda^2/2\pi$, and $\tau = 1/\gamma$. The plot is given for the case $\delta\phi = \pi$ radians when $|SNR| = \pi$ by choosing the prefactor $\frac{\hbar\omega_p|\kappa|^2 Nl}{2\gamma c\epsilon_0} = 0.55\pi$.

photon. The value of SNR can be increased beyond this lower bound by sufficiently increasing the value of the stark shift. For a single switch beam photon, $n_s = 1$, $SNR = 0.075$. A $SNR = \pi$ is obtained for $n_s = 42$ photons in the switch beam. Unfortunately, these results show that our scheme can not be used as an effective phase shifter at the single photon level in free space.

Finally, we show how we derived the optimization condition on the initial separation of the resonances Δ_0, given by Eq. (6.12), to maximize the SNR for a given set of switch beam parameters. We analytically optimized the SNR with respect to Δ_0, treating Δ_s as a constant. This resulted in the condition $\Delta_0 + \Delta_s = -\Delta_0$ to maximize the SNR. This condition physically corresponds to a configuration where the noise of the shifted case equals the noise of the unshifted case. This dependence of the optimal value of Δ_0 on Δ_s can also be seen in the plots in Fig. 6.5, which show the phase shift, effective noise, and $|SNR|$ as functions of the initial separation between the resonances Δ_0 for various values of $\Delta_s = 1.5\gamma, 6\gamma, 12\gamma$. The top axis of each of the plots is normalized to its respective value of Δ_s. The general result seen is that for a given value Δ_s the

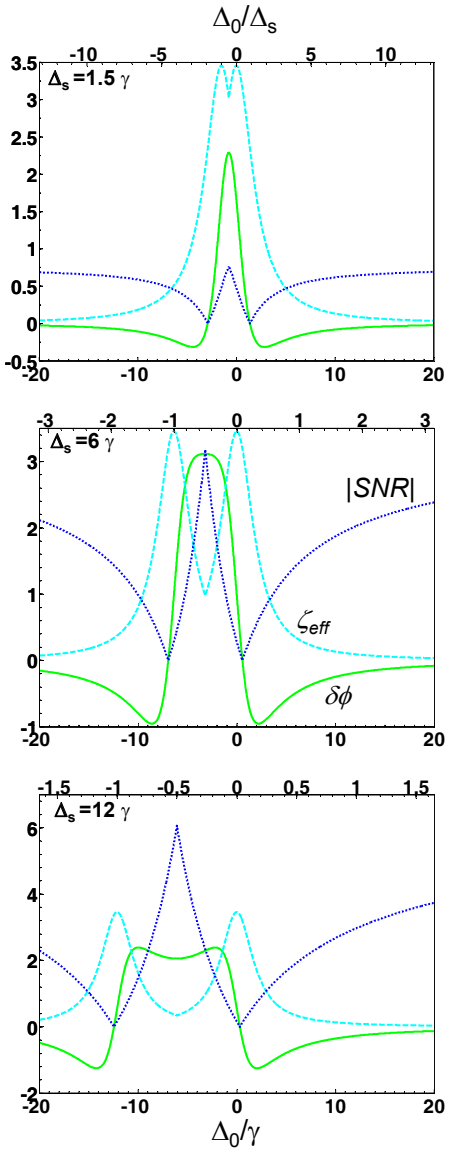

Figure 6.5 The phase shift $\delta\phi$ (green solid line), the effective noise ζ_{eff} (cyan dashed line), and the absolute value of the Signal-to-Noise ratio $|SNR|$ (blue dotted line) as functions of the initial separation of the resonances Δ_0. Between the plots the value of the conditional change in the separation of the resonances Δ_s is varied to $1.5\gamma, 6\gamma,$ and 12γ respectively. The bottom axis expresses Δ_0 in terms of system constant γ, the Raman transition linewidth. The top axis expresses Δ_0 in terms of system variable Δ_s. The key result seen here is that $|SNR|$ is optimized when $\Delta_0 = -\Delta_s/2$.

maximum $|SNR|$ occurs at $\Delta_0 = -\Delta_s/2$. Also in the limit that $\Delta_0 = \pm\infty$ the $|SNR|$ asymptotically approaches this maximum value. In the regime that $\Delta_0 = \pm\infty$ the nonlinear response of the atomic medium is greatly reduced and would require greater resources for achieving the phase shift. Thus, the key result of Fig. 6.5 is that the initial system configuration of $\Delta_0 = -\Delta_s/2$ yields the highest signal-to-noise ratio. However, we do note that when the condition $\delta\omega_s \gg \Gamma_e$ is not satisfied, power broadening of Raman linewidth γ in the shifted case must be included and a more general expression for the optimal value of Δ_0 will depend on Δ_s and the ratio of the excited state linewidth and the switch beam detuning $\Gamma_e/\delta\omega_s$.

6.4 Results for a model atomic system

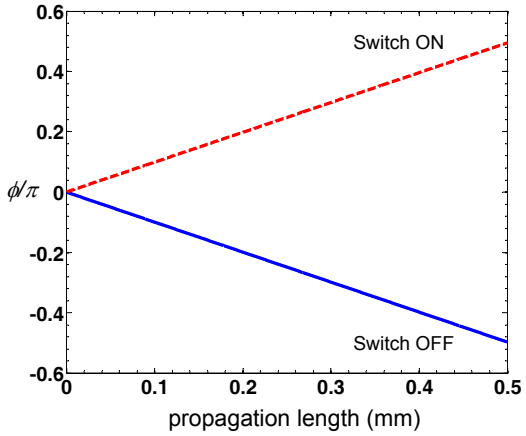

Figure 6.6 The phase accumulation ϕ for the probe beam of the unshifted case (blue solid line) and the shifted case (red dashed line) as a function of the propagation length of the probe beam in the medium.

The plot in Fig. 6.6 shows a numerical example of our phase shifter in a real system based on the analytical steady states solutions of Ref. [165] for the enhanced refractive index at vanishing absorption. We simulate the four level system in a medium of ultra-cold ^{87}Rb atoms with density $N = 2 \times 10^{14}$/cm^3 and length $l = 0.5$ mm based on techniques using either cold atom traps (e.g. magneto-optical or dipole traps) or hollow-core optical fibers [93, 136]. The excited electronic state $5P_{1/2}$ ($D1$ line) is used for the state $|e\rangle$ and $|F = 2, m_F = -2\rangle$, $|F = 2, m_F = 2\rangle$,

and $|F = 2, m_F = 0\rangle$ hyperfine states of the electronic ground state $5S_{1/2}$ are used for states $|1\rangle$, $|2\rangle$, and $|g\rangle$ respectively [141]. The excited state decay rate is $\Gamma_e = 2\pi \times 5.75$ MHz and we assume a Raman line width of $\gamma = 2\pi \times 10$ kHz. The probe, switch, and control beams have polarizations σ^+, π, and σ^- respectively and wavelengths ≈795 nm. The probe beam is red-detuned from the excited state by 10 GHz. The power of the control beams are ≈75 mW and are focused to a beam diameter ≈1 mm. To satisfy the condition that $SNR = \pi$, we set $n_s = 42$ photons per atomic cross section based on the results of Fig. 6.4. The plots in Fig. 6.6 show the accumulated phase of the probe beam as a function of the propagation length for both cases when the switch beam is present and absent. Note that the phase accumulation of the two cases are symmetric about $\phi = 0$ which follows from Eqs. (6.12) and (6.13) that $\Delta = \frac{1}{2}\xi\gamma n_s$ and $\Delta = -\frac{1}{2}\xi\gamma n_s$ when the switch beam is present or absent respectively. These opposite sign phase accumulations achieve a net phase difference of $\approx \pi$ radians at a propagation length of 0.5 mm.

In summary we have developed a scheme for a low intensity phase shifter and estimated its fidelity. The lower bound energy cost for a π radian phase shift with acceptable fidelity is on the order of tens of photons. There is an inherent trade-off where fidelity can be increased at the expense of energy cost of the switch beam. We believe our phase shifter is ideally suited for use in high fidelity optical information processing of weak beams of $10^2 - 10^3$ photons corresponding to an energy of $\approx 0.01 - 0.1$ fJ, where the constraints on beam focusing and pulse duration can be relaxed to more practical values.

Chapter 7

Giant Kerr nonlinearities using refractive index enhancement

7.1 Introduction and background

Over the last decade, there has been a growing interest in techniques that achieve significant nonlinear interactions at the single photon level [20]. These schemes are exciting and important because of both practical and fundamental reasons. Key practical applications include all-optical switches that can operate at an energy cost of a single photon [26] and two-qubit quantum gates between two single photons [94]. Some of the most promising approaches for achieving significant nonlinear interactions at the single photon level utilize the technique of Electromagnetically Induced Transparency (EIT). Various schemes for single photon switches and gates using EIT have been proposed [52, 82, 153] and demonstrated in low-photon regimes [169, 5]. Recently, single photon nonlinearities have been considered in ultra cold gases of Rydberg atoms [112, 30].

In this chapter, we suggest an alternative approach to achieve significant nonlinear interactions between single photons. Our approach uses refractive index enhancement with vanishing absorption to achieve a giant Kerr nonlinearity between two weak laser beams. Before proceeding with a detailed description we would like to summarize the key achievement of this chapter. For simplicity in this chapter, we assume the medium is non-magnetic($\mu = 1$) and drop the subscript $\mathcal{E}$ from the electric susceptibility terms. Let's first consider a laser beam interacting with an ensemble of two level atoms. For this simple case, the third order nonlinear susceptibility of the medium is proportional to $\chi^{(3)} \sim \frac{1}{|\delta - j\Gamma|^2(\delta - j\Gamma)}$ where Γ is the (amplitude) decay rate of the excited state and δ is the detuning of the laser beam from the transition [13]. This third order susceptibility is responsible for well-known effects such as intensity-dependent refractive index and optical self-focusing.

Now consider two off-resonant beams that are very largely detuned from the excited electronic state interacting with a three level atomic system in a Λ configuration. If frequency difference of the two beams is close to the frequency of the Raman transition, the third order susceptibility is enhanced and is proportional to $\chi^{(3)} \sim \frac{1}{|\delta - j\Gamma|^2(\delta\omega - j\gamma)}$. Here γ is the decay rate of the Raman transition and $\delta\omega$ is the two photon detuning. Typically, to reduce nonlinear absorption, one chooses $\delta\omega >> \gamma$ such that the imaginary part of the susceptibility is much smaller than the real part $Im(\chi^{(3)}) << Re(\chi^{(3)})$. The key achievement of our scheme is to obtain a purely real third order nonlinear susceptibility of $\chi^{(3)} \sim \frac{1}{|\delta - j\Gamma|^2\gamma}$ due to destructive interference in the imaginary part. With the decay rate of the Raman transition to be negligible, $\gamma \approx 0$, one can therefore obtain an arbitrarily large value for $\chi^{(3)}$ and obtain significant nonlinear interactions between weak beams. The key advantage of our scheme over EIT is that it does not require a strong coupling laser beam. The key disadvantage is that single-photon linear absorption of the beams is not eliminated. As we will see, this drawback will limit the minimum energy required to be on the order of tens of photons per atomic cross section.

7.2 Giant Kerr effect via interference

Figure 7.1 shows the energy level diagram of our suggestion. The scheme relies on recently-suggested refractive index enhancement with vanishing absorption that utilizes the interference of two Raman transitions [165, 113]. Although the scheme is general, for concreteness, we will focus on a real system and consider ^{87}Rb D1 line transition with the level structure shown in Fig. 7.1. We choose the ground state of the system to be $|g\rangle \rightarrow |F = 2, m_F = 0\rangle$ and the two excited Raman states to be $|1\rangle \rightarrow |F = 2, m_F = -2\rangle$, and $|2\rangle \rightarrow |F = 2, m_F = 2\rangle$. Two off-resonant beams, termed the probe and control beams, couple the ground state $|g\rangle$ to excited Raman states $|1\rangle$ and $|2\rangle$. The two beams have opposite circular polarizations (σ^+ for $\mathcal{E}_p$ and σ^- for $\mathcal{E}_\mathcal{C}$). The quantities $\delta\omega_1$ and $\delta\omega_2$ are two photon detunings of the laser beams from each Raman transition respectively and they are defined as $\delta\omega_1 = (\omega_1 - \omega_g) - (\omega_p - \omega_\mathcal{C})$, $\delta\omega_2 = (\omega_2 - \omega_g) - (\omega_\mathcal{C} - \omega_p)$. The refractive index enhancement scheme as originally suggested requires two separate control laser beams whose frequencies can be tuned to control the position of the two resonances independently.

In the scheme of Fig. 7.1, however, there is only one control laser. The position of the Raman resonances can be controlled by shifting the hyperfine levels through a combination of a Stark shift and Zeeman shift. The Zeeman shift can simply be provided with a magnetic field pointing along the propagation direction of the laser beams. The Stark shift can either be provided with a DC electric field or a separate detuned laser beam. We define the quantity $\Delta \equiv \delta\omega_1 + \delta\omega_2$ to represent the separation of the two Raman resonances as the probe (or the control) laser frequency is scanned.

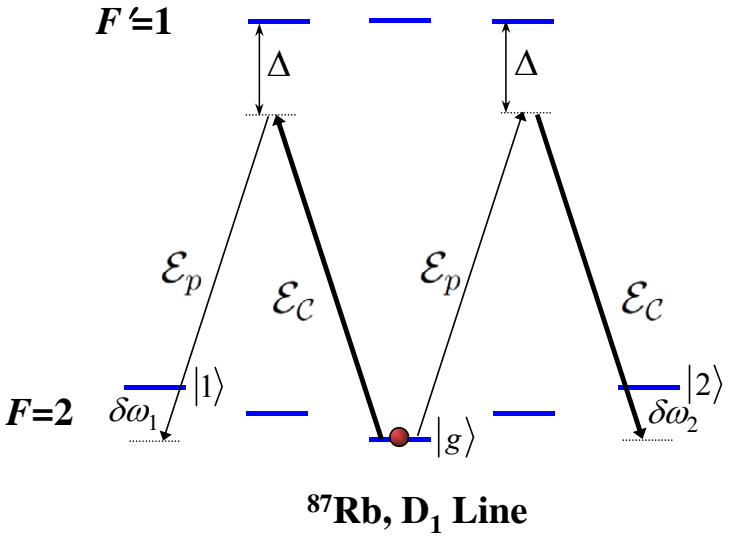

Figure 7.1 The proposed scheme. For concreteness, we focus on a real atomic system and consider two off-resonant laser beams, $\mathcal{E}_p$ and $\mathcal{E}_C$ interacting with ^{87}Rb atoms through the D1 line. The two laser beams are opposite circularly polarized and couple the ground state $|F = 2, m_F = 0\rangle$ to two excited Raman states $|F = 2, m_F = -2\rangle$ and $|F = 2, m_F = 2\rangle$. The quantities $\delta\omega_1$ and $\delta\omega_2$ are two photon detunings of the laser beams from each Raman transition respectively. The positions of the Raman resonances as the probe laser frequency is scanned can be independently controlled by a combination of Zeeman and Stark shift of the hyperfine states.

We proceed with an analysis of the scheme of Fig. 7.1. With δ to be much larger than the decay width Γ, we can adiabatically eliminate the probability amplitudes of the excited states. We also take the two beams to be weak enough such that the power broadening of the Raman transitions can be ignored. With these assumptions, the polarization of the medium at the two laser frequencies

can be written as [165]:

$$P_p = \epsilon_0 \chi^{(1)} \mathcal{E}_p + \epsilon_0 \chi^{(3)} |\mathcal{E}_\mathcal{C}|^2 \mathcal{E}_p \quad ,$$
$$P_\mathcal{C} = \epsilon_0 \chi^{(1)} \mathcal{E}_\mathcal{C} + \epsilon_0 \chi^{(3)^*} |\mathcal{E}_p|^2 \mathcal{E}_\mathcal{C} \quad , \qquad [7.1]$$

where $\chi^{(1)}$ and $\chi^{(3)}$ are the linear and the nonlinear third-order susceptibilities of the medium respectively. These quantities are [165]:

$$\chi^{(1)} = \frac{N}{\epsilon_0 \hbar} \frac{|d_{ij}|^2}{\delta - j\Gamma} \quad ,$$
$$\chi^{(3)} = \frac{N}{4\epsilon_0 \hbar^3} \frac{1}{|\delta - j\Gamma|^2} \left(\frac{|d_{ij}|^2 |d_{jk}|^2}{\delta\omega_1 - j\gamma_1} + \frac{|d_{il}|^2 |d_{lm}|^2}{\delta\omega_2 + j\gamma_2} \right) \quad . \qquad [7.2]$$

Here, N is the atomic density, d_{ij} are the dipole matrix elements between relevant states, Γ is the decay rate of the excited state, and γ_1 and γ_2 are dephasing rates of the Raman transitions respectively. As expected, the third order nonlinear susceptibility is a sum of two terms due to two Raman transitions. It is the interference of these two terms that result in the enhancement of the real part while resulting in the vanishing imaginary part. Figure 7.2 shows the real (solid line) and the imaginary (dashed line) parts of $\chi^{(3)}$ as the probe laser frequency is scanned for three different values of the separation of Raman resonances, $\Delta = 10\gamma$, 5γ, and γ respectively. Here, for simplicity, we assume the two Raman transitions to have the same parameters including an identical Raman linewidth of $\gamma_1 = \gamma_2 \equiv \gamma$. At the mid-point between the two resonances, $\delta\omega_1 = \delta\omega_2$, the imaginary part vanishes while the real part is enhanced due to constructive interference.

At the point of vanishing imaginary part, the third order nonlinear susceptibility is purely real and is given by:

$$\chi^{(3)} = \frac{N}{2\epsilon_0 \hbar^3} \frac{|d_{ij}|^2 |d_{jk}|^2}{|\delta - j\Gamma|^2} \frac{\Delta/2}{(\Delta/2)^2 + \gamma^2} \quad . \qquad [7.3]$$

While deriving Eq. (7.3), for simplicity, we have again assumed the two Raman resonances to have identical parameters. From Eq. (7.3), we note that the value of the nonlinear susceptibility strongly depends on the separation of the two Raman resonances, Δ. The maximum nonlinear susceptibility is obtained when $\Delta = 2\gamma$ and is given by,

$$\chi^{(3)}_{max} = \frac{N}{4\epsilon_0 \hbar^3} \frac{|d_{ij}|^2 |d_{jk}|^2}{|\delta - j\Gamma|^2} \frac{1}{\gamma} \quad . \qquad [7.4]$$

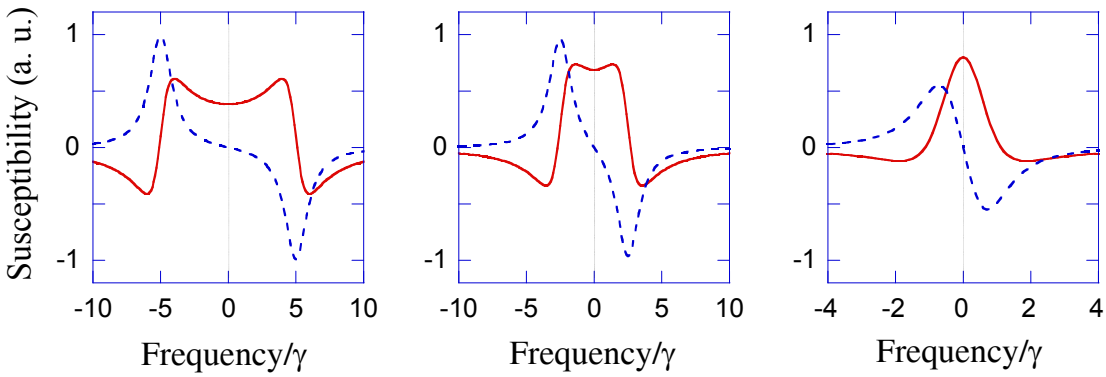

Figure 7.2 The real (solid line) and imaginary (dashed line) parts of the nonlinear susceptibility as a function of probe laser frequency for three different values of the separation of two Raman resonances, $\Delta = 10\gamma$, 5γ, and γ. At the mid-point between the two resonances, the real part is enhanced due to constructive interference whereas the imaginary part vanishes due to destructive interference.

Eq. (7.4) is the central result of this chapter. The nonlinear susceptibility is purely real and in the limit of very long dephasing and decay time of the Raman transitions ($\gamma \approx 0$), it can become arbitrarily large.

From the nonlinear susceptibility of Eq. (7.4), we can also find the expression for the intensity dependent refractive index, $n_2 = \eta\chi^{(3)}$ where $\eta = \sqrt{\mu_0/\epsilon_0}$. Before proceeding further, we evaluate the intensity dependent refractive index for experimentally achievable parameters. We consider an ultracold ^{87}Rb atomic cloud with $N = 10^{14}$ atoms/cm^3. We take $\delta = 10\Gamma$ where Γ is the decay rate of $5P_{1/2}$, $2\Gamma = 2\pi \times 5.74$ MHz. We assume a Raman transition linewidth of $\gamma = 2\pi \times 10$ kHz. With these modest parameters, we calculate an intensity dependent refractive index of $n_2 = 75.8$ cm^2/Watt, which is comparable to what has been achieved in recent EIT experiments.

We proceed with the evaluation of the nonlinear phase shift of the probe laser due to few-photon control laser pulses. For this purpose, we consider a control laser beam pulse of Gaussian temporal shape that contains n_c photons. By using Eqs. (7.1-7.4) it can be derived that the nonlinear phase accumulation of the probe laser beam and the corresponding linear power absorption coefficient

are (for the specific scheme of Fig. 7.1):

$$\begin{aligned} \phi_{non-linear} &= \frac{3}{32\sqrt{\pi}} n_{\mathcal{C}} (N\sigma L) \frac{\Gamma^2}{\delta^2+\Gamma^2} \frac{\sigma}{A} \frac{1}{\gamma\tau} \quad , \\ \alpha_{linear} &= \frac{1}{4}(N\sigma L) \frac{\Gamma^2}{\delta^2+\Gamma^2} \quad . \end{aligned} \qquad [7.5]$$

Here $\sigma = \lambda^2/2\pi$ is the atomic cross section, A is the transverse area of the beam and τ is the temporal Gaussian width of the pulse. While deriving Eq. (7.5), we have assumed that the excited states are purely lifetime broadened and neglected non-radiative broadening effects such as collisions. As expected, Eq. (7.5) shows that the nonlinear phase accumulation is intrinsically related to the linear loss. If we assume the ideal case of $\tau \approx 1/\gamma$ and consider tightly focused beams, $A \approx \sigma$, Eq. (7.5) reduces to:

$$\phi_{non-linear} = \frac{3}{8\sqrt{\pi}} n_{\mathcal{C}} \alpha_{linear} \quad . \qquad [7.6]$$

From Eq. (7.6), if we limit the linear power loss to 50 % ($\alpha_{linear} = 0.7$), a single control photon ($n_{\mathcal{C}} = 1$) per atomic cross-section causes a nonlinear phase shift of 0.15 radians. A nonlinear phase shift of π radians would therefore require about 21 control laser photons per atomic cross section.

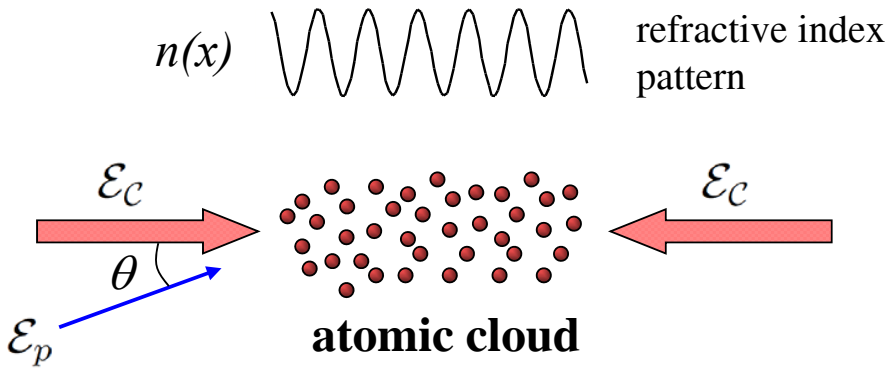

Figure 7.3 The setup for constructing an all-optical mirror. The counter-propagating control lasers form a standing wave pattern which results in a periodic variation of the refractive index. As a result, a photonic band-gap is formed for the probe laser beam and the probe wave is reflected off the medium.

7.3 All-optical mirror

We next discuss a type of optically-controlled optical device using our scheme [33]. Due to the intensity dependent refractive index, an intensity pattern on the control laser will produce a refractive index pattern for the probe laser beam. By using an appropriate intensity pattern, one can, therefore, engineer an all-optical device. Figure 7.3 shows a simple scheme where we consider an ultracold atomic cloud interacting with a probe and a counter-propagating pair of control laser beams. Due to the standing wave intensity pattern of the control laser, the probe wave experiences a periodic variation of the refractive index. Under these conditions, within a certain frequency range, a photonic band-gap is produced and the propagation of the probe wave is forbidden inside the medium. Within the photonic band-gap, the incident probe laser can not penetrate the medium and is reflected. The idea of utilizing a periodic variation of the refractive index was motivated by the recent work of Lukin and colleagues who proposed and experimentally demonstrated optically induced photonic band-gaps using EIT and slow light [3, 6].

To calculate the reflectivity of such a medium, we use the coupled mode theory of Yariv and Yeh [164]. Figure 7.4 shows the results of a calculation for an ultracold ^{87}Rb cloud. Here, we choose the medium parameters and the control laser intensity such that the nonlinear index enhancement is $n_2 I_{\mathcal{C}}^{max}$=$10^{-3}$. Due to the standing wave pattern, the refractive index varies between $n = 1$ and $n = 1 + 10^{-3}$ with a period of $\lambda_{\mathcal{C}}/2 \approx 397$ nm. We take the atomic cloud to be sufficiently cold (temperature of about 1 μK) such that two-photon Doppler broadening of the Raman transitions can be ignored. This assumption simplifies the problem considerably since probe beam interacts with both control lasers in the same way. Figure 7.4(a) shows the power reflection coefficient, R, for the probe wave as a function of the length of the medium, L. Here, we take the probe wave propagation direction to coincide with one of the control lasers ($\theta = 0$). For $L = 1.5$ mm, the reflection coefficient exceeds 99 %. Figure 7.4(b) shows the reflection coefficient as a function of the angle of incidence, θ, for a medium length of $L = 1$ mm. The angle of incidence, θ, is defined as the angle between the probe beam and one of the control lasers as shown in Fig. 7.3. The reflection coefficient remains high for about 1.5 degrees and then drops sharply. For $L = 1$ mm, if we set

the medium parameters such that there is 50 % power loss due to linear absorption ($\alpha_{linear} = 0.7$), then the results of Fig. 7.4 require about $n_{\mathcal{C}} = 13$ control laser photons (in each beam) per atomic cross section.

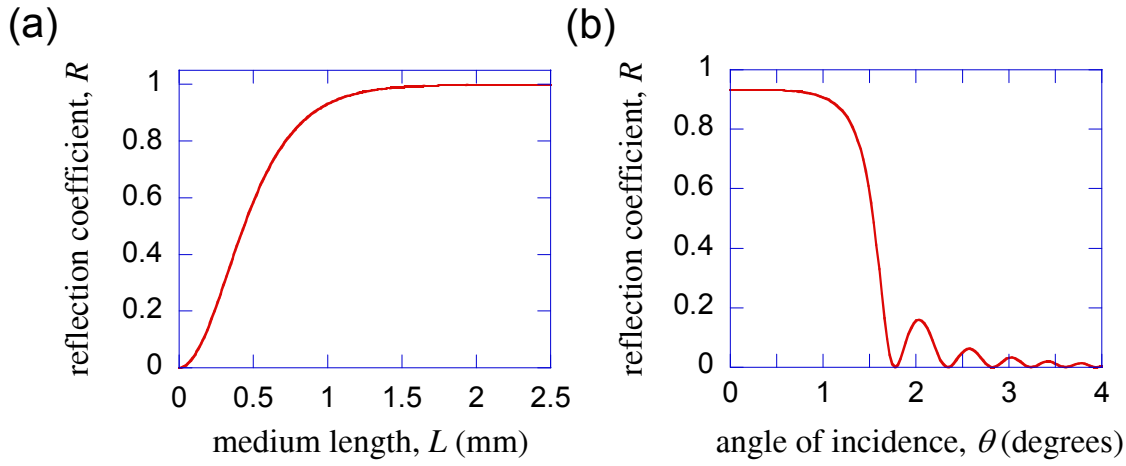

Figure 7.4 (a) The reflection coefficient for the probe wave, R, as a function of the length of the index-enhanced medium, L, for $n_2 I_{\mathcal{C}}$=10^{-3} and $\theta = 0$. The reflection coefficient exceeds 99% for $L = 1.5$ mm. (b) The reflection coefficient as a function of the angle of incidence, θ. The angle of incidence, θ, is defined as the angle between the probe beam and one of the control lasers as shown in Fig. 7.3. For $L = 1$ mm, if we set the medium parameters such that there is 50 % power loss due to linear absorption ($\alpha_{linear} = 0.7$), then these results require about $n_{\mathcal{C}} = 13$ control laser photons (in each beam) per atomic cross section.

Before concluding, we would like to draw attention to the recent work of Shapiro and colleagues [129, 130] and Gea-Banacloche [43]. By using a multi-mode quantum mechanical treatment, these authors argue the impossibility of achieving large nonlinear phase shifts using single photon wavepackets. The key reason is the loss of fidelity due to spontaneous emission. Their results suggest that achieving large nonlinear phase shifts with reliable fidelity will require beam energies at least at the tens of photons level, independent of the specific scheme that is used.

7.4 Conclusions

In conclusion, we have suggested a new approach for achieving a large nonlinear Kerr effect between two weak laser beams while maintaining vanishing nonlinear absorption. Differing from

EIT, the linear absorption of the beams is not eliminated and as a result, high nonlinear phase shifts require beam energies at the level of tens of photons per atomic cross section. The key advantage over EIT is that there is no strong coupling laser and as a result the total energy requirement is at the tens of photons level. We have also suggested a new type of an all optical distributed Bragg reflector that utilizes periodic variation of the refractive index due to a standing wave pattern.

Chapter 8

Conclusions

In this thesis we have described how the index of refraction relates to the interaction of light and matter and how it may be altered in an atomic system by using lasers to manipulate those interactions. Schemes that combine energy level structures with appropriately tuned lasers have been suggested that achieve both negative refractive index and enhanced refraction with vanishing absorption for an incident probe beam. A new approach for a medium with negative refractive index and vanishing absorption is highly desired because it can be utilized in efforts toward near perfect imaging systems, which have the ability to focus evanescent wave components. On the other hand, methods to enhance the refractive index while canceling absorption are also of interest in improving the resolution of conventional imaging systems and for the control of phase accumulation in all-optical information applications.

We have suggested a new scheme for negative refraction that results from laser driven atomic transition resonances rather than the antenna like resonances of metamaterials. We believe an atomic based approach for negative index offers the possibility of achieving negative refraction at optical wavelengths and a way to eliminate absorption by quantum interference techniques. In our suggestion a magnetoelectric cross coupling laser is present in the system and resolves the difficulty of achieving a negative valued permeability by introducing chiral interactions that contribute to the refractive index. An analytical calculation of our scheme predicts negative refraction for a probe beam at a wavelength of $\lambda_p = 500$nm in a model atomic system with a density on the order of 10^{16} cm^{-3} and decay rates on the order of 10 MHz while maintaining low absorption. The results of the analytical predictions are verified by similar results obtained by numerically solving the density-matrix equations of the system.

To our knowledge the negative refraction scheme we have suggested is the most promising in its experimental feasibility. Unlike other suggestions that require an energy level structure possessing electric and magnetic transitions at the same wavelength, our Raman-based approach is flexible, in that we may be far-off resonant from the electric transition. After investigating the structure of the rare-earth atoms we have identified possible candidates for experimental implementation in vapors of Erbium and Dysprosium and crystals doped with ions of Terbium and Praseodymium. Initial experimental goals toward negative refraction will include:

(i) A study of the specific rare-earth spectral lines of interest to the scheme. To our knowledge these have not be investigated in detail before.

(ii) Demonstration of significant magnetoelectric cross coupling interactions that alter the refractive index. A basic form of chirality has already been demonstrated in Rb vapor [120] and chiral interactions should be signification at feasible densities that are lower than the experimentally challenging high densities necessary for negative refraction. By varying the intensity, phase, and detuning of the coupling beam the effects of chiral interactions can be investigated.

(iii) Further studies and improvements of experimental techniques related to the creation of ultracold vapors of rare-earth atomic vapors at high densities and spectral hole burning in cryogenically cooled rare-earth doped crystals. These results will be of considerable interest to the broader EIT, quantum computing, and rare-earth physics communities.

We have also suggested two applications for our refractive index enhancement scheme. These applications make use of the Kerr nonlinearities of the refractive index enhancement to modify the nonlinear phase accumulation of weak probe beam in the medium. A phase shifter can be implemented by the cross phase modulation of two weak light pulses. In this scheme a conditional, weak switching beam alters the interference of the Raman resonances and causes the phase of the probe beam to shift. We predict that a minimum of 42 switch beam photons are required to induce a π radian phase shift on a probe pulse with a fidelity sufficient for all-optical information processing. We have also suggested another phase shift scheme using refractive index enhancement that examines the dependence of the nonlinear phase accumulation on the number of control beam photons and the linear absorption present in the system. In the ideal case of a temporally short

control beam pulse and tight beam focusing, a π radian nonlinear phase shift with 50% linear power loss can be obtained with about 21 control laser photons. Additionally we have suggested how the intensity dependent refractive index can be utilized for an atomic vapor all-optical mirror based on distributed Bragg reflection. For a medium 1 mm thick, a power reflection coefficient exceeding 92% with 50% linear power loss can be achieved by interfering two control beams with 13 photons each, into a standing wave pattern.

These schemes suggested in this thesis provide new insights to approaches to improve imaging systems and optically controling the phase of light. One of the common characteristics of these schemes is that they are based on far-off resonant Raman transitions. The ability of these schemes to operate in a far-off resonant regime suggests that they may be more broadly implemented in a variety of experimental systems that may not suitable for near resonant techniques such as EIT. These off resonant techniques allow the schemes to function over a tunable band of probe light frequencies. In particular the off resonant feature allows us to consider actual atomic species for proposing negative refraction experiments.

DISCARD THIS PAGE

Appendix A: Analytical dynamics of far-detuned Raman system

A.1 Four level system for refractive index enhancement

We begin by expanding the total wave function for the atomic system, $|\psi\rangle$, in the interaction picture

$$|\psi\rangle = c_g e^{-i\omega_g t}|g\rangle + c_1 e^{-i\omega_1 t}|1\rangle + c_2 e^{-i\omega_2 t}|2\rangle + c_e e^{-i\omega_e t}|e\rangle \quad , \qquad \text{[A.1]}$$

where for the respective level, $|i\rangle$, c_i is the complex probability amplitude and $\omega_i = \frac{E_i}{\hbar}$ is the frequency corresponding to the level's energy. The quantum dynamics of the system are solved for by using the Schrödinger equation,

$$i\hbar\frac{\partial|\psi\rangle}{\partial t} = \left(\hat{H}_0 + \hat{H}_{int}\right)|\psi\rangle \quad . \qquad \text{[A.2]}$$

The operator $\hat{H}_0$ is the unperturbed Hamiltonian and $\hat{H}_{int}$ is the interaction Hamiltonian that includes the interactions of the atom with the electric field components of the incident light waves. These operators are given by,

$$\begin{aligned} \hat{H}_0 &= \hbar\omega_g|g\rangle\langle g| + \hbar\omega_1|1\rangle\langle 1| + \hbar\omega_2|2\rangle\langle 2| + \hbar\omega_e|e\rangle\langle e| \quad , \\ \hat{H}_{int} &= -\mathcal{E}\hat{d} = -\mathcal{E}\left(d_{ge}|g\rangle\langle e| + d_{1e}|1\rangle\langle e| + d_{2e}|2\rangle\langle e| + h.c.\right) \quad , \end{aligned} \qquad \text{[A.3]}$$

The quantities d_{ij} are the electric dipole transition matrix elements between the respective levels and $h.c.$ refers to the hermitian conjugate. $\mathcal{E}$ refers to the total electric field which includes frequency contributions from all of the relevant lasers. The total electric field can be found by taking the real part of the Fourier expansion of relevant frequencies,

$$\begin{aligned} \mathcal{E}(t) &= Re\left[\sum_n \mathcal{E}_n e^{-i\omega_n t}\right] = \sum_n \frac{1}{2}\left(\mathcal{E}_n e^{-i\omega_n t} + \mathcal{E}_n^* e^{i\omega_n t}\right) \\ &= \frac{1}{2}\left(\mathcal{E}_p e^{-i\omega_p t} + \mathcal{E}_{\mathcal{C}1} e^{-i\omega_{\mathcal{C}1} t} + \mathcal{E}_{\mathcal{C}2} e^{-i\omega_{\mathcal{C}2} t} + h.c.\right) \quad , \end{aligned} \qquad \text{[A.4]}$$

where $\mathcal{E}_n$ is the electric field amplitude of the Fourier component oscillating at frequency ω_n.

We proceed by using Schrödinger's equation, Eq. (A.2), with Hamiltonian of Eq. (A.3) to solve for the time evolution of the probability amplitudes:

$$\begin{aligned}
\dot{c}_g &= \frac{i}{\hbar}\left[d_{ge}\mathcal{E}c_e e^{i(\omega_g-\omega_e)t}\right] \quad , \\
\dot{c}_1 &= \frac{i}{\hbar}\left[d_{1e}\mathcal{E}c_e e^{i(\omega_1-\omega_e)t}\right] - \gamma_1 c_1 \quad , \\
\dot{c}_2 &= \frac{i}{\hbar}\left[d_{2e}\mathcal{E}c_e e^{i(\omega_2-\omega_e)t}\right] - \gamma_2 c_2 \quad , \\
\dot{c}_e &= \frac{i}{\hbar}\left[d^*_{ge}\mathcal{E}c_g e^{i(\omega_e-\omega_g)t} + d^*_{1e}\mathcal{E}c_1 e^{i(\omega_e-\omega_1)t} + d^*_{2e}\mathcal{E}c_2 e^{i(\omega_e-\omega_2)t}\right] - \Gamma_e c_e \quad . \qquad \text{[A.5]}
\end{aligned}$$

We assume a weak probe beam such that the coupling rates of the probe beam are sufficiently smaller than the single-photon detunings from the excited electronic state. With this assumption, the lasers are far-off resonance with the excited electronic state and this allows us to adiabatically eliminate its probability amplitude, which simplifies our analysis by reducing the scheme to an effective three level system. Adiabatic elimination of the excited electronic state dynamics is implemented by integrating the rate equation for $\dot{c}_e$ in time but we assume that the time dependent probability amplitudes of the other states c_g, c_1, and c_2 can be treated as constants in the integration. This treatment of the other probability amplitudes as quasi-static constants is valid because the large single-photon detunings from the excited state cause c_e to vary much more rapidly compared to the other probability amplitudes. Before performing the integration of $\dot{c}_e$, we factor in the Fourier expansion of the electric field:

$$\begin{aligned}
\dot{c}_e = \frac{i}{2\hbar}\Bigg\{ & d^*_{ge}c_g \quad \Big[\quad \mathcal{E}_p e^{i(\omega_e-\omega_g-\omega_p)t} + \mathcal{E}_{\mathcal{C}1} e^{i(\omega_e-\omega_g-\omega_{\mathcal{C}1})t} + \mathcal{E}_{\mathcal{C}2} e^{i(\omega_e-\omega_g-\omega_{\mathcal{C}2})t} \\
& \qquad + \quad \mathcal{E}^*_p e^{i(\omega_e-\omega_g+\omega_p)t} + \mathcal{E}^*_{\mathcal{C}1} e^{i(\omega_e-\omega_g+\omega_{\mathcal{C}1})t} + \mathcal{E}^*_{\mathcal{C}2} e^{i(\omega_e-\omega_g+\omega_{\mathcal{C}2})t} \Big] \\
& + d^*_{1e}c_1 \quad \Big[\quad \mathcal{E}_p e^{i(\omega_e-\omega_1-\omega_p)t} + \mathcal{E}_{\mathcal{C}1} e^{i(\omega_e-\omega_1-\omega_{\mathcal{C}1})t} + \mathcal{E}_{\mathcal{C}2} e^{i(\omega_e-\omega_1-\omega_{\mathcal{C}2})t} \\
& \qquad + \quad \mathcal{E}^*_p e^{i(\omega_e-\omega_1+\omega_p)t} + \mathcal{E}^*_{\mathcal{C}1} e^{i(\omega_e-\omega_1+\omega_{\mathcal{C}1})t} + \mathcal{E}^*_{\mathcal{C}2} e^{i(\omega_e-\omega_1+\omega_{\mathcal{C}2})t} \Big] \\
& + d^*_{2e}c_2 \quad \Big[\quad \mathcal{E}_p e^{i(\omega_e-\omega_2-\omega_p)t} + \mathcal{E}_{\mathcal{C}1} e^{i(\omega_e-\omega_2-\omega_{\mathcal{C}1})t} + \mathcal{E}_{\mathcal{C}2} e^{i(\omega_e-\omega_2-\omega_{\mathcal{C}2})t} \\
& \qquad + \quad \mathcal{E}^*_p e^{i(\omega_e-\omega_2+\omega_p)t} + \mathcal{E}^*_{\mathcal{C}1} e^{i(\omega_e-\omega_2+\omega_{\mathcal{C}1})t} + \mathcal{E}^*_{\mathcal{C}2} e^{i(\omega_e-\omega_2+\omega_{\mathcal{C}2})t} \Big] \Bigg\} - \Gamma_e c_e . \qquad \text{[A.6]}
\end{aligned}$$

Then integrating this expression with respect to time we solve for the probability amplitude of the excited electronic state:

$$
\begin{aligned}
c_e = \frac{1}{2\hbar}\Bigg\{ d_{ge}^* c_g \Bigg[& \frac{\mathcal{E}_p e^{i(\omega_e-\omega_g-\omega_p)t}}{(\omega_e-\omega_g-\omega_p)-i\Gamma_e} + \frac{\mathcal{E}_p^* e^{i(\omega_e-\omega_g+\omega_p)t}}{(\omega_e-\omega_g+\omega_p)-i\Gamma_e} \\
& \frac{\mathcal{E}_{\mathcal{C}1} e^{i(\omega_e-\omega_g-\omega_{\mathcal{C}1})t}}{(\omega_e-\omega_g-\omega_{\mathcal{C}1})-i\Gamma_e} + \frac{\mathcal{E}_{\mathcal{C}1}^* e^{i(\omega_e-\omega_g+\omega_{\mathcal{C}1})t}}{(\omega_e-\omega_g+\omega_{\mathcal{C}1})-i\Gamma_e} \\
& \frac{\mathcal{E}_{\mathcal{C}2} e^{i(\omega_e-\omega_g-\omega_{\mathcal{C}2})t}}{(\omega_e-\omega_g-\omega_{\mathcal{C}2})-i\Gamma_e} + \frac{\mathcal{E}_{\mathcal{C}2}^* e^{i(\omega_e-\omega_g+\omega_{\mathcal{C}2})t}}{(\omega_e-\omega_g+\omega_{\mathcal{C}2})-i\Gamma_e} \Bigg] \\
+ d_{1e}^* c_1 \Bigg[& \frac{\mathcal{E}_p e^{i(\omega_e-\omega_1-\omega_p)t}}{(\omega_e-\omega_1-\omega_p)-i\Gamma_e} + \frac{\mathcal{E}_p^* e^{i(\omega_e-\omega_1+\omega_p)t}}{(\omega_e-\omega_1+\omega_p)-i\Gamma_e} \\
& \frac{\mathcal{E}_{\mathcal{C}1} e^{i(\omega_e-\omega_1-\omega_{\mathcal{C}1})t}}{(\omega_e-\omega_1-\omega_{\mathcal{C}1})-i\Gamma_e} + \frac{\mathcal{E}_{\mathcal{C}1}^* e^{i(\omega_e-\omega_1+\omega_{\mathcal{C}1})t}}{(\omega_e-\omega_1+\omega_{\mathcal{C}1})-i\Gamma_e} \\
& \frac{\mathcal{E}_{\mathcal{C}2} e^{i(\omega_e-\omega_1-\omega_{\mathcal{C}2})t}}{(\omega_e-\omega_1-\omega_{\mathcal{C}2})-i\Gamma_e} + \frac{\mathcal{E}_{\mathcal{C}2}^* e^{i(\omega_e-\omega_1+\omega_{\mathcal{C}2})t}}{(\omega_e-\omega_1+\omega_{\mathcal{C}2})-i\Gamma_e} \Bigg] \\
+ d_{2e}^* c_2 \Bigg[& \frac{\mathcal{E}_p e^{i(\omega_e-\omega_2-\omega_p)t}}{(\omega_e-\omega_2-\omega_p)-i\Gamma_e} + \frac{\mathcal{E}_p^* e^{i(\omega_e-\omega_2+\omega_p)t}}{(\omega_e-\omega_2+\omega_p)-i\Gamma_e} \\
& \frac{\mathcal{E}_{\mathcal{C}1} e^{i(\omega_e-\omega_2-\omega_{\mathcal{C}1})t}}{(\omega_e-\omega_2-\omega_{\mathcal{C}1})-i\Gamma_e} + \frac{\mathcal{E}_{\mathcal{C}1}^* e^{i(\omega_e-\omega_2+\omega_{\mathcal{C}1})t}}{(\omega_e-\omega_2+\omega_{\mathcal{C}1})-i\Gamma_e} \\
& \frac{\mathcal{E}_{\mathcal{C}2} e^{i(\omega_e-\omega_2-\omega_{\mathcal{C}2})t}}{(\omega_e-\omega_2-\omega_{\mathcal{C}2})-i\Gamma_e} + \frac{\mathcal{E}_{\mathcal{C}2}^* e^{i(\omega_e-\omega_2+\omega_{\mathcal{C}2})t}}{(\omega_e-\omega_2+\omega_{\mathcal{C}2})-i\Gamma_e} \Bigg] \Bigg\}
\end{aligned}
\qquad \text{[A.7]}
$$

This adiabatic elimination is an important simplification because it reduces the number of unknowns in the coupled system of rate equations given in Eqs. (A.5) and allows us to algebraically solve for a closed form of the rate equations.

We then plug in this slowly varying probability amplitude, c_e, into the rate equations for c_g, c_1, and c_2 and also expand the electric field $\mathcal{E}(t)$ into its Fourier components. The resulting expressions are very long with many terms. We use the rotating wave approximation to eliminate the off-resonant oscillating terms to derive truncated expressions for the rate equations containing only the slowly oscillating terms:

$$
\begin{aligned}
\dot{c}_g = \frac{i}{4\hbar^2}\Bigg\{ |d_{ge}|^2 c_g \Bigg[& |\mathcal{E}_p|^2 \left(\frac{1}{(\omega_e-\omega_g-\omega_p)-i\Gamma_e} + \frac{1}{(\omega_e-\omega_g+\omega_p)-i\Gamma_e} \right) \\
& + |\mathcal{E}_{\mathcal{C}1}|^2 \left(\frac{1}{(\omega_e-\omega_g-\omega_{\mathcal{C}1})-i\Gamma_e} + \frac{1}{(\omega_e-\omega_g+\omega_{\mathcal{C}1})-i\Gamma_e} \right)
\end{aligned}
$$

$$+\left|\mathcal{E}_{\mathcal{C}2}\right|^2\left(\frac{1}{(\omega_e-\omega_g-\omega_{\mathcal{C}2})-i\Gamma_e}\;+\;\frac{1}{(\omega_e-\omega_g+\omega_{\mathcal{C}2})-i\Gamma_e}\right)\Bigg]$$

$$+d_{ge}d_{1e}^{*}c_1\mathcal{E}_p\mathcal{E}_{\mathcal{C}1}^{*}e^{-i\delta\omega_1 t}\left(\frac{1}{(\omega_e-\omega_1-\omega_p)-i\Gamma_e}\;+\;\frac{1}{(\omega_e-\omega_1+\omega_{\mathcal{C}1})-i\Gamma_e}\right)$$

$$+d_{ge}d_{2e}^{*}c_2\mathcal{E}_{\mathcal{C}2}\mathcal{E}_p^{*}e^{-i\delta\omega_2 t}\left(\frac{1}{(\omega_e-\omega_2-\omega_{\mathcal{C}2})-i\Gamma_e}\;+\;\frac{1}{(\omega_e-\omega_2+\omega_p)-i\Gamma_e}\right)\Bigg\}\quad,$$

$$\dot{c}_1+\gamma_1c_1=\frac{i}{4\hbar^2}\Bigg\{d_{1e}d_{ge}^{*}c_g\mathcal{E}_{\mathcal{C}1}\mathcal{E}_p^{*}e^{i\delta\omega_1 t}\left(\frac{1}{(\omega_e-\omega_g-\omega_{\mathcal{C}1})-i\Gamma_e}\;+\;\frac{1}{(\omega_e-\omega_g+\omega_p)-i\Gamma_e}\right)$$

$$+\left|d_{1e}\right|^2c_1\Bigg[\left|\mathcal{E}_p\right|^2\left(\frac{1}{(\omega_e-\omega_1-\omega_p)-i\Gamma_e}\;+\;\frac{1}{(\omega_e-\omega_1+\omega_p)-i\Gamma_e}\right)$$

$$+\left|\mathcal{E}_{\mathcal{C}1}\right|^2\left(\frac{1}{(\omega_e-\omega_1-\omega_{\mathcal{C}1})-i\Gamma_e}\;+\;\frac{1}{(\omega_e-\omega_1+\omega_{\mathcal{C}1})-i\Gamma_e}\right)$$

$$+\left|\mathcal{E}_{\mathcal{C}2}\right|^2\left(\frac{1}{(\omega_e-\omega_1-\omega_{\mathcal{C}2})-i\Gamma_e}\;+\;\frac{1}{(\omega_e-\omega_1+\omega_{\mathcal{C}2})-i\Gamma_e}\right)\Bigg]\Bigg\},$$

$$\dot{c}_2+\gamma_2c_2=\frac{i}{4\hbar^2}\Bigg\{d_{2e}d_{ge}^{*}c_g\mathcal{E}_p\mathcal{E}_{\mathcal{C}2}^{*}e^{i\delta\omega_2 t}\left(\frac{1}{(\omega_e-\omega_g-\omega_p)-i\Gamma_e}\;+\;\frac{1}{(\omega_e-\omega_g+\omega_{\mathcal{C}2})-i\Gamma_e}\right)$$

$$+\left|d_{2e}\right|^2c_2\Bigg[\left|\mathcal{E}_p\right|^2\left(\frac{1}{(\omega_e-\omega_2-\omega_p)-i\Gamma_e}\;+\;\frac{1}{(\omega_e-\omega_2+\omega_p)-i\Gamma_e}\right)$$

$$+\left|\mathcal{E}_{\mathcal{C}1}\right|^2\left(\frac{1}{(\omega_e-\omega_2-\omega_{\mathcal{C}1})-i\Gamma_e}\;+\;\frac{1}{(\omega_e-\omega_2+\omega_{\mathcal{C}1})-i\Gamma_e}\right)$$

$$+\left|\mathcal{E}_{\mathcal{C}2}\right|^2\left(\frac{1}{(\omega_e-\omega_2-\omega_{\mathcal{C}2})-i\Gamma_e}\;+\;\frac{1}{(\omega_e-\omega_2+\omega_{\mathcal{C}2})-i\Gamma_e}\right)\Bigg]\Bigg\},\qquad\text{[A.8]}$$

where we have denoted the slowly oscillating terms with the two-photon detunings given by,

$$\delta\omega_1=(\omega_1-\omega_g)-(\omega_{\mathcal{C}1}-\omega_p)\quad,$$

$$\delta\omega_2=(\omega_2-\omega_g)-(\omega_p-\omega_{\mathcal{C}2})\quad.\qquad\text{[A.9]}$$

Following the formalism of Harris et al. [48, 51, 167], we define the Raman coupling coefficients:

$$\mathrm{a}_q\;=\;\frac{\left|d_{ge}\right|^2}{2\hbar^2}\left[\frac{1}{\omega_e-\omega_g-\omega_q-i\Gamma_e}+\frac{1}{\omega_e-\omega_g+\omega_q-i\Gamma_e}\right]\quad,$$

$$
\begin{aligned}
b_1 &= \frac{d_{ge}d_{1e}^*}{2\hbar^2}\left[\frac{1}{\omega_e-\omega_g-\omega_{\mathcal{C}1}-i\Gamma_e}+\frac{1}{\omega_e-\omega_g+\omega_p-i\Gamma_e}\right] \quad , \\
b_2 &= \frac{d_{ge}d_{2e}^*}{2\hbar^2}\left[\frac{1}{\omega_e-\omega_g-\omega_p-i\Gamma_e}+\frac{1}{\omega_e-\omega_g+\omega_{\mathcal{C}2}-i\Gamma_e}\right] \quad , \\
f_{1,q} &= \frac{|d_{1e}|^2}{2\hbar^2}\left[\frac{1}{\omega_e-\omega_1-\omega_q-i\Gamma_e}+\frac{1}{\omega_e-\omega_1+\omega_q-i\Gamma_e}\right] \quad , \\
f_{2,q} &= \frac{|d_{2e}|^2}{2\hbar^2}\left[\frac{1}{\omega_e-\omega_2-\omega_q-i\Gamma_e}+\frac{1}{\omega_e-\omega_2+\omega_q-i\Gamma_e}\right] \quad , \qquad \text{[A.10]}
\end{aligned}
$$

where we differ in the notation of Harris et al. in that we use the letters f and F instead of d and D to avoid confusion with our choice of d to denote the electric dipole moments. For convenience, we have used approximate forms for some of the denominator terms in Eqs. (A.8), such that a common definition of b_1 or b_2 may be substituted. Specifically, by examining the energy level diagram, the denominators of the cross terms in rate equation of c_g can be expressed in a from that resembles the cross terms in the rate equations of c_1 and c_2 as follows:

$$
\begin{aligned}
&\omega_e-\omega_1+\omega_{\mathcal{C}1}=\omega_e-\omega_g+\omega_p-\delta\omega_1 \quad \Rightarrow \quad \omega_e-\omega_1+\omega_{\mathcal{C}1}\approx\omega_e-\omega_g+\omega_p \quad , \\
&\omega_e-\omega_1-\omega_p=\omega_e-\omega_g-\omega_{\mathcal{C}1}-\delta\omega_1 \quad \Rightarrow \quad \omega_e-\omega_1-\omega_p\approx\omega_e-\omega_g-\omega_{\mathcal{C}1} \quad , \\
&\omega_e-\omega_2-\omega_{\mathcal{C}2}=\omega_e-\omega_g-\omega_p-\delta\omega_2 \quad \Rightarrow \quad \omega_e-\omega_2-\omega_{\mathcal{C}2}\approx\omega_e-\omega_g-\omega_p \quad , \\
&\omega_e-\omega_2+\omega_p=\omega_e-\omega_g+\omega_{\mathcal{C}2}-\delta\omega_2 \quad \Rightarrow \quad \omega_e-\omega_2+\omega_p\approx\omega_e-\omega_g+\omega_{\mathcal{C}2} \quad . \qquad \text{[A.11]}
\end{aligned}
$$

This approximation is valid because when the lasers are far-detuned from the electronic state the two-photon detunings are negligible compared to the single photon detunings. With the Raman coupling coefficients we define the quantities:

$$
\begin{aligned}
A &= \mathrm{a}_p\left|\mathcal{E}_p\right|^2+\mathrm{a}_{\mathcal{C}1}\left|\mathcal{E}_{\mathcal{C}1}\right|^2+\mathrm{a}_{\mathcal{C}2}\left|\mathcal{E}_{\mathcal{C}2}\right|^2 \quad , \\
B_1 &= b_1\mathcal{E}_p\mathcal{E}_{\mathcal{C}1}^* \quad , \\
B_2 &= b_2\mathcal{E}_p^*\mathcal{E}_{\mathcal{C}2} \quad , \\
F_1 &= f_{1,p}\left|\mathcal{E}_p\right|^2++f_{1,\mathcal{C}1}\left|\mathcal{E}_{\mathcal{C}1}\right|^2+f_{1,\mathcal{C}2}\left|\mathcal{E}_{\mathcal{C}2}\right|^2 \quad , \\
F_2 &= f_{2,p}\left|\mathcal{E}_p\right|^2++f_{2,\mathcal{C}1}\left|\mathcal{E}_{\mathcal{C}1}\right|^2+f_{2,\mathcal{C}2}\left|\mathcal{E}_{\mathcal{C}2}\right|^2 \quad . \qquad \text{[A.12]}
\end{aligned}
$$

Now we may express the rate equations of the system in a compact form:

$$\begin{aligned}
\dot{c}_g &= \frac{i}{2}Ac_g + \frac{i}{2}B_1 e^{-i\delta\omega_1 t}c_1 + \frac{i}{2}B_2 e^{-i\delta\omega_2 t}c_2 \quad , \\
\dot{c}_1 &= \frac{i}{2}B_1^* e^{i\delta\omega_1 t}c_g + \frac{i}{2}F_1 c_1 - \gamma_1 c_1 \quad , \\
\dot{c}_2 &= \frac{i}{2}B_2^* e^{i\delta\omega_2 t}c_g + \frac{i}{2}F_2 c_2 - \gamma_2 c_2 \quad . \qquad \text{[A.13]}
\end{aligned}$$

To suppress the oscillating terms of these equations, we apply a unitary transform to a rotating frame by the substitution:

$$\begin{aligned}
c_g &= \tilde{c}_g e^{i(\frac{Re(A)}{2})t} \quad , \\
c_1 &= \tilde{c}_1 e^{i(\delta\omega_1 + \frac{Re(A)}{2})t} \quad , \\
c_2 &= \tilde{c}_2 e^{i(\delta\omega_2 + \frac{Re(A)}{2})t} \quad , \qquad \text{[A.14]}
\end{aligned}$$

which transforms the equations to:

$$\begin{aligned}
\dot{\tilde{c}}_g + \frac{Im(A)}{2}\tilde{c}_g &= \frac{i}{2}B_1\tilde{c}_1 + \frac{i}{2}B_2\tilde{c}_2 \quad , \\
\dot{\tilde{c}}_1 + i\left[\delta\omega_1 - \frac{Re(F_1 - A)}{2}\right]\tilde{c}_1 + \left[\gamma_1 + \frac{Im(F_1)}{2}\right]\tilde{c}_1 &= \frac{i}{2}B_1^*\tilde{c}_g \quad , \\
\dot{\tilde{c}}_2 + i\left[\delta\omega_2 - \frac{Re(F_2 - A)}{2}\right]\tilde{c}_2 + \left[\gamma_2 + \frac{Im(F_2)}{2}\right]\tilde{c}_2 &= \frac{i}{2}B_2^*\tilde{c}_g \quad . \qquad \text{[A.15]}
\end{aligned}$$

We solve for steady state solutions for the probability amplitudes $\tilde{c}_1$ and $\tilde{c}_2$ in terms of $\tilde{c}_g$ by setting the derivatives $\dot{\tilde{c}}_1$ and $\dot{\tilde{c}}_2$ equal to zero:

$$\begin{aligned}
\tilde{c}_1 &= \frac{B_1^*\tilde{c}_g}{2[\delta\omega_1 - \frac{Re(F_1 - A)}{2} - i(\gamma_1 + \frac{Im(F_1)}{2})]} \quad , \\
\tilde{c}_2 &= \frac{B_2^*\tilde{c}_g}{2[\delta\omega_2 - \frac{Re(F_2 - A)}{2} - i(\gamma_2 + \frac{Im(F_2)}{2})]} \quad . \qquad \text{[A.16]}
\end{aligned}$$

The steady state solutions for the probability amplitudes complete our analysis of the time dynamics of the system and we can now begin to solve for the electric susceptibility of the system at the frequency of the probe beam. To begin, we consider the polarization of the system:

$$\begin{aligned}
P(t) &= N\left\langle\psi|\hat{d}|\psi\right\rangle \\
&= N\left(d_{ge}c_e c_g^* e^{-i(\omega_e - \omega_g)t} + d_{1e}c_e c_1^* e^{-i(\omega_e - \omega_1)t} + d_{2e}c_e c_2^* e^{-i(\omega_e - \omega_2)t} + h.c.\right). \qquad \text{[A.17]}
\end{aligned}$$

A complete expression for the polarization of the system can be found in terms of c_g, c_1, and c_2 by plugging in Eq. (A.7) for c_e, however it is tediously long. Our analysis can be simplified by considering a Fourier expansion of the polarization,

$$P(t) = Re\left[\sum_n P_n e^{-i\omega_n t}\right] = \sum_n \frac{1}{2}\left(P_n e^{-i\omega_n t} + P_n^* e^{i\omega_n t}\right) \quad , \tag{A.18}$$

since we are only interested in the polarization at the probe beam frequency, P_p. By noting that

$$2P(t) = \sum_n P_n e^{-i\omega_n t} + P_n^* e^{i\omega_n t} \quad , \tag{A.19}$$

we can solve for P_p by extracting all the terms of $2P(t)$ that include the oscillation $e^{-i\omega_p t}$. Thus we plug Eq. (A.7) into Eq. (A.17) and truncate the nonrelevant terms:

$$\begin{aligned} P(t) = \frac{N}{2\hbar} \quad \Bigg[\quad & |d_{ge}|^2 |c_g|^2 \mathcal{E}_p e^{-i\omega_p t}\left(\frac{1}{(\omega_e - \omega_g - \omega_p) - i\Gamma_e} + \frac{1}{(\omega_e - \omega_g + \omega_p) - i\Gamma_e}\right) \\ + \quad & d_{1e} d_{ge}^* c_g c_1^* \mathcal{E}_{\mathcal{C}1} e^{i(\omega_1 - \omega_g - \omega_{\mathcal{C}1})t}\left(\frac{1}{(\omega_e - \omega_g - \omega_{\mathcal{C}1}) - i\Gamma_e} + \frac{1}{(\omega_e - \omega_1 + \omega_{\mathcal{C}1}) - i\Gamma_e}\right) \\ + \quad & d_{ge} d_{2e}^* c_2 c_g^* \mathcal{E}_{\mathcal{C}2} e^{i(\omega_g - \omega_2 - \omega_{\mathcal{C}2})t}\left(\frac{1}{(\omega_e - \omega_2 - \omega_{\mathcal{C}2}) - i\Gamma_e} + \frac{1}{(\omega_e - \omega_g + \omega_{\mathcal{C}2}) - i\Gamma_e}\right) \\ + \quad & |d_{1e}|^2 |c_1|^2 \mathcal{E}_p e^{-i\omega_p t}\left(\frac{1}{(\omega_e - \omega_1 - \omega_p) - i\Gamma_e} + \frac{1}{(\omega_e - \omega_1 + \omega_p) - i\Gamma_e}\right) \\ + \quad & |d_{2e}|^2 |c_2|^2 \mathcal{E}_p e^{-i\omega_p t}\left(\frac{1}{(\omega_e - \omega_2 - \omega_p) - i\Gamma_e} + \frac{1}{(\omega_e - \omega_2 + \omega_p) - i\Gamma_e}\right) \\ + \quad & ... + h.c.\Bigg] \quad . \end{aligned} \tag{A.20}$$

Using the Raman coupling coefficients and noting,

$$\begin{aligned} \omega_g - \omega_1 + \omega_{\mathcal{C}1} &= \omega_p - \delta\omega_1 \quad , \\ \omega_2 - \omega_g + \omega_{\mathcal{C}2} &= \omega_p + \delta\omega_2 \quad , \end{aligned} \tag{A.21}$$

we can rewrite the polarization as:

$$\begin{aligned} P(t) = N\hbar \quad \Bigg[\quad & |d_{ge}|^2 |c_g|^2 \mathrm{a}_p \mathcal{E}_p e^{-i\omega_p t} + d_{1e} d_{ge}^* c_g c_1^* b_1^* \mathcal{E}_{\mathcal{C}1} e^{-i(\omega_p - \delta\omega_1)t} + d_{ge} d_{2e}^* c_2 c_g^* b_2 \mathcal{E}_{\mathcal{C}2} e^{-i(\omega_p + \delta\omega_2)t} \\ + \quad & |d_{1e}|^2 |c_1|^2 \mathcal{E}_p e^{-i\omega_p t} + |d_{2e}|^2 |c_2|^2 \mathcal{E}_p e^{-i\omega_p t} + ... + h.c.\Bigg] \quad . \end{aligned} \tag{A.22}$$

After extracting out the terms oscillating at the probe frequency we find the Fourier component of the polarization,

$$P_p = 2N\hbar \quad \Big[\quad |c_g|^2 \, \mathrm{a}_p \mathcal{E}_p + c_g c_1^* b_1^* \mathcal{E}_{\mathcal{C}1} e^{i\delta\omega_1 t} + c_2 c_g^* b_2^* \mathcal{E}_{\mathcal{C}1} e^{-i\delta\omega_2 t} \\ + \quad |c_1|^2 \, f_{1,p} \mathcal{E}_p + |c_2|^2 \, f_{2,p} \mathcal{E}_p \Big] \quad . \qquad \text{[A.23]}$$

Applying the rotating frame introduced in Eq. (A.14), we eliminate the slowly oscillating terms in the probe polarization

$$P_p = 2N\hbar \Big[|\tilde{c}_g|^2 \, \mathrm{a}_p \mathcal{E}_p + \tilde{c}_g \tilde{c}_1^* b_1^* \mathcal{E}_{\mathcal{C}1} + \tilde{c}_2 \tilde{c}_g^* b_2 \mathcal{E}_{\mathcal{C}2} + |\tilde{c}_1|^2 \, f_{1,p} \mathcal{E}_p + |\tilde{c}_2|^2 \, f_{2,p} \mathcal{E}_p \Big] \quad . \qquad \text{[A.24]}$$

One of the key assumptions we make is that the majority of the population remains in the ground state and there is negligible population in the Raman states because the system is far-off resonant and the probe beam is weak. The last two terms in Eq. (A.24) may be neglected under the assumption,

$$\begin{aligned} c_g c_g^* &\approx 1 \quad , \\ c_1 c_1^* &\ll 1 \quad , \\ c_2 c_2^* &\ll 1 \quad . \end{aligned} \qquad \text{[A.25]}$$

After plugging in the steady state probability amplitudes $\tilde{c}_1$ and $\tilde{c}_2$ from Eq. (A.16) into Eq. (A.24) we have

$$P_p = 2\hbar N \Bigg(a_p \quad + \quad \frac{|b_1|^2 \, |\mathcal{E}_{\mathcal{C}1}|^2}{2\left[\delta\omega_1 - \frac{Re(F_1 - A)}{2} + i\left(\gamma_1 + \frac{Im(F_1)}{2}\right)\right]} \\ + \quad \frac{|b_2|^2 \, |\mathcal{E}_{\mathcal{C}2}|^2}{2\left[\delta\omega_2 - \frac{Re(F_2 - A)}{2} - i\left(\gamma_2 + \frac{Im(F_2)}{2}\right)\right]} \Bigg) \mathcal{E}_p \quad . \qquad \text{[A.26]}$$

To compact the notation and rewrite the polarization expression in a format resembling a complex Lorentzian, we define the quantities

$$\begin{aligned} \tilde{\delta\omega_1} &= \delta\omega_1 - \frac{Re(F_1 - A)}{2} \quad , \\ \tilde{\delta\omega_2} &= \delta\omega_2 - \frac{Re(F_2 - A)}{2} \quad , \end{aligned}$$

$$\begin{aligned}\tilde{\gamma_1} &= \gamma_1 + \frac{Im(F_1)}{2} \quad , \\ \tilde{\gamma_2} &= \gamma_2 + \frac{Im(F_2)}{2} \quad . \end{aligned} \tag{A.27}$$

The terms $\frac{Re(F_1-A)}{2}$ and $\frac{Re(F_2-A)}{2}$ physically correspond to ac stark shifts of the system's levels that are proportional the intensity of the laser fields. Similarly the terms $\frac{Im(F_1)}{2}$ and $\frac{Im(F_2)}{2}$ correspond to power broadening of the level line widths.

Using the relation $P_p = \epsilon_0 \chi_{\mathcal{E}} \mathcal{E}_p$ with Eq. (A.26), we can find the susceptibility of the medium for the probe wave,

$$\chi_{\mathcal{E}} = \frac{2\hbar N}{\epsilon_0} \left(a_p + \frac{|b_1|^2}{2\left[\delta\tilde{\omega}_1 + i\tilde{\gamma_1}\right]} |\mathcal{E}_{\mathcal{C}1}|^2 + \frac{|b_2|^2}{2\left[\delta\tilde{\omega}_2 - i\tilde{\gamma_2}\right]} |\mathcal{E}_{\mathcal{C}2}|^2 \right) \quad . \tag{A.28}$$

A.2 Six level system for negative refractive index

The derivation of the refractive index in the Raman cross-coupled scheme follows very similarly to the derivation of the far-off resonant Raman system above, however there are additional magnetic resonance terms. We begin by expanding the wave function of the 6 level system in the interaction picture:

$$\begin{aligned}|\psi\rangle &= c_g \exp(-i\omega_g t)|g\rangle + c_1 \exp(-i\omega_1 t)|1\rangle + c_2 \exp(-i\omega_2 t)|2\rangle \\ &+ c_m \exp(-i\omega_m t)|m\rangle + c_a \exp(-i\omega_a t)|a\rangle + c_b \exp(-i\omega_b t)|b\rangle \quad . \end{aligned} \tag{A.29}$$

The total Hamiltonian of the system is the addition of the unperturbed Hamiltonian and the interaction Hamiltonian, given by:

$$\begin{aligned}\hat{H}_0 &= \hbar\omega_g|g\rangle\langle g| + \hbar\omega_1|1\rangle\langle 1| + \hbar\omega_2|2\rangle\langle 2| + \hbar\omega_m|m\rangle\langle m| + \hbar\omega_a|a\rangle\langle a| + \hbar\omega_b|b\rangle\langle b| \quad , \\ \hat{H}_{int} &= -\hat{d}\mathcal{E} - \hat{\mu}\mathcal{B} = -d_{ga}\mathcal{E}|g\rangle\langle a| - d_{gb}\mathcal{E}|g\rangle\langle b| - d_{1a}\mathcal{E}|1\rangle\langle a| - d_{2b}\mathcal{E}|2\rangle\langle b| \\ &\quad -\mu_{gm}\mathcal{B}|g\rangle\langle m| - \mu_{2m}\mathcal{B}|2\rangle\langle m| + h.c. \quad , \end{aligned} \tag{A.30}$$

where d and μ are the electric and magnetic dipole transition matrix elements, respectively. The electric and magnetic fields, $\mathcal{E}$ and $\mathcal{B}$ are expanded in Fourier components,

$$\mathcal{E} = Re\left\{\mathcal{E}_p e^{-i\omega_p t} + \mathcal{E}_{\mathcal{C}1} e^{-i\omega_{\mathcal{C}1} t} + \mathcal{E}_{\mathcal{C}2} e^{-i\omega_{\mathcal{C}2} t}\right\} \quad ,$$

$$\mathcal{B} = Re\left\{\mathcal{B}_p e^{-i\omega_p t} + \mathcal{B}_{2m} e^{-i\omega_{2m} t}\right\} \quad . \qquad \text{[A.31]}$$

With these definitions for the Hamiltonian and the electric and magnetic fields, we use the Schrödinger equation and adiabatic elimination of the excited state amplitudes to derive the simplified rate equations:

$$\begin{aligned}
\dot{c}_g &= \frac{i}{2}Ac_g + \frac{i}{2}B_1 e^{-i\delta\omega_1 t}c_1 + \frac{i}{2}B_2 e^{-i\delta\omega_2 t}c_2 + \frac{i}{2}\Omega_{gm} e^{-i\delta\omega_{\mathcal{B}} t}c_m \quad , \\
\dot{c}_1 &= \frac{i}{2}B_1^* e^{i\delta\omega_1 t}c_g + \frac{i}{2}F_1 c_1 - \gamma_1 c_1 \quad , \\
\dot{c}_2 &= \frac{i}{2}B_2^* e^{i\delta\omega_2 t}c_g + \frac{i}{2}F_2 c_2 + \frac{i}{2}\Omega_{2m} e^{-i\delta\omega_\Omega t}c_m - \gamma_2 c_2 \quad , \\
\dot{c}_m &= \frac{i}{2}\Omega_{gm}^* e^{i\delta\omega_{\mathcal{B}} t}c_g + \frac{i}{2}\Omega_{2m}^* e^{i\delta\omega_\Omega t}c_m - \gamma_m c_m \quad , \qquad \text{[A.32]}
\end{aligned}$$

where we have introduced the detunings,

$$\begin{aligned}
\delta\omega_1 &= (\omega_1 - \omega_g) - (\omega_{\mathcal{C}1} - \omega_p) \quad , \\
\delta\omega_2 &= (\omega_2 - \omega_g) - (\omega_p - \omega_{\mathcal{C}2}) \quad , \\
\delta\omega_{\mathcal{B}} &= (\omega_m - \omega_g) - \omega_p \quad , \\
\delta\omega_\Omega &= (\omega_m - \omega_2) - \omega_{2m} \quad , \qquad \text{[A.33]}
\end{aligned}$$

and the magnetic transition Rabi frequencies, $\Omega_{gm} = \mu_{gm}\mathcal{B}_p^*/\hbar$ and $\Omega_{2m} = \mu_{2m}\mathcal{B}_{2m}^*/\hbar$.

To suppress the oscillating terms of these equations, we apply a unitary transform to a rotating frame by the substitution:

$$\begin{aligned}
c_g &= \tilde{c}_g e^{i(\frac{Re(A)}{2})t} \quad , \\
c_1 &= \tilde{c}_1 e^{i(\delta\omega_1 + \frac{Re(A)}{2})t} \quad , \\
c_2 &= \tilde{c}_2 e^{i(\delta\omega_2 + \frac{Re(A)}{2})t} \quad , \\
c_m &= \tilde{c}_m e^{i(\delta\omega_{\mathcal{B}} + \frac{Re(A)}{2})t} \quad , \qquad \text{[A.34]}
\end{aligned}$$

which re-expresses the rate equations as:

$$\dot{\tilde{c}}_g + \frac{Im(A)}{2}\tilde{c}_g = \frac{i}{2}B_1\tilde{c}_1 + \frac{i}{2}B_2\tilde{c}_2 + \frac{i}{2}\Omega_{gm}\tilde{c}_m \quad ,$$

$$
\begin{aligned}
\dot{\tilde{c}}_1 + i\left[\delta\omega_1 - \frac{Re(F_1 - A)}{2}\right]\tilde{c}_1 + \left[\gamma_1 + \frac{Im(F_1)}{2}\right]\tilde{c}_1 &= \frac{i}{2}B_1^*\tilde{c}_g \quad , \\
\dot{\tilde{c}}_2 + i\left[\delta\omega_2 - \frac{Re(F_2 - A)}{2}\right]\tilde{c}_2 + \left[\gamma_2 + \frac{Im(F_2)}{2}\right]\tilde{c}_2 &= \frac{i}{2}B_2^*\tilde{c}_g + \frac{i}{2}\Omega_{2m}e^{i(\delta\omega_{\mathcal{B}} - \delta\omega_\Omega - \delta\omega_2)t}\tilde{c}_m \quad , \\
\dot{\tilde{c}}_m + i\left[\delta\omega_{\mathcal{B}} + \frac{Re(A)}{2}\right]\tilde{c}_m + \gamma_m\tilde{c}_m &= \frac{i}{2}\Omega_{gm}^*\tilde{c}_g + \frac{i}{2}\Omega_{2m}^*e^{-i(\delta\omega_{\mathcal{B}} - \delta\omega_\Omega - \delta\omega_2)t}\tilde{c}_2 \quad .
\end{aligned}
\qquad \text{[A.35]}
$$

For simplicity we impose the condition,

$$
\delta\omega_{\mathcal{B}} = \delta\omega_2 + \delta\omega_\Omega \quad , \qquad \text{[A.36]}
$$

to eliminate rotation of the magnetic resonance of the coupling beam, Ω_{2m}.

We find the steady-state values for the probability amplitudes in terms of $\tilde{c}_g$ by setting derivatives equal to zero and algebraically solving for:

$$
\begin{aligned}
\tilde{c}_1 &= \left\{\frac{B_1^*}{2\left[\delta\omega_1 - \frac{Re(F_1 - A)}{2} - i\left(\gamma_1 + \frac{Im(F_1)}{2}\right)\right]}\right\}\tilde{c}_g \quad , \\
\tilde{c}_2 &= \left\{\frac{2B_2^*\left[\delta\omega_{\mathcal{B}} + \frac{Re(A)}{2} - i\gamma_m\right] + \Omega_{2m}\Omega_{gm}^*}{4\left[\delta\omega_2 - \frac{Re(F_2 - A) - i\left(\gamma_2 + \frac{Im(F_2)}{2}\right)}{2}\right]\left[\delta\omega_{\mathcal{B}} + \frac{Re(A)}{2} - i\gamma_m\right] - |\Omega_{2m}|^2}\right\}\tilde{c}_g \quad , \\
\tilde{c}_m &= \left\{\frac{\Omega_{gm}^*}{2\left[\delta\omega_{\mathcal{B}} + \frac{Re(A)}{2} - i\gamma_m\right]}\right. \\
&+ \frac{B_2^*\Omega_{2m}^*}{4\left[\delta\omega_{\mathcal{B}} + \frac{Re(A)}{2} - i\gamma_m\right]\left[\delta\omega_2 - \frac{Re(F_2 - A)}{2} - \frac{|\Omega_{2m}|^2}{4\left(\delta\omega_{\mathcal{B}} + \frac{Re(A)}{2} - i\gamma_m\right)} - i\left(\gamma_2 + \frac{Im(F_2)}{2}\right)\right]} \\
&\left. + \frac{|\Omega_{2m}|^2\,\Omega_{gm}^*}{8\left[\delta\omega_{\mathcal{B}} + \frac{Re(A)}{2} - i\gamma_m\right]^2\left[\delta\omega_2 - \frac{Re(F_2 - A)}{2} - \frac{|\Omega_{2m}|^2}{4\left(\delta\omega_{\mathcal{B}} + \frac{Re(A)}{2} - i\gamma_m\right)} - i\left(\gamma_2 + \frac{Im(F_2)}{2}\right)\right]}\right\}\tilde{c}_g \quad .
\end{aligned}
\qquad \text{[A.37]}
$$

The polarization and magnetization of the system are given by the quantum expectation values,

$$
\begin{aligned}
P(t) &= N\left\langle\psi|\hat{d}|\psi\right\rangle \quad , \\
M(t) &= N\left\langle\psi|\hat{\mu}|\psi\right\rangle \quad .
\end{aligned}
\qquad \text{[A.38]}
$$

Following the method used in the above, the adiabatically eliminated probability amplitudes of the excited electronic states are used to simplify the polarization and magnetization expressions resulting from Eqs.(A.38). The probe beam Fourier components of the polarization and magnetization, P_p and M_p, respectively, are found by truncating these expressions to include only the terms oscillating near the probe frequency. These reduced expressions for the Fourier components in the rotating frame are given by,

$$\begin{aligned} P_p &= 2N\hbar\Big[\left|\tilde{c_g}\right|^2 \mathrm{a}_p\mathcal{E}_p + \tilde{c_g}\tilde{c_1^*}b_1^*\mathcal{E}_{\mathcal{C}1} + \tilde{c_2}\tilde{c_g^*}b_2\mathcal{E}_{\mathcal{C}2} + \left|\tilde{c_1}\right|^2 f_{1,p}\mathcal{E}_p + \left|\tilde{c_2}\right|^2 f_{2,p}\mathcal{E}_p\Big] \quad , \\ M_p &= 2N\Big[\tilde{c_m}\tilde{c_g^*}\mu_{gm} + \tilde{c_m}\tilde{c_2^*}\mu_{gm}^* e^{-i\omega_{\mathcal{C}2}t}\Big] \quad . \end{aligned} \tag{A.39}$$

Again, we assume the majority of the population remains in the ground state and there is negligible population in the other states, such that

$$\begin{aligned} c_g c_g^* &\approx 1 \quad , \\ c_1 c_1^* &\ll 1 \quad , \\ c_2 c_2^* &\ll 1 \quad , \\ c_m c_m^* &\ll 1 \quad . \end{aligned} \tag{A.40}$$

We then neglect the small terms in the P_p and M_p and equate them to the definitions of the polarization and magnetization in terms of the polarizability coefficients giving,

$$\begin{aligned} P_p &= 2\hbar N\left(\mathrm{a}_p\left|\tilde{c_g}\right|^2\mathcal{E}_p + b_1^*\tilde{c_g}\tilde{c_1^*}\mathcal{E}_{\mathcal{C}1} + b_2\tilde{c_g^*}\tilde{c_2}\mathcal{E}_{\mathcal{C}2}\right) \equiv N\left(\alpha_{\mathcal{E}\mathcal{E}}\mathcal{E}_p + \alpha_{\mathcal{E}\mathcal{B}}\mathcal{B}_p\right) \quad , \\ M_p &= 2N\tilde{c_g^*}\tilde{c_m}\mu_{gm} \equiv N\left(\alpha_{\mathcal{B}\mathcal{E}}\mathcal{E}_p + \alpha_{\mathcal{B}\mathcal{B}}\mathcal{B}_p\right) \quad . \end{aligned} \tag{A.41}$$

The cross-coupled polarizability coefficients can be found by plugging in the steady-state probability amplitudes of Eqs. (A.37) into Eqs. (A.41) and then appropriately factoring out the probe electric and magnetic field amplitudes, $\mathcal{E}_p$ and $\mathcal{B}_p$. Thus the coefficients are given by:

$$\alpha_{\mathcal{E}\mathcal{E}} = 2\hbar\mathrm{a}_p + \frac{\hbar\left|b_1\right|^2\left|\mathcal{E}_{\mathcal{C}1}\right|^2}{\left[\tilde{\delta\omega_1} + i\left(\gamma_1 + \frac{Im(F_1)}{2}\right)\right]} + \frac{\hbar\left|b_2\right|^2\left|\mathcal{E}_{\mathcal{C}2}\right|^2}{\left[\tilde{\delta\omega_2} - \frac{\left|\Omega_{2m}\right|^2}{4\left(\tilde{\delta\omega_{\mathcal{B}}} - i\gamma_m\right)} - i\left(\gamma_2 + \frac{Im(F_2)}{2}\right)\right]} \quad ,$$

$$\alpha_{\mathcal{B}\mathcal{B}} = \frac{\left|\mu_{gm}\right|^2}{\hbar\left[\left(\tilde{\delta\omega_{\mathcal{B}}} - i\gamma_m\right) - \frac{\left|\Omega_{2m}\right|^2}{4\left(\tilde{\delta\omega_2} - i\left(\gamma_2 + \frac{Im(F_2)}{2}\right)\right)}\right]} \quad ,$$

$$\begin{aligned}
\alpha_{\mathcal{EB}} &= \frac{b_2\mu^*_{gm}\mathcal{E}_{\mathcal{C}2}\Omega_{2m}}{2\left(\tilde{\delta\omega}_{\mathcal{B}} + -i\gamma_m\right)\left[\tilde{\delta\omega}_2 - \frac{|\Omega_{2m}|^2}{4\left(\tilde{\delta\omega}_{\mathcal{B}} - i\gamma_m\right)} - i\left(\gamma_2 + \frac{Im(F_2)}{2}\right)\right]} \quad , \\
\alpha_{\mathcal{BE}} &= \frac{b^*_2\mu_{gm}\mathcal{E}^*_{\mathcal{C}2}\Omega^*_{2m}}{2\left(\tilde{\delta\omega}_{\mathcal{B}} - i\gamma_m\right)\left[\tilde{\delta\omega}_2 - \frac{|\Omega_{2m}|^2}{4\left(\tilde{\delta\omega}_{\mathcal{B}} - i\gamma_m\right)} - i\left(\gamma_2 + \frac{Im(F_2)}{2}\right)\right]} \quad ,
\end{aligned} \qquad \text{[A.42]}$$

where we have introduced a simplified notation for the detunings that includes the AC Stark shifts,

$$\begin{aligned}
\tilde{\delta\omega}_{\mathcal{B}} &= \delta\omega_B + \frac{Re(A)}{2} \quad , \\
\tilde{\delta\omega}_1 &= \delta\omega_1 - \frac{Re(F_1 - A)}{2} \quad , \\
\tilde{\delta\omega}_2 &= \delta\omega_2 - \frac{Re(F_2 - A)}{2} \quad .
\end{aligned} \qquad \text{[A.43]}$$

Appendix B: Index of refraction in a magnetoelectric cross coupled system

B.1 General wave equation in cross coupled media

In most materials polarization occurs in response to an applied electric field and similarly magnetization in the presence of a magnetic field. However, cross-coupled materials do exist that become polarized in a magnetic field and magnetized in an electric field. Materials such as these are related to aspects in physics and chemistry such as optical activity or rotation, where linear polarized light experiences a rotation as it propagates through the material. To account for these cross-coupled behaviors the constitutive relations of bianisotropic media given by,

$$\vec{P} = \epsilon_0 \bar{\chi}_{\mathcal{E}} \vec{\mathcal{E}} + \frac{1}{c} \bar{\xi}_{\mathcal{EB}} \vec{\mathcal{H}} \quad , \tag{B.1}$$

$$\vec{M} = \frac{1}{c\mu_0} \bar{\xi}_{\mathcal{BE}} \vec{\mathcal{E}} + \bar{\chi}_{\mathcal{B}} \vec{\mathcal{H}} \quad , \tag{B.2}$$

present a more general treatment where the polarization includes a magnetic field term and the magnetization includes an electric field term. $\bar{\chi}_{\mathcal{E}}$ and $\bar{\chi}_{\mathcal{B}}$ are the electric and magnetic susceptibility tensors and $\bar{\xi}_{\mathcal{EB}}$ and $\bar{\xi}_{\mathcal{BE}}$ are the magnetoelectric coupling (chirality) coefficient tensors.

The index of refraction of a medium is defined by the ratio of an electromagnetic wave's phase velocity to the speed of light in a vacuum,

$$n = \frac{c}{v} \quad . \tag{B.3}$$

To determine the phase velocity of a wave propagating in a material we consider a plane E-M wave,

$$\begin{aligned} \vec{\mathcal{E}}(t) &= \vec{\mathcal{E}}_0 e^{i\left(\vec{k}\cdot\vec{r}-\omega t\right)} \quad , \quad \vec{\mathcal{E}}_0 = \mathcal{E}_0 \hat{e}_{\mathcal{E}} \quad , \\ \vec{\mathcal{H}}(t) &= \vec{\mathcal{H}}_0 e^{i\left(\vec{k}\cdot\vec{r}-\omega t\right)} \quad , \quad \vec{\mathcal{H}}_0 = \mathcal{H}_0 \hat{e}_{\mathcal{H}} \quad , \end{aligned} \tag{B.4}$$

and use Maxwell's equations in matter for the curl of the fields,

$$\begin{aligned} \nabla \times \vec{\mathcal{E}} &= -\frac{\partial}{\partial t} \vec{\mathcal{B}} \quad , \\ \nabla \times \vec{\mathcal{H}} &= \frac{\partial}{\partial t} \vec{D} \quad . \end{aligned} \tag{B.5}$$

The material fields include the polarization and magnetization terms according to the constitutive relations

$$\begin{aligned} \vec{D} &= \epsilon_0\vec{\mathcal{E}} + \vec{P} = \epsilon_0\vec{\mathcal{E}} + \epsilon_0\bar{\chi}_{\mathcal{E}}\vec{\mathcal{E}} + \frac{1}{c}\bar{\xi}_{\mathcal{EB}}\vec{\mathcal{H}} \quad , \\ \vec{\mathcal{B}} &= \mu_0\left(\vec{\mathcal{H}} + \vec{M}\right) = \mu_0\vec{\mathcal{H}} + \frac{1}{c}\bar{\xi}_{\mathcal{BE}}\vec{\mathcal{E}} + \mu_0\bar{\chi}_{\mathcal{B}}\vec{\mathcal{H}} \quad . \end{aligned} \tag{B.6}$$

After introducing the relative permittivity tensor, $\bar{\epsilon} = 1 + \bar{\chi}_{\mathcal{E}}$, and relative permeability tensor, $\bar{\mu} = 1 + \bar{\chi}_{\mathcal{B}}$, the material fields may be factored as,

$$\begin{aligned} \vec{D} &= \epsilon_0\bar{\epsilon}\vec{\mathcal{E}} + \frac{1}{c}\bar{\xi}_{\mathcal{EB}}\vec{\mathcal{H}} \quad , \\ \vec{\mathcal{B}} &= \mu_0\bar{\mu}\vec{\mathcal{H}} + \frac{1}{c}\bar{\xi}_{\mathcal{BE}}\vec{\mathcal{E}} \quad . \end{aligned} \tag{B.7}$$

Then we plug these material field expressions into Maxwell's curl relations from Eq. (B.5), giving

$$\begin{aligned} \nabla\times\vec{\mathcal{E}} &= -\frac{\partial}{\partial t}\left(\mu_0\bar{\mu}\vec{\mathcal{H}} + \frac{1}{c}\bar{\xi}_{\mathcal{BE}}\vec{\mathcal{E}}\right) \quad , \\ \nabla\times\vec{\mathcal{H}} &= \frac{\partial}{\partial t}\left(\epsilon_0\bar{\epsilon}\vec{\mathcal{E}} + \frac{1}{c}\bar{\xi}_{\mathcal{EB}}\vec{\mathcal{H}}\right) \quad . \end{aligned} \tag{B.8}$$

The space and time derivatives of the curl relations can be performed for the plane E-M, we defined in Eqs. (B.4), by the transformations $\nabla\times \rightarrow i\vec{k}\times$ and $\frac{\partial}{\partial t} \rightarrow -i\omega$, which give

$$i\vec{k}\times\vec{\mathcal{E}}_0 = i\omega\left(\mu_0\bar{\mu}\vec{\mathcal{H}}_0 + \frac{1}{c}\bar{\xi}_{\mathcal{BE}}\vec{\mathcal{E}}_0\right) \quad , \tag{B.9}$$

$$i\vec{k}\times\vec{\mathcal{H}}_0 = -i\omega\left(\epsilon_0\bar{\epsilon}\vec{\mathcal{E}}_0 + \frac{1}{c}\bar{\xi}_{\mathcal{EB}}\vec{\mathcal{H}}_0\right) \quad . \tag{B.10}$$

These expressions can be rearranged to group the common field terms as

$$\omega\mu_0\bar{\mu}\vec{\mathcal{H}}_0 = \left(\vec{k}\times\bar{1} - \frac{\omega}{c}\bar{\xi}_{\mathcal{BE}}\right)\vec{\mathcal{E}}_0 \quad , \tag{B.11}$$

$$-\omega\epsilon_0\bar{\epsilon}\vec{\mathcal{E}}_0 = \left(\vec{k}\times\bar{1} + \frac{\omega}{c}\bar{\xi}_{\mathcal{EB}}\right)\vec{\mathcal{H}}_0 \quad . \tag{B.12}$$

Using Eq. (B.11) we solve for the magnetic field term,

$$\vec{\mathcal{H}}_0 = \frac{1}{\omega\mu_0}\bar{\mu}^{-1}\left(\vec{k}\times\bar{1} - \frac{\omega}{c}\bar{\xi}_{\mathcal{BE}}\right)\vec{\mathcal{E}}_0 \quad , \tag{B.13}$$

and then plug this into Eq. (B.12) to find the expression

$$\bar{\epsilon}\vec{\mathcal{E}}_0 = -\frac{1}{\omega^2\epsilon_0\mu_0}\left(\vec{k}\times\bar{1} + \frac{\omega}{c}\bar{\xi}_{\mathcal{EB}}\right)\bar{\mu}^{-1}\left(\vec{k}\times\bar{1} - \frac{\omega}{c}\bar{\xi}_{\mathcal{BE}}\right)\vec{\mathcal{E}}_0 \quad , \tag{B.14}$$

solely in terms of the electric field term. Thus we now have the final wave equation governing propagation in a magnetoelectric cross-coupled material, given by

$$\left\{\bar{\epsilon} + \left(\frac{c}{\omega}\vec{k}\times\bar{1} + \bar{\xi}_{\mathcal{EB}}\right)\bar{\mu}^{-1}\left(\frac{c}{\omega}\vec{k}\times\bar{1} - \bar{\xi}_{\mathcal{BE}}\right)\right\}\vec{\mathcal{E}}_0 = 0 \quad . \tag{B.15}$$

In order to determine the refractive index of the material we must find a wave vector, $\vec{k}$, which satisfies this propagation equation for a given field polarization vector, $\hat{e}_{\mathcal{E}}$. Finding a general solution for $\vec{k}$ presents a difficult task.

B.2 Circular polarization solution in cross coupled media

Following the suggestion of Fleischhauer et al. [62], we consider the case of a circularly polarized light wave propagating in a material with magnetoelectric cross coupling. For simplicity we take the permittivity and permeability tensors to be isotropic, $\bar{\epsilon} = \epsilon\bar{1}$, $\bar{\mu} = \mu\bar{1}$, and we consider a wave propagating in the $+z$ direction with wave vector,

$$\vec{k} = k_z\hat{e}_z = \begin{bmatrix} 0 \\ 0 \\ k_z \end{bmatrix} \quad . \tag{B.16}$$

If we assume the cross-coupling tensors $\bar{\xi}_{\mathcal{EB}}$ and $\bar{\xi}_{\mathcal{BE}}$ are diagonal in a circular polarization basis, $\{\hat{e}_+, \hat{e}_-, \hat{e}_z\}$, where $\hat{e}_\pm = (\hat{e}_x \pm i\hat{e}_y)/\sqrt{2}$, then

$$\bar{\xi}_{\mathcal{EB}} = \begin{bmatrix} \left(\xi^+_{\mathcal{EB}} + \xi^-_{\mathcal{EB}}\right)/2 & -i\left(\xi^+_{\mathcal{EB}} - \xi^-_{\mathcal{EB}}\right)/2 & 0 \\ i\left(\xi^+_{\mathcal{EB}} - \xi^-_{\mathcal{EB}}\right)/2 & \left(\xi^+_{\mathcal{EB}} + \xi^-_{\mathcal{EB}}\right)/2 & 0 \\ 0 & 0 & \xi^z_{\mathcal{EB}} \end{bmatrix} \quad , \tag{B.17}$$

and similarly for $\bar{\xi}_{\mathcal{BE}}$.

We consider a right circularly polarized wave given by

$$\vec{\mathcal{E}}_0 = \mathcal{E}_0 \hat{e}_- = \frac{\mathcal{E}_0}{\sqrt{2}} \begin{bmatrix} 1 \\ -i \\ 0 \end{bmatrix} \quad , \qquad \text{[B.18]}$$

and plug the wave vector of Eq. (B.16) into the propagation equation of Eq. (B.15). This gives

$$\left\{ \epsilon\mu\bar{1} + \left(\frac{c}{\omega} \begin{bmatrix} 0 \\ 0 \\ k_z \end{bmatrix} \times \bar{1} + \bar{\xi}_{\mathcal{EB}} \right) \left(\frac{c}{\omega} \begin{bmatrix} 0 \\ 0 \\ k_z \end{bmatrix} \times \bar{1} - \bar{\xi}_{\mathcal{BE}} \right) \right\} \frac{\mathcal{E}_0}{\sqrt{2}} \begin{bmatrix} 1 \\ -i \\ 0 \end{bmatrix} = 0 \quad . \qquad \text{[B.19]}$$

After performing the appropriate vector operations this expression reduces to

$$\left\{ \epsilon\mu + \left(i\frac{c}{\omega} k_z^- + \xi_{\mathcal{EB}}^- \right) \left(i\frac{c}{\omega} k_z^- - \xi_{\mathcal{BE}}^- \right) \right\} \begin{bmatrix} 1 \\ -i \\ 0 \end{bmatrix} = 0 \quad , \qquad \text{[B.20]}$$

from this we can extract the scalar expression,

$$\epsilon\mu + \left(i\frac{c}{\omega} k_z^- + \xi_{\mathcal{EB}}^- \right) \left(i\frac{c}{\omega} k_z^- - \xi_{\mathcal{BE}}^- \right) = 0 \quad . \qquad \text{[B.21]}$$

With the reduction of the wave vector, $\vec{k}$, to a scalar, k_z^-, we can determine the wave's phase velocity $v^- = \frac{\omega}{k_z^-}$. Thus the refractive index for a right circular polarization is given by,

$$n^- = k_z^- \frac{c}{\omega} \quad , \qquad \text{[B.22]}$$

which we substitute into Eq. (B.21). This results in the expression,

$$\epsilon\mu + \left(in^- + \xi_{\mathcal{EB}}^- \right) \left(in^- - \xi_{\mathcal{BE}}^- \right) = 0 \quad . \qquad \text{[B.23]}$$

We now arrive at the formula,

$$n^- = \sqrt{\epsilon\mu - \frac{\left(\xi_{\mathcal{EB}}^- + \xi_{\mathcal{BE}}^- \right)^2}{4}} + \frac{i}{2} \left(\xi_{\mathcal{EB}}^- - \xi_{\mathcal{BE}}^- \right) \quad , \qquad \text{[B.24]}$$

for the refractive index in a magnetoelectric cross coupled material for a right circular polarization. A similar analysis for a left circular polarization will result in the expression,

$$n^{+} = \sqrt{\epsilon\mu - \frac{\left(\xi^{+}_{\mathcal{EB}} + \xi^{+}_{\mathcal{BE}}\right)^{2}}{4}} - \frac{i}{2}\left(\xi^{+}_{\mathcal{EB}} - \xi^{+}_{\mathcal{BE}}\right) \quad . \qquad \text{[B.25]}$$

These refractive indices are some times referred to as chiral indices because the refractive index depends on the “handedness” of the circular polarization.

Appendix C: Density matrix of Raman negative index system

C.1 Density matrix equations

In order to numerically time evolution of coherences we consider a density matrix formalism for the system. We express the quantum state of the system as a pure state vector:

$$|\psi\rangle = \begin{bmatrix} c_g & c_1 & c_2 & c_m & c_a & c_b \end{bmatrix}^T \quad , \tag{C.1}$$

with $\sum_i |c_i|^2 = 1$. Noting that a coherence is defined as $\rho_{ij} = c_i {c_j}^*$, the density matrix ρ is given by

$$\rho = |\psi\rangle\langle\psi| = \begin{bmatrix} \rho_{gg} & \rho_{g1} & \rho_{g2} & \rho_{gm} & \rho_{ga} & \rho_{gb} \\ \rho_{1g} & \rho_{11} & \rho_{12} & \rho_{1m} & \rho_{1a} & \rho_{1b} \\ \rho_{2g} & \rho_{21} & \rho_{22} & \rho_{2m} & \rho_{2a} & \rho_{2b} \\ \rho_{mg} & \rho_{m1} & \rho_{m2} & \rho_{mm} & \rho_{ma} & \rho_{mb} \\ \rho_{ag} & \rho_{a1} & \rho_{a2} & \rho_{am} & \rho_{aa} & \rho_{ab} \\ \rho_{bg} & \rho_{b1} & \rho_{b2} & \rho_{bm} & \rho_{ba} & \rho_{bb} \end{bmatrix} \quad . \tag{C.2}$$

The time evolution of the density matrix is given by

$$\dot{\rho} = -\frac{i}{\hbar}[H, \rho] - \frac{1}{2}\{\Gamma, \rho\} \quad , \tag{C.3}$$

where $H = H_0 + H_{int}$ is the Hamiltonian matrix and Γ is the decay matrix of the system given by

$$\Gamma = \begin{bmatrix} \gamma_g & 0 & 0 & 0 & 0 & 0 \\ 0 & \gamma_1 & 0 & 0 & 0 & 0 \\ 0 & 0 & \gamma_2 & 0 & 0 & 0 \\ 0 & 0 & 0 & \gamma_m & 0 & 0 \\ 0 & 0 & 0 & 0 & \Gamma_a & 0 \\ 0 & 0 & 0 & 0 & 0 & \Gamma_b \end{bmatrix} \quad . \tag{C.4}$$

The unperturbed Hamiltonian is

$$H_0 = \begin{bmatrix} \hbar\omega_g & 0 & 0 & 0 & 0 & 0 \\ 0 & \hbar\omega_1 & 0 & 0 & 0 & 0 \\ 0 & 0 & \hbar\omega_2 & 0 & 0 & 0 \\ 0 & 0 & 0 & \hbar\omega_m & 0 & 0 \\ 0 & 0 & 0 & 0 & \hbar\omega_a & 0 \\ 0 & 0 & 0 & 0 & 0 & \hbar\omega_b \end{bmatrix} \quad , \qquad \text{[C.5]}$$

and the interaction Hamiltonian is $H_{int} = -d\mathcal{E} - \mu\mathcal{B}$, where d and μ are the electric and magnetic dipole transition matrices, respectively, given by

$$d = \begin{bmatrix} 0 & 0 & 0 & 0 & d_{ga} & d_{gb} \\ 0 & 0 & 0 & 0 & d_{1a} & 0 \\ 0 & 0 & 0 & 0 & 0 & d_{2b} \\ 0 & 0 & 0 & 0 & 0 & 0 \\ d^*_{ga} & d^*_{1a} & 0 & 0 & 0 & 0 \\ d^*_{gb} & 0 & d^*_{2b} & 0 & 0 & 0 \end{bmatrix} \quad , \qquad \text{[C.6]}$$

$$\mu = \begin{bmatrix} 0 & 0 & 0 & \mu_{gm} & 0 & 0 \\ 0 & 0 & 0 & \mu_{1m} & 0 & 0 \\ 0 & 0 & 0 & \mu_{2m} & 0 & 0 \\ \mu^*_{gm} & \mu^*_{1m} & \mu^*_{2m} & 0 & 0 & 0 \\ 0 & 0 & 0 & 0 & 0 & 0 \\ 0 & 0 & 0 & 0 & 0 & 0 \end{bmatrix} \quad . \qquad \text{[C.7]}$$

A general expression for H_{int} is tediously long when the $\mathcal{E}$ and $\mathcal{B}$ are expanded in Fourier components,

$$\begin{aligned} \mathcal{E} &= Re\left\{\mathcal{E}_p e^{-i\omega_p t} + \mathcal{E}_{\mathcal{C}1} e^{-i\omega_{\mathcal{C}1} t} + \mathcal{E}_{\mathcal{C}2} e^{-i\omega_{\mathcal{C}2} t}\right\} \quad , \\ \mathcal{B} &= Re\left\{\mathcal{B}_p e^{-i\omega_p t} + \mathcal{B}_{2m} e^{-i\omega_{2m} t}\right\} \quad . \end{aligned} \qquad \text{[C.8]}$$

We use the rotating wave approximation to reduce H_{int} such that only the relevant field terms remain and introduce the Rabi frequencies,

$$\begin{aligned} \Omega_{ga} &= \frac{d_{ga}\mathcal{E}^*_{\mathcal{C}1}}{\hbar} \quad , \quad \Omega_{gb} = \frac{d_{gb}\mathcal{E}^*_{p}}{\hbar} \quad , \quad \Omega_{1a} = \frac{d_{1a}\mathcal{E}^*_{p}}{\hbar} \quad , \quad \Omega_{2b} = \frac{d_{2b}\mathcal{E}^*_{\mathcal{C}2}}{\hbar} \quad , \\ \Omega_{gm} &= \frac{\mu_{gm}\mathcal{B}^*_{p}}{\hbar} \quad , \quad \Omega_{1m} = \frac{\mu_{1m}\mathcal{B}^*_{2m}}{\hbar} \quad , \quad \Omega_{2m} = \frac{\mu_{2m}\mathcal{B}^*_{2m}}{\hbar} \quad , \end{aligned} \tag{C.9}$$

and express the interaction Hamiltonian matrix:

$$H_{int} = -\frac{\hbar}{2}\begin{bmatrix} 0 & 0 & 0 & \Omega_{gm}e^{i\omega_p t} & \Omega_{ga}e^{i\omega_{\mathcal{C}1} t} & \Omega_{gb}e^{i\omega_p t} \\ 0 & 0 & 0 & \Omega_{1m}e^{i\omega_{2m} t} & \Omega_{1a}e^{i\omega_p t} & 0 \\ 0 & 0 & 0 & \Omega_{2m}e^{i\omega_{2m} t} & 0 & \Omega_{2b}e^{i\omega_{\mathcal{C}2} t} \\ \Omega^*_{gm}e^{-i\omega_p t} & \Omega^*_{1m}e^{-i\omega_{2m} t} & \Omega^*_{2m}e^{-i\omega_{2m} t} & 0 & 0 & 0 \\ \Omega^*_{ga}e^{-i\omega_{\mathcal{C}1} t} & \Omega^*_{1a}e^{-i\omega_p t} & 0 & 0 & 0 & 0 \\ \Omega^*_{gb}e^{-i\omega_p t} & 0 & \Omega^*_{2b}e^{-i\omega_{\mathcal{C}2} t} & 0 & 0 & 0 \end{bmatrix} \tag{C.10}$$

We transform the Hamiltonian to a rotating reference frame by using a suitable unitary transformation matrix,

$$U = \begin{bmatrix} e^{i\omega_g t} & 0 & 0 & 0 & 0 & 0 \\ 0 & e^{i(\omega_{\mathcal{C}1}-\omega_p+\omega_g)t} & 0 & 0 & 0 & 0 \\ 0 & 0 & e^{i(\omega_p-\omega_{\mathcal{C}2}+\omega_g)t} & 0 & 0 & 0 \\ 0 & 0 & 0 & e^{i(\omega_p+\omega_g)t} & 0 & 0 \\ 0 & 0 & 0 & 0 & e^{i(\omega_{\mathcal{C}1}+\omega_g)t} & 0 \\ 0 & 0 & 0 & 0 & 0 & e^{i(\omega_p+\omega_g)t} \end{bmatrix} \quad . \tag{C.11}$$

With this transformation to a rotating frame, we suppresses oscillations in the time evolution of the system and improve stability of numerical integration. In this rotating frame, the state vector is given by,

$$|\tilde{\psi}\rangle = U|\psi\rangle = \begin{bmatrix} \tilde{c}_g & \tilde{c}_1 & \tilde{c}_2 & \tilde{c}_m & \tilde{c}_a & \tilde{c}_b \end{bmatrix}^T \quad , \tag{C.12}$$

and we have the transformed Hamiltonian given by,

$$\tilde{H} = U\left(H_0 + H_{int}\right)U^\dagger - i\hbar U\frac{\partial U^\dagger}{\partial t}$$

$$= -\frac{\hbar}{2}\begin{bmatrix} 0 & 0 & 0 & \Omega_{gm} & \Omega_{ga} & \Omega_{gb} \\ 0 & -2\delta\omega_1 & 0 & \Omega_{1m} & \Omega_{1a} & 0 \\ 0 & 0 & -2\delta\omega_2 & \Omega_{2m} & 0 & \Omega_{2b} \\ \Omega^*_{gm} & \Omega^*_{1m} & \Omega^*_{2m} & -2\delta\omega_{\mathcal{B}} & 0 & 0 \\ \Omega^*_{ga} & \Omega^*_{1a} & 0 & 0 & -2\delta\omega_a & 0 \\ \Omega^*_{gb} & 0 & \Omega^*_{2b} & 0 & 0 & -2\delta\omega_b \end{bmatrix} \quad , \qquad \text{[C.13]}$$

where the detunings are defined as:

$$\begin{aligned} \delta\omega_1 &\equiv (\omega_1 - \omega_g) - (\omega_{\mathcal{C}1} - \omega_p) \quad , \\ \delta\omega_2 &\equiv (\omega_2 - \omega_g) - (\omega_p - \omega_{\mathcal{C}2}) \quad , \\ \delta\omega_{\mathcal{B}} &\equiv (\omega_m - \omega_g) - \omega_p \quad , \\ \delta\omega_a &\equiv (\omega_a - \omega_g) - \omega_{\mathcal{C}1} \quad , \\ \delta\omega_b &\equiv (\omega_b - \omega_g) - \omega_p \quad . \end{aligned} \qquad \text{[C.14]}$$

We solve for the time evolution of the system by plugging the Hamiltonian from Eq. (C.13) into Eq. (C.3), resulting in the matrix $\dot{\tilde{\rho}}$, where each element is the rate equation of a coherence. For our 6 level system this results in a set of 36 coupled differential equations, which are:

$$\begin{aligned}
\dot{\tilde{\rho}}_{gg} &= -\gamma_g\tilde{\rho}_{gg} + \frac{\Gamma_a}{3}\tilde{\rho}_{aa} + \frac{\Gamma_b}{3}\tilde{\rho}_{bb} + \gamma_1\tilde{\rho}_{11} + \gamma_2\tilde{\rho}_{22} + \gamma_m\tilde{\rho}_{mm} \\
&+ \frac{i}{2}\left[\tilde{\rho}^*_{gm}\Omega_{gm} + \tilde{\rho}^*_{ga}\Omega_{ga} + \tilde{\rho}^*_{gb}\Omega_{gb} - h.c.\right] \quad , \\
\dot{\tilde{\rho}}_{g1} &= \frac{i2\delta\omega_1 - (\gamma_1 + \gamma_g)}{2}\tilde{\rho}_{g1} + \frac{i}{2}\left[-\tilde{\rho}_{gm}\Omega^*_{1m} - \tilde{\rho}_{ga}\Omega^*_{1a} + \tilde{\rho}^*_{1m}\Omega_{gm} + \tilde{\rho}^*_{1a}\Omega_{ga} + \tilde{\rho}^*_{1b}\Omega_{gb}\right] \quad , \\
\dot{\tilde{\rho}}_{g2} &= \frac{i2\delta\omega_2 - (\gamma_2 + \gamma_g)}{2}\tilde{\rho}_{g2} + \frac{i}{2}\left[-\tilde{\rho}_{gm}\Omega^*_{2m} - \tilde{\rho}_{gb}\Omega^*_{2b} + \tilde{\rho}^*_{2m}\Omega_{gm} + \tilde{\rho}^*_{2a}\Omega_{ga} + \tilde{\rho}^*_{2b}\Omega_{gb}\right] \quad , \\
\dot{\tilde{\rho}}_{gm} &= \frac{i2\delta\omega_{\mathcal{B}} - (\gamma_m + \gamma_g)}{2}\tilde{\rho}_{gm} \\
&+ \frac{i}{2}\left[-\tilde{\rho}_{g1}\Omega_{1m} - \tilde{\rho}_{g2}\Omega_{2m} + (\tilde{\rho}_{mm} - \tilde{\rho}_{gg})\,\Omega_{gm} + \tilde{\rho}^*_{ma}\Omega_{ga} + \tilde{\rho}^*_{mb}\Omega_{gb}\right] \quad , \\
\dot{\tilde{\rho}}_{ga} &= \frac{i2\delta\omega_a - (\Gamma_a + \gamma_g)}{2}\tilde{\rho}_{ga} + \frac{i}{2}\left[-\tilde{\rho}_{g1}\Omega_{1a} + \tilde{\rho}_{ma}\Omega_{gm} + (\tilde{\rho}_{aa} - \tilde{\rho}_{gg})\,\Omega_{ga} + \tilde{\rho}^*_{ab}\Omega_{gb}\right] \quad , \\
\dot{\tilde{\rho}}_{gb} &= \frac{i2\delta\omega_b - (\Gamma_b + \gamma_g)}{2}\tilde{\rho}_{gb} + \frac{i}{2}\left[-\tilde{\rho}_{g2}\Omega_{2b} + \tilde{\rho}_{mb}\Omega_{gm} + (\tilde{\rho}_{bb} - \tilde{\rho}_{gg})\,\Omega_{gb} + \tilde{\rho}_{ab}\Omega_{ga}\right] \quad ,
\end{aligned}$$

$$
\begin{aligned}
\dot{\tilde{\rho}}_{11} &= -\gamma_1\tilde{\rho}_{11} + \frac{\Gamma_a}{3}\tilde{\rho}_{aa} + \frac{\Gamma_b}{3}\tilde{\rho}_{bb} + \frac{i}{2}\left[\tilde{\rho}^*_{1m}\Omega_{1m} + \tilde{\rho}^*_{1a}\Omega_{1a} - h.c.\right] \quad , \\
\dot{\tilde{\rho}}_{12} &= \frac{i2\left(\delta\omega_2 - \delta\omega_1\right) - \left(\gamma_1 + \gamma_2\right)}{2}\tilde{\rho}_{12} - \frac{i}{2}\left[-\tilde{\rho}^*_{2m}\Omega_{1m} - \tilde{\rho}^*_{2a}\Omega_{1a} + \tilde{\rho}_{1m}\Omega^*_{2m} + \tilde{\rho}_{1b}\Omega^*_{2b}\right] \quad , \\
\dot{\tilde{\rho}}_{1m} &= \frac{i2\left(\delta\omega_{\mathcal{B}} - \delta\omega_1\right) - \left(\gamma_1 + \gamma_m\right)}{2}\tilde{\rho}_{1m} \\
&+ \frac{i}{2}\left[\left(\tilde{\rho}_{mm} - \tilde{\rho}_{11}\right)\Omega_{1m} + \tilde{\rho}^*_{ma}\Omega_{1a} - \tilde{\rho}_{12}\Omega_{2m} - \tilde{\rho}^*_{g1}\Omega_{gm}\right] \quad , \\
\dot{\tilde{\rho}}_{1a} &= \frac{i2\left(\delta\omega_a - \delta\omega_1\right) - \left(\gamma_1 + \Gamma_a\right)}{2}\tilde{\rho}_{1a} + \frac{i}{2}\left[\left(\tilde{\rho}_{aa} - \tilde{\rho}_{11}\right)\Omega_{1a} + \tilde{\rho}_{ma}\Omega_{1m} - \tilde{\rho}^*_{g1}\Omega_{ga}\right] \quad , \\
\dot{\tilde{\rho}}_{1b} &= \frac{i2\left(\delta\omega_b - \delta\omega_1\right) - \left(\gamma_1 + \Gamma_b\right)}{2}\tilde{\rho}_{1b} + \frac{i}{2}\left[\tilde{\rho}_{mb}\Omega_{1m} + \tilde{\rho}_{ab}\Omega_{1a} - \tilde{\rho}_{12}\Omega_{2b} - \tilde{\rho}^*_{g1}\Omega_{gb}\right] \quad , \\
\dot{\tilde{\rho}}_{22} &= -\gamma_2\tilde{\rho}_{22} + \frac{\Gamma_a}{3}\tilde{\rho}_{aa} + \frac{\Gamma_b}{3}\tilde{\rho}_{bb} + \frac{i}{2}\left[\tilde{\rho}^*_{2m}\Omega_{2m} + \tilde{\rho}^*_{2b}\Omega_{2b} - h.c.\right] \quad , \\
\dot{\tilde{\rho}}_{2m} &= \frac{i2\left(\delta\omega_{\mathcal{B}} - \delta\omega_2\right) - \left(\gamma_2 + \gamma_m\right)}{2}\tilde{\rho}_{2m} \\
&+ \frac{i}{2}\left[\left(\tilde{\rho}_{mm} - \tilde{\rho}_{22}\right)\Omega_{2m} - \tilde{\rho}^*_{12}\Omega_{1m} + \tilde{\rho}^*_{mb}\Omega_{2b} - \tilde{\rho}^*_{g2}\Omega_{gm}\right] \quad , \\
\dot{\tilde{\rho}}_{2a} &= \frac{i2\left(\delta\omega_a - \delta\omega_2\right) - \left(\gamma_2 + \Gamma_a\right)}{2}\tilde{\rho}_{2a} + \frac{i}{2}\left[-\tilde{\rho}^*_{12}\Omega_{1a} + \tilde{\rho}_{ma}\Omega_{2m} + \tilde{\rho}^*_{ab}\Omega_{2b} - \tilde{\rho}^*_{g2}\Omega_{ga}\right] \quad , \\
\dot{\tilde{\rho}}_{2b} &= \frac{i2\left(\delta\omega_b - \delta\omega_2\right) - \left(\gamma_2 + \Gamma_b\right)}{2}\tilde{\rho}_{2b} + \frac{i}{2}\left[\left(\tilde{\rho}_{bb} - \tilde{\rho}_{22}\right)\Omega_{2b} + \tilde{\rho}_{mb}\Omega_{2m} - \tilde{\rho}^*_{g2}\Omega_{gb}\right] \quad , \\
\dot{\tilde{\rho}}_{mm} &= -\gamma_m\tilde{\rho}_{mm} + \frac{i}{2}\left[\tilde{\rho}_{1m}\Omega^*_{1m} + \tilde{\rho}_{2m}\Omega^*_{2m} + \tilde{\rho}_{gm}\Omega^*_{gm} - h.c.\right] \quad , \\
\dot{\tilde{\rho}}_{ma} &= \frac{i2\left(\delta\omega_a - \delta\omega_{\mathcal{B}}\right) - \left(\gamma_m + \Gamma_a\right)}{2}\tilde{\rho}_{ma} \\
&- \frac{i}{2}\left[-\tilde{\rho}_{1a}\Omega^*_{1m} + \tilde{\rho}^*_{1m}\Omega_{1a} - \tilde{\rho}_{2a}\Omega^*_{2m} - \tilde{\rho}_{ga}\Omega^*_{gm} + \tilde{\rho}^*_{gm}\Omega_{ga}\right] \quad , \\
\dot{\tilde{\rho}}_{mb} &= \frac{i2\left(\delta\omega_b - \delta\omega_{\mathcal{B}}\right) - \left(\gamma_m + \Gamma_b\right)}{2}\tilde{\rho}_{mb} \\
&- \frac{i}{2}\left[-\tilde{\rho}_{1b}\Omega^*_{1m} + \tilde{\rho}^*_{2m}\Omega_{2b} - \tilde{\rho}_{2b}\Omega^*_{2m} - \tilde{\rho}_{gb}\Omega^*_{gm} + \tilde{\rho}^*_{gm}\Omega_{gb}\right] \quad , \\
\dot{\tilde{\rho}}_{aa} &= -\Gamma_a\tilde{\rho}_{aa} + \frac{i}{2}\left[\tilde{\rho}_{1a}\Omega^*_{1a} + \tilde{\rho}_{ga}\Omega^*_{ga} - h.c.\right] \quad , \\
\dot{\tilde{\rho}}_{ab} &= \frac{i2\left(\delta\omega_b - \delta\omega_a\right) - \left(\Gamma_a + \Gamma_b\right)}{2}\tilde{\rho}_{ab} - \frac{i}{2}\left[-\tilde{\rho}_{1b}\Omega^*_{1a} + \tilde{\rho}^*_{2a}\Omega_{2b} - \tilde{\rho}_{gb}\Omega^*_{ga} + \tilde{\rho}^*_{ga}\Omega_{gb}\right] \quad , \\
\dot{\tilde{\rho}}_{bb} &= -\Gamma_b\tilde{\rho}_{bb} + \frac{i}{2}\left[\tilde{\rho}_{2b}\Omega^*_{2b} + \tilde{\rho}_{gb}\Omega^*_{gb} - h.c.\right] \quad . \qquad \text{[C.15]}
\end{aligned}
$$

The remaining elements of the 6×6 density matrix can be found using $\tilde{\rho}_{ij} = \tilde{\rho}^*_{ji}$.

To ensure a closed system with population conservation, we have assumed equal branching ratios for decays from the excited electric states $|a\rangle$ and $|b\rangle$ to the states $|g\rangle$, $|1\rangle$, and $|2\rangle$ and

included the appropriate population transfer terms in Eqs. (C.15). This is verified by,

$$\frac{\partial}{\partial t}\left(\tilde{\rho}_{gg}+\tilde{\rho}_{11}+\tilde{\rho}_{22}+\tilde{\rho}_{mm}+\tilde{\rho}_{aa}+\tilde{\rho}_{bb}\right)=-\gamma_g\tilde{\rho}_{gg} \quad , \tag{C.16}$$

where decay of ground state is the only mechanism for population to leave the system, which we will assume to be zero.

For a given set of system parameters, we numerically integrate the coupled system of Eqs. (C.15) with the initial condition that the atoms start in the ground state, $\tilde{\rho}_{gg}=1$, and the lasers fields are off and gradually turned on to full power. We use fourth-order Runge-Kutta as our numerical integration algorithm and integrate in time until steady state values are reached for the coherences.

We proceed to solve for the various polarizabilities of the system by determining the polarization and magnetization, respectively, as

$$\begin{aligned} P(t) &= N\langle\psi|d|\psi\rangle = N\left\langle\tilde{\psi}|\tilde{d}|\tilde{\psi}\right\rangle \quad , \\ M(t) &= N\langle\psi|\mu|\psi\rangle = N\left\langle\tilde{\psi}|\tilde{\mu}|\tilde{\psi}\right\rangle \quad . \end{aligned} \tag{C.17}$$

In the rotating frame the dipole transition matrix are given as,

$$\tilde{d}=UdU^{\dagger}=\begin{bmatrix} 0 & 0 & 0 & 0 & d_{ga}e^{-i\omega_{\mathcal{C}1}t} & d_{gb}e^{-i\omega_p t} \\ 0 & 0 & 0 & 0 & d_{1a}e^{-i\omega_p t} & 0 \\ 0 & 0 & 0 & 0 & 0 & d_{2b}e^{-i\omega_{\mathcal{C}2}t} \\ 0 & 0 & 0 & 0 & 0 & 0 \\ d^*_{ga}e^{i\omega_{\mathcal{C}1}t} & d^*_{1a}e^{i\omega_p t} & 0 & 0 & 0 & 0 \\ d^*_{gb}e^{i\omega_p t} & 0 & d^*_{2b}e^{i\omega_{\mathcal{C}2}t} & 0 & 0 & 0 \end{bmatrix} \quad , \tag{C.18}$$

$$\tilde{\mu}=U\mu U^{\dagger}=\begin{bmatrix} 0 & 0 & 0 & \mu_{gm}e^{-i\omega_p t} & 0 & 0 \\ 0 & 0 & 0 & \mu_{1m}e^{-i(2\omega_p-\omega_{\mathcal{C}1})t} & 0 & 0 \\ 0 & 0 & 0 & \mu_{2m}e^{-i\omega_{\mathcal{C}2}t} & 0 & 0 \\ \mu^*_{gm}e^{i\omega_p t} & \mu^*_{1m}e^{i(2\omega_p-\omega_{\mathcal{C}1})t} & \mu^*_{2m}e^{i\omega_{\mathcal{C}2}t} & 0 & 0 & 0 \\ 0 & 0 & 0 & 0 & 0 & 0 \\ 0 & 0 & 0 & 0 & 0 & 0 \end{bmatrix} . \tag{C.19}$$

In general the polarization and magnetization are long expressions with many terms, however we are only interested in the probe beam frequency Fourier components, P_p and M_p. By noting that

$$\begin{aligned} 2P(t) &= \sum_n P_n e^{-i\omega_n t} + P_n^* e^{i\omega_n t} \quad , \\ 2M(t) &= \sum_n M_n e^{-i\omega_n t} + M_n^* e^{i\omega_n t} \quad , \end{aligned} \tag{C.20}$$

we can solve for P_p and M_p by extracting all the terms of $2P(t)$ and $2M(t)$, respectively, that include the oscillation $e^{-i\omega_p t}$.

We take the polarization and magnetization in the rotating frame by plugging Eqs. (C.18-C.19) into Eq. (C.17) to find the probe Fourier components in terms of the system coherences:

$$\begin{aligned} P_p &= 2N\left(\tilde{\rho}_{1a}^* d_{1a} + \tilde{\rho}_{gb}^* d_{gb}\right) \quad , \\ M_p &= 2N\left(\tilde{\rho}_{gm}^* \mu_{gm}\right) \quad . \end{aligned} \tag{C.21}$$

Using the definition of the polarization and the magnetization in a cross-coupled medium:

$$\begin{aligned} P_p &\equiv N\left(\alpha_{\mathcal{EE}}\mathcal{E}_p + \alpha_{\mathcal{EB}}\mathcal{B}_p\right) \quad , \\ M_p &\equiv N\left(\alpha_{\mathcal{BE}}\mathcal{E}_p + \alpha_{\mathcal{BB}}\mathcal{B}_p\right) \quad , \end{aligned} \tag{C.22}$$

we wish to solve for the polarizabilities, $\alpha_{\mathcal{EE}}$, $\alpha_{\mathcal{BB}}$, $\alpha_{\mathcal{EB}}$, and $\alpha_{\mathcal{BE}}$ in terms of the numerically computed steady state coherence values. By relating Eqs. (C.21) with Eqs. (C.22) we have the relations:

$$\begin{aligned} 2\left(\tilde{\rho}_{1a}^* d_{1a} + \tilde{\rho}_{gb}^* d_{gb}\right) &= \alpha_{\mathcal{EE}}\mathcal{E}_p + \alpha_{\mathcal{EB}}\mathcal{B}_p \quad , \\ 2\tilde{\rho}_{gm}^* \mu_{gm} &= \alpha_{\mathcal{BE}}\mathcal{E}_p + \alpha_{\mathcal{BB}}\mathcal{B}_p \quad . \end{aligned} \tag{C.23}$$

C.2 Isolating electric and magnetic dependencies of coherences

To numerically determine the polarizabilities we follow the method used by Fleischhauer et al. [62]. In general the coherences of the LHS of Eqs. (C.23) are functions of both the probe electric

and magnetic field amplitudes,

$$\begin{aligned} \tilde{\rho}^*_{1a} &= k\left(\mathcal{E}_p, \mathcal{B}_p\right) \quad , \\ \tilde{\rho}^*_{gb} &= l\left(\mathcal{E}_p, \mathcal{B}_p\right) \quad , \\ \tilde{\rho}^*_{gm} &= m\left(\mathcal{E}_p, \mathcal{B}_p\right) \quad , \end{aligned} \tag{C.24}$$

and the polarizability coefficients, α_{ij}, are functions of both field amplitudes as well. Examining the relations of Eqs. (C.23), it appears difficult to uniquely separate the electric and magnetic field dependencies of the numerical LHS, such that we may equate these to the corresponding polarizability factors of the RHS. A unique separation of the dependices of the numerical LHS can performed as follows by first expanding the functions k, l, and m in a power series of the field amplitudes:

$$\begin{aligned} k\left(\mathcal{E}_p, \mathcal{B}_p\right) &= \sum_{i,j} k_{ij} \mathcal{E}_p^i \mathcal{B}_p^j \quad , \\ l\left(\mathcal{E}_p, \mathcal{B}_p\right) &= \sum_{i,j} l_{ij} \mathcal{E}_p^i \mathcal{B}_p^j \quad , \\ m\left(\mathcal{E}_p, \mathcal{B}_p\right) &= \sum_{i,j} m_{ij} \mathcal{E}_p^i \mathcal{B}_p^j \quad . \end{aligned} \tag{C.25}$$

We note that because we are only considering the polarization and magnetization oscillating at the probe frequency, $e^{-i\omega_p t}$, there must physically be only terms in the power series that feature an odd number of field amplitudes, e.g. $i + j$ is an odd integer. This is because in the dynamics of the coherences, each appearance of a probe field term includes an oscillation factor of either $e^{-i\omega_p t}$ or $e^{i\omega_p t}$, which result in odd numbers of field terms oscillating at the probe frequency, ω_p, and even numbers of field terms being static. Since an odd number of field amplitudes can only result from an odd power of $\mathcal{E}_p$ with even power of $\mathcal{B}_p$ and vice versa, we can split the power expansions of Eqs. (C.25) as:

$$\begin{aligned} k\left(\mathcal{E}_p, \mathcal{B}_p\right) &= \sum_{i,j} k^{\mathcal{E}}_{ij} \left|\mathcal{E}_p\right|^{2i} \left|\mathcal{B}_p\right|^{2j} \mathcal{E}_p + \sum_{i,j} k^{\mathcal{B}}_{ij} \left|\mathcal{E}_p\right|^{2i} \left|\mathcal{B}_p\right|^{2j} \mathcal{B}_p \quad , \\ l\left(\mathcal{E}_p, \mathcal{B}_p\right) &= \sum_{i,j} l^{\mathcal{E}}_{ij} \left|\mathcal{E}_p\right|^{2i} \left|\mathcal{B}_p\right|^{2j} \mathcal{E}_p + \sum_{i,j} l^{\mathcal{B}}_{ij} \left|\mathcal{E}_p\right|^{2i} \left|\mathcal{B}_p\right|^{2j} \mathcal{B}_p \quad , \\ m\left(\mathcal{E}_p, \mathcal{B}_p\right) &= \sum_{i,j} m^{\mathcal{E}}_{ij} \left|\mathcal{E}_p\right|^{2i} \left|\mathcal{B}_p\right|^{2j} \mathcal{E}_p + \sum_{i,j} m^{\mathcal{B}}_{ij} \left|\mathcal{E}_p\right|^{2i} \left|\mathcal{B}_p\right|^{2j} \mathcal{B}_p \quad . \end{aligned} \tag{C.26}$$

After plugging the split behavior Eqs. (C.26) into relations of Eqs. (C.23), we can uniquely separate the electric and magnetic dependices to solve for the polarizability coefficients:

$$\begin{aligned}
\alpha_{\mathcal{E}\mathcal{E}} &= 2\left[d_{1a}\left(\sum_{i,j} k_{ij}^{\mathcal{E}} \left|\mathcal{E}_p\right|^{2i} \left|\mathcal{B}_p\right|^{2j}\right) + d_{gb}\left(\sum_{i,j} l_{ij}^{\mathcal{E}} \left|\mathcal{E}_p\right|^{2i} \left|\mathcal{B}_p\right|^{2j}\right)\right] \quad , \\
\alpha_{\mathcal{E}\mathcal{B}} &= 2\left[d_{1a}\left(\sum_{i,j} k_{ij}^{\mathcal{B}} \left|\mathcal{E}_p\right|^{2i} \left|\mathcal{B}_p\right|^{2j}\right) + d_{gb}\left(\sum_{i,j} l_{ij}^{\mathcal{B}} \left|\mathcal{E}_p\right|^{2i} \left|\mathcal{B}_p\right|^{2j}\right)\right] \quad , \\
\alpha_{\mathcal{B}\mathcal{E}} &= 2\left[\mu_{gm}\left(\sum_{i,j} m_{ij}^{\mathcal{E}} \left|\mathcal{E}_p\right|^{2i} \left|\mathcal{B}_p\right|^{2j}\right)\right] \quad , \\
\alpha_{\mathcal{B}\mathcal{B}} &= 2\left[\mu_{gm}\left(\sum_{i,j} m_{ij}^{\mathcal{B}} \left|\mathcal{E}_p\right|^{2i} \left|\mathcal{B}_p\right|^{2j}\right)\right] \quad . \qquad \text{[C.27]}
\end{aligned}$$

To solve for the split power series terms we make use of the symmetry properties of the odd functions in Eqs. (C.26), and note that by changing the sign of the field amplitudes we have:

$$\begin{aligned}
\sum_{i,j} k_{ij}^{\mathcal{E}} \left|\mathcal{E}_p\right|^{2i} \left|\mathcal{B}_p\right|^{2j} &= \frac{1}{2\mathcal{E}_p}\left[k\left(\mathcal{E}_p, \mathcal{B}_p\right) + k\left(\mathcal{E}_p, -\mathcal{B}_p\right)\right] \quad , \\
\sum_{i,j} k_{ij}^{\mathcal{B}} \left|\mathcal{E}_p\right|^{2i} \left|\mathcal{B}_p\right|^{2j} &= \frac{1}{2\mathcal{B}_p}\left[k\left(\mathcal{E}_p, \mathcal{B}_p\right) + k\left(-\mathcal{E}_p, \mathcal{B}_p\right)\right] \quad , \qquad \text{[C.28]}
\end{aligned}$$

and similarly for the expansions of l and m. To compute the functions k, l, and m with negative field amplitudes we are required to numerically solve the density matrix dynamics of Eqs. (C.15), but change the sign of the corresponding probe electric or magnetic field amplitude parameters in the computation. Thus we have to numerically solve the system evolution for three cases: $(\mathcal{E}_p, \mathcal{B}_p)$, $(-\mathcal{E}_p, \mathcal{B}_p)$, and $(\mathcal{E}_p, -\mathcal{B}_p)$, in order to separate the electric and magnetic dependices and hence numerically compute the polarizability coefficients:

$$\begin{aligned}
\alpha_{\mathcal{E}\mathcal{E}} &= \frac{d_{gb}\left[l\left(\mathcal{E}_p, \mathcal{B}_p\right) + l\left(\mathcal{E}_p, -\mathcal{B}_p\right)\right] + d_{1a}\left[k\left(\mathcal{E}_p, \mathcal{B}_p\right) + k\left(\mathcal{E}_p, -\mathcal{B}_p\right)\right]}{\mathcal{E}_p} \quad , \\
\alpha_{\mathcal{E}\mathcal{B}} &= \frac{d_{gb}\left[l\left(\mathcal{E}_p, \mathcal{B}_p\right) + l\left(-\mathcal{E}_p, \mathcal{B}_p\right)\right] + d_{1a}\left[k\left(\mathcal{E}_p, \mathcal{B}_p\right) + k\left(-\mathcal{E}_p, \mathcal{B}_p\right)\right]}{\mathcal{B}_p} \quad , \\
\alpha_{\mathcal{B}\mathcal{E}} &= \frac{\mu_{gm}\left[m\left(\mathcal{E}_p, \mathcal{B}_p\right) + m\left(\mathcal{E}_p, -\mathcal{B}_p\right)\right]}{\mathcal{E}_p} \quad , \\
\alpha_{\mathcal{B}\mathcal{B}} &= \frac{\mu_{gm}\left[m\left(\mathcal{E}_p, \mathcal{B}_p\right) + m\left(-\mathcal{E}_p, \mathcal{B}_p\right)\right]}{\mathcal{B}_p} \quad . \qquad \text{[C.29]}
\end{aligned}$$

Appendix D: Distributed Bragg reflector via refractive index enhancement

D.1 Periodically varying refractive index

In our suggestion for an all-optical mirror, we create a periodically varying refractive index for the probe beam in a could of atoms by exploiting the intensity dependence of non-linear susceptibility, $\chi^{(3)}|\mathcal{E}_{\mathcal{C}}|^2$. Two counter-propagating control beams on the z-axis form a standing wave spatial interference pattern:

$$\begin{aligned} \mathcal{E}_{\mathcal{C}}^{tot}(z,t) &= \mathcal{E}_{\mathcal{C}} e^{i(k_{\mathcal{C}} z - \omega_{\mathcal{C}} t)} + \mathcal{E}_{\mathcal{C}} e^{i(-k_{\mathcal{C}} z - \omega_{\mathcal{C}} t)} \\ &= \mathcal{E}_{\mathcal{C}} e^{-i\omega_{\mathcal{C}} t}\left(2\cos\left(k_{\mathcal{C}} z\right)\right) \quad . \end{aligned} \tag{D.1}$$

The time averaged intensity of the control beam fields is a periodic spatially varying function,

$$\begin{aligned} I_{\mathcal{C}}(z) &= \frac{1}{2\eta}\left\langle \left|\mathcal{E}_{\mathcal{C}}^{tot}\right|^2 \right\rangle = \frac{2\left|\mathcal{E}_{\mathcal{C}}\right|^2}{\eta}\cos^2\left(k_{\mathcal{C}} z\right) \\ &= \frac{\left|\mathcal{E}_{\mathcal{C}}\right|^2}{\eta} + \frac{\left|\mathcal{E}_{\mathcal{C}}\right|^2}{\eta}\cos\left(2k_{\mathcal{C}} z\right) \quad . \end{aligned} \tag{D.2}$$

Thus there is a periodic variation of the refractive index according to the

$$\begin{aligned} n(z) &= n_1 + n_2 I_{\mathcal{C}}(z) \\ &= n_1 + \frac{n_2 I_{\mathcal{C}}^{max}}{2} + \frac{n_2 I_{\mathcal{C}}^{max}}{2}\cos\left(\frac{2\pi}{\Lambda} z\right) \quad , \end{aligned} \tag{D.3}$$

where we have introduced the periodicity, $\Lambda = \frac{1}{2}\lambda_{\mathcal{C}}$ by plugging the wave number $k_{\mathcal{C}} = \frac{2\pi}{\lambda_{\mathcal{C}}}$ into Eq. (D.2) and $I_{\mathcal{C}}^{max} = \frac{2|\mathcal{E}_{\mathcal{C}}|^2}{\eta}$. We separate the static and varying parts of the refractive index as $n(z) = n_0 + \Delta n(z)$, where

$$\begin{aligned} n_0 &= n_1 + \frac{n_2 I_{\mathcal{C}}^{max}}{2} \quad , \\ \Delta n(z) &= \frac{n_2 I_{\mathcal{C}}^{max}}{2}\cos\left(\frac{2\pi}{\Lambda} z\right) \quad . \end{aligned} \tag{D.4}$$

The refractive index of the probe beam is related to the permittivity by

$$n = \sqrt{\epsilon + \Delta\epsilon(z)} = \sqrt{1 + \chi^{(1)} + \chi^{(3)}\left|\mathcal{E}_{\mathcal{C}}^{tot}(z)\right|^2} \quad . \tag{D.5}$$

By using Eqs. (D.4-D5) and assuming $\chi \ll 1$, we have

$$\begin{aligned} n_0 &\approx 1 + \frac{1}{2}\chi^{(1)} \quad , \\ \Delta n\left(z\right) &\approx \frac{1}{2}\chi^{(3)}\left|\mathcal{E}_{\mathcal{C}}^{tot}\left(z\right)\right|^2 \quad . \end{aligned} \tag{D.6}$$

By noting in Eqn. (D.5) that $\Delta\epsilon\left(z\right) = \chi^{(3)}\left|\mathcal{E}_{\mathcal{C}}^{tot}\left(z\right)\right|^2$ and the relations for $\Delta n\left(z\right)$ in Eqs. (D.4) and (D.6), we find that

$$\begin{aligned} \Delta\epsilon\left(z\right) &\approx 2\Delta n\left(z\right) \\ &\approx n_2 I_{\mathcal{C}}^{max}\cos\left(\frac{2\pi}{\Lambda}z\right) \quad , \end{aligned} \tag{D.7}$$

giving us the spatial variation of the permittivity in the medium.

D.2 Coupled mode theory

The translational symmetry periodicity of the permittivity, $\epsilon\left(z\right) = \epsilon\left(z+\Lambda\right)$, resulting from the periodic intensity pattern, allows us to use the coupled mode theory of Yariv and Yeh [164]. The permittivity can be written as a Fourier expansion,

$$\Delta\epsilon\left(z\right) = \sum_{m\neq 0}\epsilon_m \exp\left(-im\frac{2\pi}{\Lambda}z\right) \quad , \tag{D.8}$$

where ϵ_m is the coefficient of the m-th mode. For the system we are considering, the periodic perturbation of the permittivity given in Eqn. (D.7) can be expressed as

$$\begin{aligned} \Delta\epsilon\left(z\right) &\approx n_2 I_{\mathcal{C}}^{max}\cos\left(\frac{2\pi}{\Lambda}z\right) \\ &= \frac{n_2 I_{\mathcal{C}}^{max}}{2}\left[\exp\left(-i\frac{2\pi}{\Lambda}z\right) + \exp\left(i\frac{2\pi}{\Lambda}z\right)\right] \quad , \end{aligned} \tag{D.9}$$

where we find the coefficients $\epsilon_{-1} = \epsilon_1 = \frac{n_2 I_{\mathcal{C}}^{max}}{2}$ and take all other coefficients to be zero.

The interference of the multiple reflections and refractions of light due to the periodic variation of the permittivity cause the medium to behave as a distributed Bragg reflector. The power reflection coefficient of a distributed Bragg reflector is given by [164]:

$$R = \frac{\kappa^*\kappa\sinh^2\left(sL\right)}{s^2\cosh^2\left(sL\right) + \left(\frac{\Delta\beta}{2}\right)^2\sinh^2\left(sL\right)} \quad , \tag{D.10}$$

where L is the length of the medium. The parameters given by

$$\begin{aligned} \Delta\beta &= 2k_p \cos\theta - \frac{2\pi}{\Lambda} \quad , \\ \kappa &= \frac{\omega_p^2 \mu_0 \mu \epsilon_0}{2k_0 \cos\theta} \epsilon_m \quad , \\ k_0 &= \frac{n_0 \omega_p}{c} \quad , \\ s &= \sqrt{\kappa^* \kappa - \left(\frac{\Delta\beta}{2}\right)^2} \quad , \end{aligned} \qquad \text{[D.11]}$$

contain the angular dependence, θ, the periodicity, Λ, and the magnitude of the variation, ϵ_m.

LIST OF REFERENCES

[1] K. Aikawa, A. Frisch, M. Mark, S. Baier, A. Rietzler, R. Grimm, and F. Ferlaino. Bose-einstein condensation of erbium. *Phys. Rev. Lett.*, 108:210401, May 2012.

[2] A. André, M. Bajcsy, A. S. Zibrov, and M. D. Lukin. Nonlinear optics with stationary pulses of light. *Phys. Rev. Lett.*, 94:063902, Feb 2005.

[3] A. André and M. D. Lukin. Manipulating light pulses via dynamically controlled photonic band gap. *Phys. Rev. Lett.*, 89:143602, Sep 2002.

[4] P. Anisimov and O. Kocharovskaya. 38th winter colloquium on physics of quantum electronics, snowbird, utah. *Invited Talk*, Jan 2008.

[5] M. Bajcsy, S. Hofferberth, V. Balic, T. Peyronel, M. Hafezi, A. S. Zibrov, V. Vuletic, and M. D. Lukin. Efficient all-optical switching using slow light within a hollow fiber. *Phys. Rev. Lett.*, 102:203902, May 2009.

[6] M. Bajcsy, A. S. Zibrov, and M. D. Lukin. Stationary pulses of light in an atomic medium. *Nature (London)*, 426:638–641, Dec 2003.

[7] S. Bentley and R. Boyd. Nonlinear optical lithography with ultra-high sub-rayleigh resolution. *Opt. Express*, 12(23):5735–5740, Nov 2004.

[8] A. J. Berglund, J. L. Hanssen, and J. J. McClelland. Narrow-line magneto-optical cooling and trapping of strongly magnetic atoms. *Phys. Rev. Lett.*, 100:113002, Mar 2008.

[9] A. J. Berglund, S. A. Lee, and J. J. McClelland. Sub-doppler laser cooling and magnetic trapping of erbium. *Phys. Rev. A*, 76:053418, Nov 2007.

[10] E. Betzig. Proposed method for molecular optical imaging. *Opt. Lett.*, 20(3):237–239, Feb 1995.

[11] V. P. Bhola. Optical study of caf2 : Pr3+. *Journal of Luminescence*, 10(3):185 – 192, 1975.

[12] A. N. Boto, P. Kok, D. S. Abrams, S. L. Braunstein, C. P. Williams, and J. P. Dowling. Quantum interferometric optical lithography: Exploiting entanglement to beat the diffraction limit. *Phys. Rev. Lett.*, 85:2733–2736, Sep 2000.

[13] R. W. Boyd. *Nonlinear Optics*. Elsevier Academic Press, Burlington, MA, USA, 2008.

[14] D. A. Braje, V. Balić, G. Y. Yin, and S. E. Harris. Low-light-level nonlinear optics with slow light. *Phys. Rev. A*, 68:041801, Oct 2003.

[15] R. M. Camacho, P. B. Dixon, R. T. Glasser, A. N. Jordan, and J. C. Howell. Realization of an all-optical zero to π cross-phase modulation jump. *Phys. Rev. Lett.*, 102:013902, Jan 2009.

[16] W. T. Carnall, P. R. Fields, and K. Rajnak. Electronic energy levels of the trivalent lanthanide aquo ions. iii. tb[sup 3 +]. *The Journal of Chemical Physics*, 49(10):4447–4449, 1968.

[17] U. K. Chettiar, A. V. Kildishev, H. Yuan, W. Cai, S. Xiao, V. P. Drachev, and V. M. Shalaev. Dual-band negative index metamaterial: double negative at 813 nm and single negative at 772 nm. *Opt. Lett.*, 32(12):1671–1673, Jun 2007.

[18] W. J. Childs. Hyperfine structure of $^5i_{8,7}$ atomic states of $\mathrm{dy}^{161,163}$ and the ground-state nuclear moments. *Phys. Rev. A*, 2:1692–1701, Nov 1970.

[19] W. J. Childs, L. S. Goodman, and V. Pfeufer. Hyperfine structure of the $4f^{12}6s^23h$ and ^3f terms of $^{167}\mathrm{Er}$ i by atomic-beam, laser-rf double resonance. *Phys. Rev. A*, 28:3402–3408, Dec 1983.

[20] I. L. Chuang and Y. Yamamoto. Simple quantum computer. *Phys. Rev. A*, 52:3489–3496, Nov 1995.

[21] D. M. Cook. *Theory of the Electromagnetic Field*. Prentice Hall, Englewood Cliffs, New Jersey, 1975.

[22] R. D. Cowan. *The Theory of Atomic Structure and Spectra*. University of California Press, Berkeley, CA, 1981.

[23] E. Cubukcu, K. Aydin, E. Ozbay, S. Foteinopoulou, and C. M. Soukoulis. Electromagnetic waves: Negative refraction by photonic crystals. *Nature (London)*, 423:604–607, June 2003.

[24] E. Cubukcu, K. Aydin, E. Ozbay, S. Foteinopoulou, and C. M. Soukoulis. Subwavelength resolution in a two-dimensional photonic-crystal-based superlens. *Phys. Rev. Lett.*, 91:207401, Nov 2003.

[25] M. D'Angelo, M. V. Chekhova, and Y. Shih. Two-photon diffraction and quantum lithography. *Phys. Rev. Lett.*, 87:013602, Jun 2001.

[26] A. M. C. Dawes, L. Illing, S. M. Clark, and D. J. Gauthier. All-optical switching in rubidium vapor. *Science*, 308(5722):672–674, 2005.

[27] G. H. Dieke and H. M. Crosswhite. The spectra of the doubly and triply ionized rare earths. *Appl. Opt.*, 2(7):675–686, Jul 1963.

[28] G. Dolling, C. Enkrich, M. Wegener, C. M. Soukoulis, and S. Linden. Low-loss negative-index metamaterial at telecommunication wavelengths. *Opt. Lett.*, 31(12):1800–1802, Jun 2006.

[29] G. Dolling, M. Wegener, C. M. Soukoulis, and S. Linden. Negative-index metamaterial at 780 nm wavelength. *Opt. Lett.*, 32(1):53–55, Jan 2007.

[30] Y. O. Dudin and A. Kuzmich. Strongly interacting rydberg excitations of a cold atomic gas. *Science*, 336(6083):887–889, 2012.

[31] V. A. Dzuba, U. I. Safronova, and W. R. Johnson. Energy levels and lifetimes of nd iv, pm iv, sm iv, and eu iv. *Phys. Rev. A*, 68:032503, Sep 2003.

[32] V. A. Dzuba, O. P. Sushkov, W. R. Johnson, and U. I. Safronova. Energy levels and lifetimes of gd iv and enhancement of the electron electric dipole moment. *Phys. Rev. A*, 66:032105, Sep 2002.

[33] H. J. Eichler. Laser-induced grating phenomena. *Optica Acta: International Journal of Optics*, 24(6):631–642, 1977.

[34] L. R. Elias, Wm. S. Heaps, and W. M. Yen. Excitation of uv fluorescence in laf_3 doped with trivalent cerium and praseodymium. *Phys. Rev. B*, 8:4989–4995, Dec 1973.

[35] R. W. Equall, Y. Sun, R. L. Cone, and R. M. Macfarlane. Ultraslow optical dephasing in eu^{3+}:y_2sio_5. *Phys. Rev. Lett.*, 72:2179–2182, Apr 1994.

[36] N. Fang, H. Lee, C. Sun, and X. Zhang. Sub-diffraction-limited optical imaging with a silver superlens. *Science*, 308(5721):534–537, 2005.

[37] M. Fleischhauer, A. Imamoglu, and J. P. Marangos. Electromagnetically induced transparency: Optics in coherent media. *Rev. Mod. Phys.*, 77:633–673, Jul 2005.

[38] M. Fleischhauer, C. H. Keitel, M. O. Scully, Chang Su, B. T. Ulrich, and S. Zhu. Resonantly enhanced refractive index without absorption via atomic coherence. *Phys. Rev. A*, 46:1468–1487, Aug 1992.

[39] S. Foteinopoulou, E. N. Economou, and C. M. Soukoulis. Refraction in media with a negative refractive index. *Phys. Rev. Lett.*, 90:107402, Mar 2003.

[40] I. Friedler, G. Kurizki, and D. Petrosyan. Deterministic quantum logic with photons via optically induced photonic band gaps. *Phys. Rev. A*, 71:023803, Feb 2005.

[41] I. Friedler, D. Petrosyan, M. Fleischhauer, and G. Kurizki. Long-range interactions and entanglement of slow single-photon pulses. *Phys. Rev. A*, 72:043803, Oct 2005.

[42] T. Fukuhara, S. Sugawa, and Y. Takahashi. Bose-einstein condensation of an ytterbium isotope. *Phys. Rev. A*, 76:051604, Nov 2007.

[43] J. Gea-Banacloche. Impossibility of large phase shifts via the giant kerr effect with single-photon wave packets. *Phys. Rev. A*, 81:043823, Apr 2010.

[44] D. A. Gurnett and Bhattacharjee A. *Introduction to Plasma Physics*. Cambridge University Press, Cambridge, UK, 2005.

[45] B. S. Ham, P. R. Hemmer, and M. S. Shahriar. Efficient electromagnetically induced transparency in a rare-earth doped crystal. *Optics Communications*, 144(46):227 – 230, 1997.

[46] B. S. Ham, P. R. Hemmer, and M. S. Shahriar. Efficient phase conjugation via two-photon coherence in an optically dense crystal. *Phys. Rev. A*, 59:R2583–R2586, Apr 1999.

[47] C. I. Hancox, S. C. Doret, M. T. Hummon, L. Luo, and J. M. Doyle. Magnetic trapping of rare-earth atoms at millikelvin temperatures. *Nature (London)*, 431:281, Sept 2004.

[48] S. E. Harris. Refractive-index control with strong fields. *Opt. Lett.*, 19(23):2018–2020, Dec 1994.

[49] S. E. Harris. Electromagnetically induced transparency. *Physics Today*, 50(7):36–42, 1997.

[50] S. E. Harris and L. V. Hau. Nonlinear optics at low light levels. *Phys. Rev. Lett.*, 82:4611–4614, Jun 1999.

[51] S. E. Harris and A. V. Sokolov. Broadband spectral generation with refractive index control. *Phys. Rev. A*, 55:R4019–R4022, Jun 1997.

[52] S. E. Harris and Y. Yamamoto. Photon switching by quantum interference. *Phys. Rev. Lett.*, 81:3611–3614, Oct 1998.

[53] E. Hecht. *Optics*. Addison Wesley, San Francisco, CA, 2002.

[54] S. W. Hell and J. Wichmann. Breaking the diffraction resolution limit by stimulated emission: stimulated-emission-depletion fluorescence microscopy. *Opt. Lett.*, 19(11):780–782, Jun 1994.

[55] C. Hettich, C. Schmitt, J. Zitzmann, S. Khn, I. Gerhardt, and V. Sandoghdar. Nanometer resolution and coherent optical dipole coupling of two individual molecules. *Science*, 298(5592):385–389, 2002.

[56] A. A. Houck, J. B. Brock, and I. L. Chuang. Experimental observations of a left-handed material that obeys snell's law. *Phys. Rev. Lett.*, 90:137401, Apr 2003.

[57] C. Jeppesen, R. B. Nielsen, A. Boltasseva, S. Xiao, N. A. Mortensen, and A. Kristensen. Thin film ag superlens towards lab-on-a-chip integration. *Opt. Express*, 17(25):22543–22552, Dec 2009.

[58] W. G. Jin, T. Horiguchi, M. Wakasugi, and Y. Yoshizawa. Hyperfine structure and isotope shift in er i by the atomic-beam laser spectroscopy. *Journal of the Physical Society of Japan*, 59(9):3148–3154, 1990.

[59] K. S. Johnson, J. H. Thywissen, N. H. Dekker, K. K. Berggren, A. P. Chu, R. Younkin, and M. Prentiss. Localization of metastable atom beams with optical standing waves: Nanolithography at the heisenberg limit. *Science*, 280(5369):1583–1586, 1998.

[60] H. Kang and Y. Zhu. Observation of large kerr nonlinearity at low light intensities. *Phys. Rev. Lett.*, 91:093601, Aug 2003.

[61] J. Kästel, M. Fleischhauer, and G. Juzeliūnas. Local-field effects in magnetodielectric media: Negative refraction and absorption reduction. *Phys. Rev. A*, 76:062509, Dec 2007.

[62] J. Kästel, M. Fleischhauer, S. F. Yelin, and R. L. Walsworth. Tunable negative refraction without absorption via electromagnetically induced chirality. *Phys. Rev. Lett.*, 99:073602, Aug 2007.

[63] J. Kästel, M. Fleischhauer, S. F. Yelin, and R. L. Walsworth. Low-loss negative refraction by laser-induced magnetoelectric cross coupling. *Phys. Rev. A*, 79:063818, Jun 2009.

[64] T. A. Klar, E. Engel, and S. W. Hell. Breaking abbe's diffraction resolution limit in fluorescence microscopy with stimulated emission depletion beams of various shapes. *Phys. Rev. E*, 64:066613, Nov 2001.

[65] J. Klein, F. Beil, and T. Halfmann. Rapid adiabatic passage in a pr 3+ :y 2 sio 5 crystal. *Journal of Physics B: Atomic, Molecular and Optical Physics*, 40(11):S345, 2007.

[66] J. Klein, F. Beil, and T. Halfmann. Robust population transfer by stimulated raman adiabatic passage in a pr^{+3}:$\mathrm{y_2sio_5}$ crystal. *Phys. Rev. Lett.*, 99:113003, Sep 2007.

[67] J. Klein, F. Beil, and T. Halfmann. Experimental investigations of stimulated raman adiabatic passage in a doped solid. *Phys. Rev. A*, 78:033416, Sep 2008.

[68] O. Kocharovskaya and P. Mandel. Amplification without inversion: The double-λ scheme. *Phys. Rev. A*, 42:523–535, Jul 1990.

[69] W. E. Kock. Metallic delay lenses. *Bell Syst. Tech. J.*, 27:58–82, Jan 1948.

[70] F. Könz, Y. Sun, C. W. Thiel, R. L. Cone, R. W. Equall, R. L. Hutcheson, and R. M. Macfarlane. Temperature and concentration dependence of optical dephasing, spectral-hole lifetime, and anisotropic absorption in eu^{3+}: $\mathrm{Y_2sio_5}$. *Phys. Rev. B*, 68:085109, Aug 2003.

[71] B. Lauritzen, S. R. Hastings-Simon, H. de Riedmatten, M. Afzelius, and N. Gisin. State preparation by optical pumping in erbium-doped solids using stimulated emission and spin mixing. *Phys. Rev. A*, 78:043402, Oct 2008.

[72] B. Lauritzen, N. Timoney, N. Gisin, M. Afzelius, H. de Riedmatten, Y. Sun, R. M. Macfarlane, and R. L. Cone. Spectroscopic investigations of eu^{3+}:y_2sio_5 for quantum memory applications. *Phys. Rev. B*, 85:115111, Mar 2012.

[73] U. Leonhardt. Optical conformal mapping. *Science*, 312(5781):1777–1780, 2006.

[74] U. Leonhardt and T. G. Philbin. General relativity in electrical engineering. *New Journal of Physics*, 8(10):247, 2006.

[75] H. J. Lezec, J. A. Dionne, and H. A. Atwater. Negative refraction at visible frequencies. *Science*, 316(5823):430–432, 2007.

[76] G. K. Liu, J. Huang, R. L. Cone, and B. Jacquier. Spectral hole burning, zeeman effect, and hyperfine structure for tb^{3+}:liyf_4. *Phys. Rev. B*, 38:11061–11067, Dec 1988.

[77] Z. Liu, N. Fang, T. Yen, and X. Zhang. Rapid growth of evanescent wave by a silver superlens. *Applied Physics Letters*, 83(25):5184–5186, 2003.

[78] E. Loh. $^1s_0$ level of pr^{3+} in crystals of fluorides. *Phys. Rev.*, 140:A1463–A1466, Nov 1965.

[79] A. Lorenzo, L. E. Bausá, and J. García Solé. Optical spectroscopy of pr^{3+} ions in linbo_3. *Phys. Rev. B*, 51:16643–16650, Jun 1995.

[80] M. Lu, N. Q. Burdick, and B. L. Lev. Quantum degenerate dipolar fermi gas. *Phys. Rev. Lett.*, 108:215301, May 2012.

[81] M. Lu, S. H. Youn, and B. L. Lev. Trapping ultracold dysprosium: A highly magnetic gas for dipolar physics. *Phys. Rev. Lett.*, 104:063001, Feb 2010.

[82] M. D. Lukin and A. Imamoğlu. Nonlinear optics and quantum entanglement of ultraslow single photons. *Phys. Rev. Lett.*, 84:1419–1422, Feb 2000.

[83] R. M. Macfarlane. High-resolution laser spectroscopy of rare-earth doped insulators: a personal perspective. *Journal of Luminescence*, 100(1-4):1 – 20, 2002.

[84] R. M. MacFarlane and R. M. Shelby. Homogeneous line broadening of optical transitions of ions and molecules in glasses. *Journal of Luminescence*, 36(45):179 – 207, 1987.

[85] M. Mašalas and M. Fleischhauer. Scattering of dark-state polaritons in optical lattices and quantum phase gate for photons. *Phys. Rev. A*, 69:061801, Jun 2004.

[86] A. B. Matsko, I. Novikova, G. R. Welch, and M. S. Zubairy. Enhancement of kerr nonlinearity by multiphoton coherence. *Opt. Lett.*, 28(2):96–98, Jan 2003.

[87] D. L. McAuslan, J. G. Bartholomew, M. J. Sellars, and J. J. Longdell. Reducing decoherence in optical and spin transitions in rare-earth-metal-ion˘doped materials. *Phys. Rev. A*, 85:032339, Mar 2012.

[88] J. J. McClelland and J. L. Hanssen. Laser cooling without repumping: A magneto-optical trap for erbium atoms. *Phys. Rev. Lett.*, 96:143005, Apr 2006.

[89] D. P. McLeod and M. F. Reid. Intensities of hyperfine transitions of pr3+ and ho3+ in caf2. *Journal of Alloys and Compounds*, 250(12):302 – 305, 1997.

[90] D. Melville and R. Blaikie. Super-resolution imaging through a planar silver layer. *Opt. Express*, 13(6):2127–2134, Mar 2005.

[91] R. Merlin. Analytical solution of the almost-perfect-lens problem. *Applied Physics Letters*, 84(8):1290–1292, 2004.

[92] C. Monzon and D. W. Forester. Negative refraction and focusing of circularly polarized waves in optically active media. *Phys. Rev. Lett.*, 95:123904, Sep 2005.

[93] R. Newell, J. Sebby, and T. G. Walker. Dense atom clouds in a holographic atom trap. *Opt. Lett.*, 28(14):1266–1268, Jul 2003.

[94] M. A. Nielsen and I. L. Chuang. *Quantum Computation and Quantum Information*. Cambridge University Press, Cambridge, UK, 2000.

[95] C. O'Brien and O. Kocharovskaya. Resonant enhancement of refractive index in transition element doped crystals via coherent control of excited state absorption. *Journal of Modern Optics*, 56(18-19):1933–1940, 2009.

[96] G. S. Ofelt. Intensities of crystal spectra of rare-earth ions. *The Journal of Chemical Physics*, 37(3):511–520, 1962.

[97] G. S. Ofelt. Structure of the f[sup 6] configuration with application to rare-earth ions. *The Journal of Chemical Physics*, 38(9):2171–2180, 1963.

[98] M. Ö. Oktel and Ö. E. Müstecaplıoğlu. Electromagnetically induced left-handedness in a dense gas of three-level atoms. *Phys. Rev. A*, 70:053806, Nov 2004.

[99] C. Ottaviani, S. Rebić, D. Vitali, and P. Tombesi. Quantum phase-gate operation based on nonlinear optics: Full quantum analysis. *Phys. Rev. A*, 73:010301, Jan 2006.

[100] C. Ottaviani, D. Vitali, M. Artoni, F. Cataliotti, and P. Tombesi. Polarization qubit phase gate in driven atomic media. *Phys. Rev. Lett.*, 90:197902, May 2003.

[101] P. V. Parimi, W. T. Lu, P. Vodo, J. Sokoloff, J. S. Derov, and S. Sridhar. Negative refraction and left-handed electromagnetism in microwave photonic crystals. *Phys. Rev. Lett.*, 92:127401, Mar 2004.

[102] P. S. Peijzel, A. Meijerink, R. T. Wegh, M. F. Reid, and G. W. Burdick. A complete energy level diagram for all trivalent lanthanide ions. *Journal of Solid State Chemistry*, 178(2):448 – 453, 2005.

[103] N. Pelletier-Allard and R. Pelletier. Magnetic-dipole and electric-quadrupole effects in $\mathrm{lacl_3{:}tb^{3+}}$. *Phys. Rev. B*, 31:2661–2666, Mar 1985.

[104] J. B. Pendry. Negative refraction makes a perfect lens. *Phys. Rev. Lett.*, 85:3966–3969, Oct 2000.

[105] J. B. Pendry. A chiral route to negative refraction. *Science*, 306(5700):1353–1355, 2004.

[106] J. B. Pendry, A. J. Holden, W. J. Stewart, and I. Youngs. Extremely low frequency plasmons in metallic mesostructures. *Phys. Rev. Lett.*, 76:4773–4776, Jun 1996.

[107] J. B. Pendry, D. Schurig, and D. R. Smith. Controlling electromagnetic fields. *Science*, 312(5781):1780–1782, 2006.

[108] J. B. Pendry and D. R. Smith. Reversing light with negative refraction. *Physics Today*, 57(6):37–43, 2004.

[109] J.B. Pendry, A.J. Holden, D.J. Robbins, and W.J. Stewart. Magnetism from conductors and enhanced nonlinear phenomena. *IEEE Trans. Microwave Theory Tech.*, 47:2075–2084, Nov 1999.

[110] D. Petrosyan and G. Kurizki. Symmetric photon-photon coupling by atoms with zeeman-split sublevels. *Phys. Rev. A*, 65:033833, Mar 2002.

[111] D. Petrosyan and Y. P. Malakyan. Magneto-optical rotation and cross-phase modulation via coherently driven four-level atomsin a tripod configuration. *Phys. Rev. A*, 70:023822, Aug 2004.

[112] T. Peyronel, Y. V. Rostovtsev, O. Firstenberg, Q. Liang, S. Hofferberth, A. V. Gorshkov, T. Pohl, M. D. Lukin, and V. Vuletic. Quantum nonlinear optics with single photons enabled by strongly interacting atoms. *Nature*, 488:57, Aug 2012.

[113] N. A. Proite, B. E. Unks, J. T. Green, and D. D. Yavuz. Refractive index enhancement with vanishing absorption in an atomic vapor. *Phys. Rev. Lett.*, 101:147401, Sep 2008.

[114] R. M. Rajapakse, T. Bragdon, A. M. Rey, T. Calarco, and S. F. Yelin. Single-photon nonlinearities using arrays of cold polar molecules. *Phys. Rev. A*, 80:013810, Jul 2009.

[115] U. Rathe, M. Fleischhauer, Shi-Yao Zhu, T. W. Hänsch, and M. O. Scully. Nonlinear theory of index enhancement via quantum coherence and interference. *Phys. Rev. A*, 47:4994–5002, Jun 1993.

[116] S. Rebić, C. Ottaviani, G. Di Giuseppe, D. Vitali, and P. Tombesi. Assessment of a quantum phase-gate operation based on nonlinear optics. *Phys. Rev. A*, 74:032301, Sep 2006.

[117] S. Rebić, D. Vitali, C. Ottaviani, P. Tombesi, M. Artoni, F. Cataliotti, and R. Corbalán. Polarization phase gate with a tripod atomic system. *Phys. Rev. A*, 70:032317, Sep 2004.

[118] M. S. Rill, C. Plet, M. Thiel, I. Staude, G. von Freymann, S. Linden, and M. Wegener. Photonic metamaterials by direct laser writing and silver chemical vapour deposition. *Nature Materials*, 7:543–546, July 2008.

[119] W. Rotman. Plasma simulation by artificial dielectrics and parallel-plate media. *IRE Trans. Antennas Propag.*, 10:82–95, Jan 1962.

[120] V. A. Sautenkov, Y. V. Rostovtsev, H. Chen, P. Hsu, G. S. Agarwal, and M. O. Scully. Electromagnetically induced magnetochiral anisotropy in a resonant medium. *Phys. Rev. Lett.*, 94:233601, Jun 2005.

[121] H. Schmidt and A. Imamoglu. Giant kerr nonlinearities obtained by electromagnetically induced transparency. *Opt. Lett.*, 21(23):1936–1938, Dec 1996.

[122] D. Schurig, J. J. Mock, B. J. Justice, S. A. Cummer, J. B. Pendry, A. F. Starr, and D. R. Smith. Metamaterial electromagnetic cloak at microwave frequencies. *Science*, 314(5801):977–980, 2006.

[123] D. Schurig, J. B. Pendry, and D. R. Smith. Calculation of material properties and ray tracing in transformation media. *Opt. Express*, 14(21):9794–9804, Oct 2006.

[124] M. O. Scully. Enhancement of the index of refraction via quantum coherence. *Phys. Rev. Lett.*, 67:1855–1858, Sep 1991.

[125] M. O. Scully and M. Fleischhauer. High-sensitivity magnetometer based on index-enhanced media. *Phys. Rev. Lett.*, 69:1360–1363, Aug 1992.

[126] M. O. Scully, S. Zhu, and A. Gavrielides. Degenerate quantum-beat laser: Lasing without inversion and inversion without lasing. *Phys. Rev. Lett.*, 62:2813–2816, Jun 1989.

[127] M. O. Scully and M. S. Zubairy. *Quantum Optics*. Cambridge University Press, Cambridge, UK, 1997.

[128] V. M. Shalaev, W. Cai, U. K. Chettiar, H. Yuan, A. K. Sarychev, V. P. Drachev, and A. V. Kildishev. Negative index of refraction in optical metamaterials. *Opt. Lett.*, 30(24):3356–3358, Dec 2005.

[129] J. H. Shapiro. Single-photon kerr nonlinearities do not help quantum computation. *Phys. Rev. A*, 73:062305, Jun 2006.

[130] J. H. Shapiro and M. Razavi. Continuous-time cross-phase modulation and quantum computation. *New Journal of Physics*, 9(1):16, 2007.

[131] R. A. Shelby, D. R. Smith, and S. Schultz. Experimental verification of a negative index of refraction. *Science*, 292(5514):77–79, 2001.

[132] J. Shen, Z. Ruan, and S. He. How to realize a negative refractive index material at the atomic level in an optical frequency range? *Journal of Zhejiang University SCIENCE A*, 5(11):1322–1326, 2004.

[133] A. E. Siegman. *Lasers*. University Science Books, Sausalito, CA, USA, 1986.

[134] D. E. Sikes and D. D. Yavuz. Negative refraction with low absorption using raman transitions with magnetoelectric coupling. *Phys. Rev. A*, 82:011806(R), Jul 2010.

[135] Z. J. Simmons, N. A. Proite, J. Miles, D. E. Sikes, and D. D. Yavuz. Refractive index enhancement with vanishing absorption in short, high-density vapor cells. *Phys. Rev. A*, 85:053810, May 2012.

[136] A. R. Slepkov, A. D. andBhagwat, V. Venkataraman, P. Londero, and A. L. Gaeta. Generation of large alkali vapor densities inside bare hollow-core photonic band-gap fibers. *Opt. Express*, 16(23):18976–18983, Nov 2008.

[137] D. R. Smith and N. Kroll. Negative refractive index in left-handed materials. *Phys. Rev. Lett.*, 85:2933–2936, Oct 2000.

[138] D. R. Smith, W. J. Padilla, D. C. Vier, S. C. Nemat-Nasser, and S. Schultz. Composite medium with simultaneously negative permeability and permittivity. *Phys. Rev. Lett.*, 84:4184–4187, May 2000.

[139] D. R. Smith, D. Schurig, M. Rosenbluth, S. Schultz, S. A. Ramakrishna, and J. B. Pendry. Limitations on subdiffraction imaging with a negative refractive index slab. *Applied Physics Letters*, 82(10):1506–1508, 2003.

[140] L. Solymar and E. Shamonina. *Waves in Metamaterials*. Oxford University Press Inc., New York, NY, USA, 2009.

[141] D. A. Steck. Alkali d line data. Technical report, Los Alamos National Laboratory, 2001.

[142] Y. Takasu, K. Honda, K. Komori, T. Kuwamoto, M. Kumakura, Y. Takahashi, and T. Yabuzaki. High-density trapping of cold ytterbium atoms by an optical dipole force. *Phys. Rev. Lett.*, 90:023003, Jan 2003.

[143] K. N. R. Taylor and M. I. Darby. *Physics of Rare Earth Solids*. Chapman and Hall, 1972.

[144] K. S. Thomas, S. Singh, and G. H. Dieke. Energy levels of tb[sup 3 +] in lacl[sub 3] and other chlorides. *The Journal of Chemical Physics*, 38(9):2180–2190, 1963.

[145] Q. Thommen and P. Mandel. Electromagnetically induced left handedness in optically excited four-level atomic media. *Phys. Rev. Lett.*, 96:053601, Feb 2006.

[146] Q. A. Turchette, C. J. Hood, W. Lange, H. Mabuchi, and H. J. Kimble. Measurement of conditional phase shifts for quantum logic. *Phys. Rev. Lett.*, 75:4710–4713, Dec 1995.

[147] A. V. Turukhin, V. S. Sudarshanam, M. S. Shahriar, J. A. Musser, B. S. Ham, and P. R. Hemmer. Observation of ultraslow and stored light pulses in a solid. *Phys. Rev. Lett.*, 88:023602, Dec 2001.

[148] J. Valentine, J. Li, T. Zentgraf, G. Bartal, and X. Zhang. An optical cloak made of dielectrics. *Nature Materials*, 8:568–571, July 2009.

[149] L. van Pieterson, M. F. Reid, G. W. Burdick, and A. Meijerink. $4f^n \rightarrow 4f^{n-1}5d$ transitions of the heavy lanthanides: experiment and theory. *Phys. Rev. B*, 65:045114, Jan 2002.

[150] L. van Pieterson, M. F. Reid, and A. Meijerink. Reappearance of fine structure as a probe of lifetime broadening mechanisms in the $4f \rightarrow 4f5d$ excitation spectra of tb^{+3}, er^{+3}, and tm^{+3} in caf_2 and $liyf_4$. *Phys. Rev. Lett.*, 88:067405, Jan 2002.

[151] L. van Pieterson, M. F. Reid, R. T. Wegh, S. Soverna, and A. Meijerink. $4f^n \rightarrow 4f^{n-1}5d$ transitions of the light lanthanides: experiment and theory. *Phys. Rev. B*, 65:045113, Jan 2002.

[152] V. G. Veselago. The electrodynamics of substances with simultaneously negative values of ϵ and μ. *Soviet Physics Uspekhi*, 10(4):509, 1968.

[153] H. Wang, D. Goorskey, and M. Xiao. Enhanced kerr nonlinearity via atomic coherence in a three-level atomic system. *Phys. Rev. Lett.*, 87:073601, Jul 2001.

[154] Z. Wang, K. Marzlin, and B. C. Sanders. Large cross-phase modulation between slow copropagating weak pulses in $^{87}\mathrm{Rb}$. *Phys. Rev. Lett.*, 97:063901, Aug 2006.

[155] A. J. Ward and J. B. Pendry. Refraction and geometry in maxwell's equations. *Journal of Modern Optics*, 43(4):773–793, 1996.

[156] M. J. Weber. Probabilities for radiative and nonradiative decay of er^{3+} in laf_3. *Phys. Rev.*, 157:262–272, May 1967.

[157] M. J. Weber. Selective excitation and decay of er^{3+} fluorescence in laf_3. *Phys. Rev.*, 156:231–241, Apr 1967.

[158] R. T. Wegh and A. Meijerink. Spin-allowed and spin-forbidden $4f^n \leftrightarrow 4f^{n-1}5d$ transitions for heavy lanthanides in fluoride hosts. *Phys. Rev. B*, 60:10820–10830, Oct 1999.

[159] B. G. Wybourne. *Spectroscopic Properties of Rare-Earths*. John Wiley & Sons, 1965.

[160] S. Xiao, U. K. Chettiar, A. V. Kildishev, V. P. Drachev, and V. M. Shalaev. Yellow-light negative-index metamaterials. *Opt. Lett.*, 34(22):3478–3480, Nov 2009.

[161] A. Yamaguchi, S. Uetake, D. Hashimoto, J. M. Doyle, and Y. Takahashi. Inelastic collisions in optically trapped ultracold metastable ytterbium. *Phys. Rev. Lett.*, 101:233002, Dec 2008.

[162] Y. Yamamoto and A. Imamoglu. *Mesoscopic Quantum Optics*. John Wiley & Sons, Inc., New York, NY, USA, 1999.

[163] M. Yan, E. G. Rickey, and Y. Zhu. Observation of absorptive photon switching by quantum interference. *Phys. Rev. A*, 64:041801, Sep 2001.

[164] A. Yariv and P. Yeh. *Optical Waves in Crystals*. Wiley, New York, 1984.

[165] D. D. Yavuz. Refractive index enhancement in a far-off resonant atomic system. *Phys. Rev. Lett.*, 95:223601, Nov 2005.

[166] D. D. Yavuz and N. A. Proite. Noise in refractive index enhancement. *Phys. Rev. A*, 78:053811, Nov 2008.

[167] D. D. Yavuz, A. V. Sokolov, and S. E. Harris. Eigenvectors of a raman medium. *Phys. Rev. Lett.*, 84:75–78, Jan 2000.

[168] T. J. Yen, W. J. Padilla, N. Fang, D. C. Vier, D. R. Smith, J. B. Pendry, D. N. Basov, and X. Zhang. Terahertz magnetic response from artificial materials. *Science*, 303(5663):1494–1496, 2004.

[169] J. Zhang, G. Hernandez, and Y. Zhu. All-optical switching at ultralow light levels. *Opt. Lett.*, 32(10):1317–1319, May 2007.

[170] S. Zhang, W. Fan, N. C. Panoiu, K. J. Malloy, R. M. Osgood, and S. R. J. Brueck. Experimental demonstration of near-infrared negative-index metamaterials. *Phys. Rev. Lett.*, 95:137404, Sep 2005.

[171] A. S. Zibrov, M. D. Lukin, L. Hollberg, D. E. Nikonov, M. O. Scully, H. G. Robinson, and V. L. Velichansky. Experimental demonstration of enhanced index of refraction via quantum coherence in rb. *Phys. Rev. Lett.*, 76:3935–3938, May 1996.